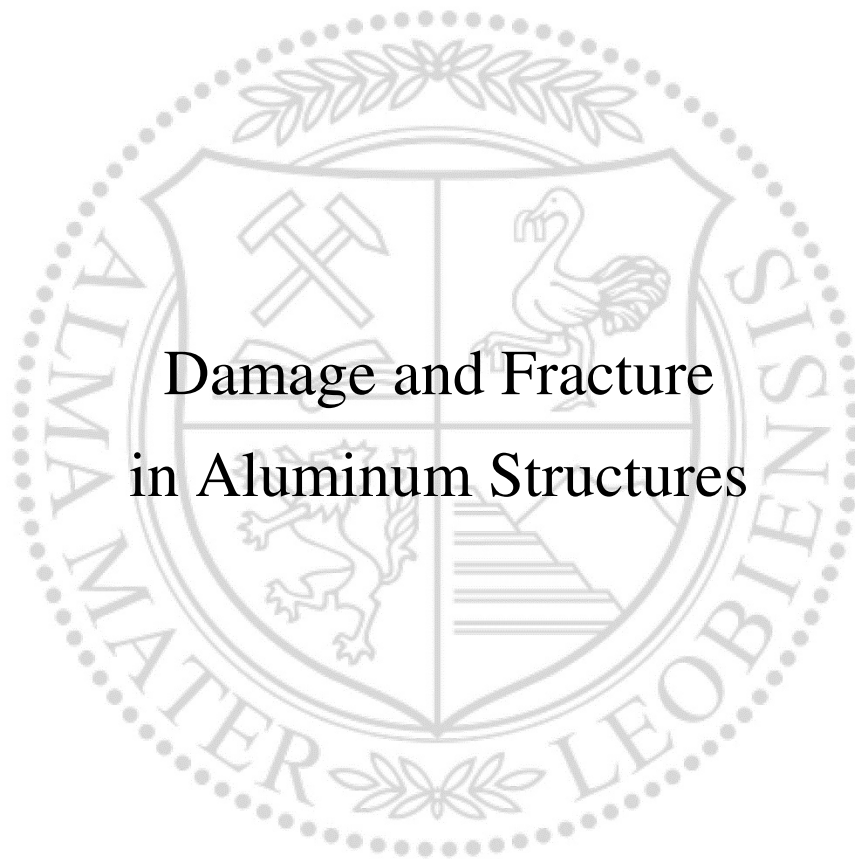




Institute of Mechanics

Doctoral Thesis



Damage and Fracture
in Aluminum Structures

Dipl.-Ing. Sandra Baltic, BSc

December 2020

Damage and Fracture

in Aluminum Structures

Sandra Baltic

Dissertation

eingereicht am

Institut für Mechanik

zur Erlangung des akademischen Grades

Doktor der montanistischen Wissenschaften

an der Montanuniversität Leoben

Dezember 2020

Affidavit

I declare on oath that I wrote this thesis independently, did not use other than the specified sources and aids, and did not otherwise use any unauthorized aids.

I declare that I have read, understood, and complied with the guidelines of the senate of the Montanuniversität Leoben for "Good Scientific Practice".

Furthermore, I declare that the electronic and printed version of the submitted thesis are identical, both, formally and with regard to content.

December 2020

Sandra Baltic

Contents

1	Introduction	15
1.1	Continuum mechanics foundations	18
1.2	Characterization of the stress state	23
1.3	Continuum Damage Mechanics.....	26
1.4	Finite element discretization	29
2	Coupled damage variable based on fracture locus: Modeling and calibration .	35
2.1	Introduction and motivation	36
2.2	Towards a fully coupled damage plasticity model: governing equations..	42
2.3	Ductile fracture experiments and model calibration	48
2.4	Results and discussion	58
2.5	Conclusions.....	68
3	Coupled damage variable based on fracture locus: Prediction of ductile failure in a complex structure	71
3.1	Introduction and motivation	72
3.2	Computational model: calibration from laboratory specimens	75
3.3	Application to a complex structure exposed to multiaxial loading.....	83
3.4	Results and discussion	86
3.5	Summary and conclusion	91
4	Ductile crack formation modeling in pre-cracked solids using coupled fracture locus theory.....	93
4.1	Introduction	94
4.2	Experiments	95
4.3	Computational model.....	98
4.4	Numerical results	100
4.5	Summary and conclusion	105
5	Machine learning assisted calibration of a ductile fracture locus model	106
5.1	Introduction	107
5.2	Constitutive model: governing equations	109
5.3	Computational framework for material parameter identification.....	111
5.4	Results and discussion	125
5.5	Summary and conclusion	133
6	Summary	135
7	Appendices	149

List of Figures

Fig. 1.1. Motion of body B: initial ($t = 0$) and current configuration ($t > 0$), transformation of a line element.	19
Fig. 1.2. An illustrative representation of the elasto-plastic material behavior.....	21
Fig. 1.3. Decomposition of the stress tensor. Adapted from (Öchsner 2016).....	24
Fig. 1.4. The space of principal stresses: Cartesian coordinate system ($\sigma_1, \sigma_2, \sigma_3$) and cylindrical coordinate system (ξ, ρ, θ).....	25
Fig. 1.5. Typical engineering stress-strain curve of a ductile aluminum alloy (AlMgSi0.5). The region of multiaxial stress upon elasto-plastic deformation is highlighted. Adapted from (Öchsner 2016).	27
Fig. 1.6. Schematic representation of an undeformed (undamaged) and deformed (damaged) tensile specimen. Adapted from (Öchsner 2016).....	28
Fig. 1.7. Eight node solid element (SOLID185 from (ANSYS Documentation)) with associated nodes and local normalized coordinate system (s, t, r).....	30
Fig. 1.8. Incremental Newton-Raphson method.....	31
Fig. 1.9. Incremental Newton-Raphson method with highlighted convergence region.	33
Fig. 2.1. Coupled damage variable for three different loading paths: weakening of the material driven by strain induced damage (schematic representation of Eq. 2.10). The inset shows the fracture locus ϵf in the space of stress triaxiality η and Lode angle parameter θ	46
Fig. 2.2. Tension test samples of aluminum alloy AA1050 designed to capture various stress states.	49
Fig. 2.3. Force-displacement curves of extruded AA1050 in three different orientations with respect to the extrusion flow: $0^\circ, 45^\circ, 90^\circ$	50
Fig. 2.4. Force-displacement curve of AA1050: annealed and work-hardened dog-bone sample.	51
Fig. 2.5. Ductile fracture experiments: force-displacement curves and DIC equivalent strains. The instant prior to failure (★) determines the instant of the onset of fracture.....	53
Fig. 2.6. Critical loading paths: history of the equivalent plastic strain vs. stress triaxiality (a) and Lode angle parameter (b) extracted from FEM simulations of ductile fracture experiments at the critical point.....	55

Fig. 2.7. Identified fracture loci of AA1050. Parameters of the ductile fracture model proposed by (Lou and Huh 2013): $c_1=2.082$, $c_2=0.557$, $c_3=2.423$. The figure shows a fracture locus (surface) together with both loading paths (lines) and fracture strains used for calibration (★).....	56
Fig. 2.8. Representative strain profile for determination of experimentally resolved length scale: (a) planar distribution of the equivalent plastic strain determined by Digital Image Correlation and (b) approximation of the central strain profile by Eq. 2.23 with $l=0.195$ mm and $\epsilon_0=1$	57
Fig. 2.9. Calibration process of the parameter L controlling the amount of regularization: the iterative fitting procedure by comparing experimental and simulated force-displacement curves. The length scale parameter l is fixed ($l = 0.195$ mm).	58
Fig. 2.10. Experimental vs. numerically predicted force-displacement curves of various tests: The FEM simulations use a coupled damage model.	59
Fig. 2.11. Scanning Electron Microscope (SEM) micrographs of various ductile fracture mechanisms: (a) ductile failure due to void growth and coalescence observed at the failure site of the notched specimen R025, (b) shear dominant failure and sheared voids at the failure site of the shear specimen 0° , (c) mixed mode failure: combination of ductile and shear failure observed at the failure site of a dog-bone sample.	60
Fig. 2.12. Shear sample: (a) fracture surface and (b) force-displacement curves of coupled and uncoupled damage model compared with experiment, where the inset shows FE mesh.	61
Fig. 2.13. Shear tension sample: (a) Equivalent plastic strain (specimen surface): Digital Image Correlation (DIC) vs. simulated distribution of the equivalent plastic strain and (b) plot of damage with the critical element reaching damage $D=1$ (specimen center), distribution of stress triaxiality and Lode angle parameter.....	63
Fig. 2.14. Notched tension sample: (a) fracture surface and (b) force-displacement curves of coupled and uncoupled damage model compared with experiment. The inset shows the FE mesh.	64
Fig. 2.15. Notched tension sample: (a) Equivalent plastic strain (specimen surface): experimentally measured (DIC) vs. simulated distribution of plastic strain, (b) damage parameter at the critical element reaching damage $D=1$, distribution of stress triaxiality and Lode angle parameter.	64
Fig. 2.16. Loading path of the dog-bone tension specimen: history of the equivalent plastic strain as a function of stress triaxiality and Lode angle parameter.....	65
Fig. 2.17. Dog-bone tension test: (a) fracture surface and (b) force-displacement curves of coupled and uncoupled model compared with an experiment.	66
Fig. 2.18. Dog-bone tension test: (a) Equivalent plastic strain (specimen surface): experimental Digital Image Correlation (DIC) vs. simulated using coupled damage model and (b) plot of damage with the critical element reaching damage $D=1$, distribution of stress triaxiality and Lode angle parameter (specimen center).....	67

Fig. 2.19. Regularization of shear bands using large-deformation gradient theory proposed by (Anand et al. 2012). Standard equivalent plastic strain εP ; nonlocal plastic strain eP representing a weighted average of εP neutralizing the width of the band by the difference of εP and eP having a positive contribution in the center of strain localization and negative one at the edges (specimen surface)..... 68

Fig. 3.1. Material characterisation: specimens cut out from a thin-walled aluminum component. (a) geometry of the structural component, (b) specimen geometries machined from the bottom part of 0.55 mm thickness: dogbone, notched and shear tension specimens. 75

Fig. 3.2. Experimental characterization of flow anisotropy: (a) dogbone specimens machined in different orientations with respect to extrusion flow from the bottom section, (b) force displacement curves of differently oriented dogbone specimens, (c) plastic width strain versus plastic thickness strain curve. 78

Fig. 3.3. Coupled damage variable for three different loading paths (Baltic et al. 2020a): weakening of the material driven by strain induced damage (schematic representation of Eq. 3.1). The inset shows the fracture locus εf in the space of stress triaxiality η and Lode angle parameter θ 79

Fig. 3.4. Experimental vs. numerically predicted force-displacement curves of basic ductile fracture experiments and DIC equivalent strains (Baltic et al. 2020a): tensile tests of specimens undergoing various stress states. The star (★) marks the instant prior to failure..... 81

Fig. 3.5. Experimentally vs. numerically predicted force-displacement responses of a miniature dogbone specimen and a twice larger dogbone specimen. The star (★) marks the instant prior to failure. For the miniature dogbone the length scale parameter is $l = 0.195$ mm; for the larger dogbone the length scale parameter is $l_s = 0.390$ mm..... 83

Fig. 3.6. Geometrical details of the analysed structure: outside and cross section views of the thin-walled aluminum component 84




Fig. 3.7. Simulation model of the analysed mechanical system: (a) outside and cross section views, (b) 3D view with indicated boundary conditions: symmetry planes (), displacement in Y-direction set to zero on the top surface (), pressure on the interior surfaces (). The inset shows the gauge width w_s where the shear band forms. 85

Fig. 3.8. Finite element model of the thin-walled structure: non-conformal mesh in the safety vent region 86

Fig. 3.9. Experimental vs. numerically predicted results for thin-walled aluminum component: (a) burst pressure for a variety of membrane thicknesses and (b) deformation prior to failure..... 87

Fig. 3.10. Overview of the fracture surface of the failed aluminum component after testing: (a) Scanning Electron Microscopy (SEM) micrographs show a ductile fracture mechanism in the structure, revealing a sheared fracture surface; the

centrepiece is broken out. (b) overlap of the stress triaxiality and Lode angle parameter contour lines from the simulation.	88
Fig. 3.11. Comparison of the failure mechanism predicted by the numerical model with the SEM documentation of the failed component: plot of damage as well as distributions of stress triaxiality and Lode angle parameter in the damaged zone. .	89
Fig. 3.12. The localization band in the structure for various 3 mesh discretizations of the FE model: plot of the equivalent plastic strain ϵ_p	91
Fig. 4.1. Geometrical details of the pre-cracked specimen. The hatched areas of the specimen indicate the clamping regions.....	96
Fig. 4.2. Digital microscope image of the final specimen geometry showing the introduced pre-crack (close-up).....	96
Fig. 4.3. Experimental results for tensile specimens with a side notch and a pre-crack: (a) force-displacement curve and DIC analysis of a specimen exhibiting a failure path of type A and (b) a specimen exhibiting a failure path of type B.	98
Fig. 4.4. Finite element model of the pre-cracked specimen. The finite elements along the marked (dashed) line are separated in y-direction to model the pre-crack. One half of the model is shown due to the symmetry in z-direction.	99
Fig. 4.5. Numerical study of the response of the pre-cracked specimen under different boundary conditions (BC): numerically predicted failure path for applied DIC-measured displacement history (BC-DIC) compared to a model of an ideally clamped specimen with fixed lower specimen boundary (BC-fixed); for samples A and B.	102
Fig. 4.6. Comparison of experimentally recorded (EXP) and numerically calculated (FEM) force-displacement curves for (a) sample A and (b) sample B; the insets show the equivalent strains recorded by Digital Image Correlation (DIC) and calculated numerically (FEM). Visualisation of the numerically computed evolution of stress triaxiality, Lode angle parameter and damage in sample A (c) and sample B (d); the plots show the fields in the center plane of the sample.....	104
Fig. 5.1. Finite element model of the shear tension specimen.....	112
Fig. 5.2. Design of numerical experiments following the three level full factorial: 3-variable system with 3 levels (0 = low value, 1 = middle value, 2 = high value) arranged on the middle edge nodes (○), corner edge nodes (●) and centre nodes (●).	113
Fig. 5.3. Passing the training database from FE to ANN throughout the complete numerical experiment: (a) images of the local displacement field in X and Y direction (UX and UY) for every time step t, (b) global force-displacement curve values for every time step t.....	115
Fig. 5.4. Different ANN architectures studied: models A, B and C.	116
Fig. 5.5. Model summary of different ANN architectures: (a) model A, (b) model B, (c) model C.	121

Fig. 5.6. Application of the trained ANN model: feeding the experimental data of the shear tension specimen into the trained ANN. (a) local displacement fields obtained from DIC analysis and (b) global force-displacement curve.	124
Fig. 5.7. Verification of the ANN models: results of the FE model predictions (FEM) for numerical test cases (FE test case) using parameter sets determined by different ANN architectures (ANN_A, ANN_B, ANN_C); the inserted numbers (1 - 8) on each individual graph represent the number of the FE test case; (a) results for the FE models covering the middle nodes of each of the 8 cubes; (b) results for the FE models designed according to the Latin hypercube sampling.....	127
Fig. 5.8. Comparative statistics of different ANN network outputs on verification data. (a) FE models covering the middle nodes of each of the 8 cubes; (b) FE models designed according to the Latin hypercube sampling. The box plots show the statistics obtained by 10 independent optimization outcomes of the ANN and the green dotted lines show the true value, used in the FE model to generate the test data, for comparison.....	129
Fig. 5.9. Comparative statistics of different ANN network outputs on the experimental data.....	130
Fig. 5.10. Validation of the ANN model: FE model predictions of the experimental force displacement curves using material parameters determined by different ANN architectures (ANN_A, ANN_B, ANN_C).....	131
Fig. 5.11. Comparison of local equivalent total strain distributions documented experimentally using Digital Image Correlation (DIC) and calculated numerically (FEM) at three stages (1, 2 and 3). The FE simulation (FEM) shows the results using the set of parameters predicted by ANN model architecture A.	132
Fig. 5.12. Comparison of numerically predicted force-displacement curves using the set of parameters given by ANN model A for multiple geometries covering various stress states. The experimental data is taken from (Baltic et al. 2020a).	132

List of Tables

Table 2.1. Summary of selected ductile fracture models representing typical modeling approaches	37
Table 2.2. List of abbreviations.....	49
Table 2.3. Material parameters used for modeling aluminum alloy AA1050	58
Table 3.1. Material parameters used for modeling the aluminum alloy AA1050 (Baltic et al. 2020a).....	81
Table 5.1. Material parameters to be identified by the ANN.....	111
Table 5.2. ANN training database developed following a three level full factorial design.....	113
Table 5.3. FE test cases covering the middle points of each of the 8 cubes.....	115
Table 5.4. FE test cases selected according to the Latin hypercube sampling	116
Table 5.5. Identified material parameters after feeding the experimental data of the shear tension specimen into ANN.....	130
Table 5.6. List of abbreviations.....	133

Acknowledgements

I would like to thank Professor Thomas Antretter, Head of Institute of Mechanics and my doctoral father, for his continuous support and always encouraging feedback over the past three years. Thanks to his outstanding expertise and excellent advising I could to learn a lot that I will take with me into the future. I am proud and grateful that I could have been his PhD student.

I am thankful and highly appreciate the collaboration with René Hammer, the project leader at MCL who guided me through the interesting project that we have worked on during my PhD time. Our daily discussions have definitely had an important impact on my approach to research. I am happy and grateful to have been given the opportunity to be a part of this research project.

I would like to thank Hans-Peter Gänser for his time and effort invested in our discussions. I highly appreciate his outstanding expertise and am grateful for his advices and encouragements that enriched me both as a researcher and as a person.

Special thanks are due to my office colleague Johann Riedler at MCL who made it easier for me to enter the world of programming. My appreciation goes also to my MCL colleagues Julien Magnien and Zhian Asadzadeh for excellent collaboration.

Thanks are due to all members of the MCL Simulation Group for a great working atmosphere and our coffee breaks. I could not have asked for a better working environment than the one at the MCL and Montanuniversität Leoben. Thank you all.

I would like to thank my dear friends in Austria who welcomed me here with delight and made my PhD time unforgettable. My special thanks goes to my boyfriend for his love, support and faith in me.

In the end I would like to thank my family in Croatia for their unconditional support and encouragement for PhD study even across the borders.

Dedicated to my beloved grandparents.

Abstract

This thesis introduces a numerical model for describing damage processes and fracture in a severely strain-hardened aluminum alloy. The macroscopic phenomenology and fracture mechanisms of sheet-metal specimens as well as thin-walled structures have been studied experimentally and numerically for various loading conditions. The model's essential feature is capturing different fracture mechanisms under various stress states. This has been accomplished by introducing a stress state dependent damage variable in the elasto-plastic constitutive behavior. A custom material model with nonlocal regularization has been implemented into commercial finite element software. The model has not only been applied to modeling uncracked and pre-cracked alloy specimens, but has also been put at test in a complex loading scenario occurring in a real world mechanical component. The model's true predictive ability has been assessed thereby. The model predictions for various geometrical as well as loading scenarios are found to be in very good agreement with experimental findings. This has been accomplished even for fundamentally different damage and fracture processes without any changes of the material model. Furthermore, a simplified method for determination of material constants has been introduced that assists traditional inverse identification of parameters by artificial intelligence based on machine learning methods. All research findings together encourage the general use of the constitutive model for the design of aluminum and other sheet-metal structures.

Zusammenfassung

Diese Arbeit stellt ein numerisches Modell zur Beschreibung von Schädigungsprozessen bis hin zum Bruch einer kaltverfestigten Aluminiumlegierung vor. Die makroskopische Phänomenologie und die Bruchmechanismen von Blechproben sowie die dünnwandige Struktur wurden experimentell und numerisch für verschiedene Belastungsbedingungen untersucht. Das wesentliche Merkmal des Modells ist die Erfassung verschiedener Bruchmechanismen unter verschiedenen Spannungszuständen. Dies wurde durch die Einführung einer spannungszustandsabhängigen Schadensvariable in das elasto-plastische Konstitutivgesetz des Materials erreicht. Ein benutzerdefiniertes Materialmodell mit einer nichtlokalen Regularisierung wurde in kommerzielle Finite-Elemente-Software implementiert. Das Modell wurde nicht nur zur Modellierung von ungerissenen und vorgerissenen Proben angewendet, sondern auch für komplexere Belastungsszenarien getestet, wie sie in realen mechanischen Komponenten auftreten. Die Vorhersagen des Modells stimmen für alle untersuchten Szenarien sehr gut mit den experimentellen Ergebnissen überein. Dies wurde auch bei grundlegend unterschiedlichen Schadens- und Bruchprozessen ohne Änderung des Materialmodells erreicht. Darüber hinaus wurde eine vereinfachte Methode zur Bestimmung von Materialkonstanten eingeführt, welche die traditionelle inverse Identifizierung von Parametern durch künstliche Intelligenz auf Basis der Methoden des maschinellen Lernens unterstützt. Die präsentierten Forschungsergebnisse bestätigen die allgemeine Anwendbarkeit des konstitutiven Modells für das Design von Aluminium- und anderen Blechstrukturen.

Publications and Outline

The thesis is composed of an introductory part (Chapter 1) followed by the executive parts (Chapter 2, 3, 4 and 5) consisting of journal publications, published or submitted for publication. A list of referred journal publications with reference to the chapters of the thesis is given below. Chapter 6 closes the work and summarizes the main results.

Baltic, S.; Magnien, J.; Gänser, H.-P.; Antretter, T.; Hammer, R. (2020a): Coupled damage variable based on fracture locus: Modeling and calibration. In: <i>International Journal of Plasticity</i> 126, S. 102623. DOI: 10.1016/j.ijplas.2019.11.002.	Chapter 2
Baltic, S.; Magnien, J.; Gänser, H.-P.; Antretter, T.; Hammer, R. (2020b): Coupled damage variable based on fracture locus: Prediction of ductile failure in a complex structure. In: <i>International Journal of Solids and Structures</i> 207, S. 132-144. DOI: 10.1016/j.ijsolstr.2020.10.018.	Chapter 3
Baltic, S.; Magnien, J.; Kolitsch, S.; Gänser, H.-P.; Antretter, T.; Hammer, R.: Ductile crack formation modeling in pre-cracked solids using coupled fracture locus theory, submitted for publication in a peer-reviewed journal, 2020.	Chapter 4
Baltic, S.; Asadzadeh, M. Z.; Hammer, P.; Magnien, J.; Gänser, H.-P.; Antretter, T.; Hammer, R.: Machine learning assisted calibration of a ductile fracture locus model (2021). In: <i>Materials & Design</i> 203, S. 109604. DOI: 10.1016/j.matdes.2021.109604	Chapter 5

Chapter 1

Introduction

Aluminum structures have shown their great potential for widespread applications, from large landmark buildings (e.g. all of the Empire State Building's basic structures), over car bodies to tiny microelectronic components (e.g. microchips and capacitors). Today there is an increasing trend of making use of aluminum for vehicle structure design to minimize the weight while maximizing structural stiffness. Finally, with rapid development of the microelectronics industry, commercial off-the-shelf engineering aluminum alloys have become a standard in the production of electronic components.

Ductility and favorable strength to weight ratio featuring aluminum alloys are central to designing safe and reliable components. Premature failures and excessive deformations are unwanted scenarios that disrupt the functionality and safety of the components. In preventing their catastrophic failures computational mechanics with its existing and emerging methods plays a central role. A constant quest for reliable material models that can predict large deformations, ductile damage over the structure's life cycle and finally structural failure has given rise to worldwide efforts over the past decade to benchmark the computational methods available. Three Sandia Fracture Challenges (Boyce et al. 2014; Boyce et al. 2016; Kramer et al. 2019) have been launched by Sandia National Laboratories¹, inviting the research groups to report the numerical predictions of deformation and damage in specimens of novel geometries without knowing the experimental outcome. While some results were more encouraging than others, they underscored the need for more sophisticated, yet useable models for real world applications, leaving the ductile fracture predictions challenging.

¹ Sandia National Laboratories research group is a Federally Funded Research and Development Center (FFRDC). It operates as a contractor for the U.S. Department of Energy's National Nuclear Security Administration (NNSA) and supports numerous federal, state, and local government agencies, companies, and organizations.

STATE-OF-THE-ART

From a micromechanical point of view, ductile fracture comprises void generation, growth and coalescence to a macrocrack. The cylindrical void growth model (McClintock 1968b), the spherical void growth model (Rice and Tracey 1969), damage mechanics (Lemaitre 1985), porous plasticity (Gurson 1977; Tvergaard and Needleman 1984), fracture criterions like e.g. (Johnson and Cook 1985) all belong to the class of macroscopic models developed to describe the ductile fracture of metals. The fundamental mechanisms of ductile fracture are rather well understood (see e.g. the reviews of (Pineau et al. 2016; Benzerga et al. 2016; Besson 2009)). A detailed overview of different modeling approaches is given in Chapter 2. However, the choice of the material model to simulate ductile fracture in a metal structure is not straightforward due to the variety of the modeling approaches available.

This work is concerned with the macroscopic aspect of fracture relying on the equivalent strain to fracture, i.e. the local maximum of the equivalent plastic strain just before the final failure (the instant of the material separation), referred to as the fracture strain in the continuation. Ductile fracture criteria based on fracture strain measurements attracted great attention by researchers both in distant (McClintock 1968b; Rice and Tracey 1969; Hancock and Mackenzie 1976; Johnson and Cook 1985) and in more recent (Bao and Wierzbicki 2004; Bao and Wierzbicki 2005; Dunand and Mohr 2010; Roth and Mohr 2018) past. They provided ample evidence that the fracture strain of the material is not constant but rather a complex function of the local stress state evolution. This concept will be termed hereinafter the local fracture strain concept.

To establish a fracture model for an uncracked structure, one can define a measure of the material damage D on the basis of the above (stress state dependent) local fracture strain concept. (Fischer et al. 1995) and (Gänser et al. 2000) referred to as damage indicator, as the damage is used to indicate the onset of a local crack in a structure. The damage indicator does not influence the material's elastic-plastic behavior and thereby belongs to a so-called uncoupled damage concept. As much as this is computationally efficient, it is not sufficient for describing the damaging process. This requires more sophisticated approaches such as e.g. porous plasticity (Gurson 1977) or Lemaitre's damage mechanics (Lemaitre 1985). These models are termed coupled damage concepts as they allow for strain softening due to damage in the elasto-plastic constitutive description of the material. They, however, require higher computational effort and more complex numerical implementation.

As to the real world demands, the trend is clear. The industry seeks computational models that save time and costs to stay ahead of the competition. Design decision have to be made faster than ever. Consequently, rather simple models are preferred over more complicated and time-consuming models. For these reasons, uncoupled damage concepts are extensively used in applied mechanics so far (Bao and Wierzbicki 2004; Dunand and Mohr 2010; Khan and Liu 2012; Roth and Mohr 2016; Lou et al. 2017; Deole et al. 2018; Ha et al. 2018; McDonald et al. 2019). This work aims

at complementing the current standards in FE modeling of ductile materials, taking into account both state-of-the-art theoretical knowledge and industrial requirements.

OBJECTIVES, APPROACHES AND NOVEL ASPECTS

The objective of the thesis is to model the damaging process and fracture of a severely strain-hardened aluminum alloy prone to necking and strain localization at extremely small deformations. In doing so, it is essential to capture different material behaviors under different regimes, i.e. to describe different fracture mechanisms under various stress states. The numerical model has to ensure:

- a tight correspondence of material model constants with experimentally measurable quantities to minimize the freedom in adjusting the model parameters,
- physics-based model formulation along with using as few parameters as possible,
- mesh independent finite element simulation of a ductile fracture,
- applicability for practical purposes and
- as simple as possible calibration from independent experiments.

These aspects have already been elaborated in the literature individually, yet a single unified model that considers all of them is still missing. In order to meet the above objective, the fracture strain concept is selected among other modeling approaches because, on the one hand, it is simple enough to be easily calibrated as it relies on an experimentally measurable quantity (the strain). On the other hand, it is complex enough to capture the stress state dependency of the fracture process.

However, in contrast to the former approaches from the literature, the present work reports the measured local fracture strains together with their associated length scale, that is, the length scale over which the experimental strains are averaged. This allows to consider the length scale in the computational model and implement a regularization that is a function of the length scale associated with directly measurable quantity, which is attempted here for the first time.

Furthermore, the local fracture strain theory is applied here as a fully coupled concept in a damage mechanics framework, as opposed to the common practice of applying the fracture strain theory as an uncoupled damage concept.

Eventually, an attempt is made to develop a computational framework that simplifies finding the material constants of the presented damage and fracture model. The experimental data of one single specimen is used together with machine learning methods to find a set of material constants applicable not only to the calibration specimen but also to other specimens covering various stress states.

The material model is implemented into commercial finite element software and applied to aluminum structures experiencing a variety of failure mechanisms. All of them are computed using one and the same unique material parameter set.

Chapter 2 introduces a generally applicable damage-plasticity model fulfilling all of the requirements above. The governing equations of the coupled damage concept based on local fracture strain are given and the model calibration from basic ductile fracture experiments is presented.

Chapter 3 demonstrates the theory from Chapter 2 by application to a complex engineering structure and reports experimentally validated numerical predictions of the fracture initiation.

Chapter 4 assesses the fundamental generality of the theory on a pre-cracked structure by comparing experimentally observed and numerically calculated crack propagation paths.

Chapter 5 simplifies the determination of the material model parameters by assisting the calibration procedure with machine learning methods.

The approaches used in this work are based on continuum mechanics and comprise finite element (FE) modeling, classical plasticity theory and the principles of continuum damage mechanics. The following sections of Chapter 1 summarize the continuum mechanics background needed in this work for the finite element formulation of a structural engineering problem.

1.1 Continuum mechanics foundations

The basic equations of continuum mechanics are threefold. Firstly, kinematic relations describe the deformation and motion of a body. They relate the strain to displacement. Secondly, balance equations describe the force equilibrium in the system. Thirdly, the stress is related to a kinematic quantity (e.g. strain) through constitutive equations. Here, a concise overview of the continuum mechanical foundation is presented as the basis for a finite element analysis of a ductile fracture within a continuum approach. Further details on continuum mechanics topics relevant to this thesis can be looked up in the literature, e.g. (Lemaitre and Chaboche 1990; Bonet and Wood 1997; Wriggers 2008; Mase et al. 2010).

KINEMATIC EQUATIONS

Consider a continuous body B occupying a domain Ω in a three-dimensional Euclidean space. For time $t = 0$ the material point P has an initial position \mathbf{X} (the position vector in the initial configuration). For time $t > 0$ the body B takes another configuration, see Fig. 1.1. The motion of the point P can be explained by mapping

$$\mathbf{x} = \chi(\mathbf{X}, t). \quad (1.1)$$

The displacement vector is given by

$$\mathbf{u} = \mathbf{x} - \mathbf{X}. \quad (1.2)$$

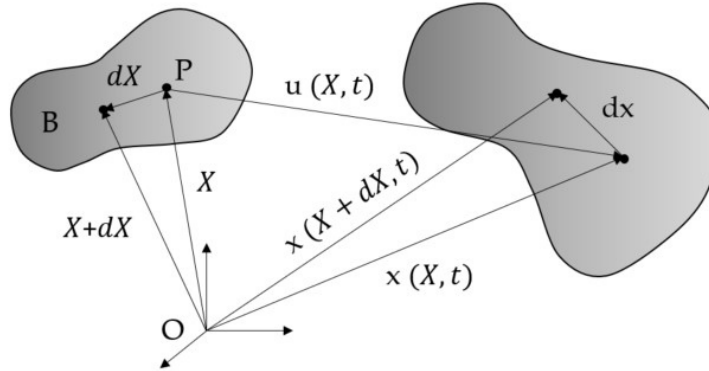


Fig. 1.1. Motion of body B : initial ($t = 0$) and current configuration ($t > 0$), transformation of a line element.

Consider now a line element in the body B defined by vector $d\mathbf{X}$, see Fig. 1.1. To mathematically describe the deformation process on a local level, a tensor \mathbf{F} is introduced. It relates the tangent vectors of initial (\mathbf{X}) and current configuration (\mathbf{x}) to each other, i.e., it maps a material line element of the initial configuration $d\mathbf{X}$ to a line element $d\mathbf{x}$ of the current configuration \mathbf{x} :

$$d\mathbf{x} = \mathbf{F} d\mathbf{X} \quad (1.3)$$

where the structure of the Eq. (1.3) already suggests that \mathbf{F} represents a gradient,

$$\mathbf{F} = \frac{\partial \mathbf{x}}{\partial \mathbf{X}} \quad (1.4)$$

and hence it is called deformation gradient. The same can be written in terms of the displacement (Eq. 1.2.) as

$$\mathbf{F} = \mathbf{I} + \frac{\partial \mathbf{u}}{\partial \mathbf{X}} \quad (1.5)$$

where \mathbf{I} is the identity matrix. The deformation gradient \mathbf{F} contains the information about the volume change, the rotation and the shape change of a deformable body. The volume change is determined by

$$\frac{dV}{dV_0} = \det \mathbf{F} \quad (1.6)$$

with V and V_0 denoting current and original volume. The rotation and shape change contained in the deformation gradient \mathbf{F} can be separated by applying the right polar decomposition theorem,

$$\mathbf{F} = \mathbf{R} \mathbf{U} \quad (1.7)$$

where \mathbf{R} is the rotation matrix ($\mathbf{R}^T \mathbf{R} = \mathbf{I}$) and \mathbf{U} is the right stretch (shape change) matrix. Once the matrix \mathbf{U} is known, a logarithmic or Hencky strain measure is defined,

$$\boldsymbol{\varepsilon} = \ln \mathbf{U} \quad (1.8)$$

with $\boldsymbol{\varepsilon}$ being the Hencky strain tensor.

To explain the change of length of a line element, another strain measure, i.e. Green-Lagrange strain tensor \mathbf{E} formulated in the initial configuration is introduced,

$$\mathbf{E} = \frac{1}{2}(\mathbf{F}^T \mathbf{F} - \mathbf{I}) = \frac{1}{2}(\mathbf{C} - \mathbf{I}). \quad (1.9)$$

where $\mathbf{C} = \mathbf{F}^T \mathbf{F}$ is the right Cauchy-Green tensor. The left Cauchy-Green tensor $\mathbf{B} = \mathbf{F} \mathbf{F}^T$ is used in the Almansi strain tensor, the strain measure formulated in the current configuration,

$$\mathbf{e} = \frac{1}{2}(\mathbf{I} - \mathbf{F}^{-T} \mathbf{F}^{-1}) = \frac{1}{2}(\mathbf{I} - \mathbf{B}^{-1}). \quad (1.10)$$

Because the plastic behavior of a ductile material is history-dependent, a time-dependence of the deformation $\chi(\mathbf{X}, t)$ has to be considered. Therefore, we need time derivatives of the kinematic quantities. The first and second derivatives with respect to time define the velocity and acceleration of a material point in regard to the reference configuration, respectively:

$$\mathbf{v}(\mathbf{X}, t) = \frac{\partial \chi(\mathbf{X}, t)}{\partial t} \quad (1.11)$$

$$\mathbf{a}(\mathbf{X}, t) = \frac{\partial^2 \chi(\mathbf{X}, t)}{\partial t^2} = \frac{\partial \mathbf{v}(\mathbf{X}, t)}{\partial t} \quad (1.12)$$

BALANCE EQUATIONS

During the deformation process, conservation laws for mass, momentum, angular momentum etc. must be fulfilled. Therefore, the change of mass in a system has to be zero ($\dot{m} = 0$). This means that the mass of an infinitesimally small element in initial and current configuration must be equal. If ρ and ρ_0 denote the densities in initial and current conditions, respectively, the mass balance is given by

$$\rho dV = \rho_0 dV_0, \quad (1.13)$$

or by the rate form of mass continuity,

$$\frac{\partial \rho}{\partial t} + \nabla \cdot (\rho \mathbf{v}) = 0, \quad (1.14)$$

where \mathbf{v} is the velocity field. The balance of linear momentum can be stated as

$$\nabla \cdot \boldsymbol{\sigma} + \rho \mathbf{b} = \rho \frac{\partial \mathbf{v}}{\partial t}, \quad (1.15)$$

where \mathbf{b} stands for the body force density per unit mass. $\boldsymbol{\sigma}$ is the Cauchy stress tensor. $\rho \mathbf{b}$ describes the volume forces, such as gravitational force, acting on a body B . $\rho \frac{\partial \mathbf{v}}{\partial t}$ defines the inertial forces. They are negligible for quasi-static problems. The local balance of angular momentum demands the Cauchy stress tensor $\boldsymbol{\sigma}$ to be symmetric, i.e.

$$\boldsymbol{\sigma} = \boldsymbol{\sigma}^T. \quad (1.16)$$

The conservation of energy known as the first law of thermodynamics says that the change of total energy E equals to the sum of the mechanical power P of all external loads and the heat supply Q ,

$$\dot{E} = P + Q. \quad (1.17)$$

The first law of thermodynamics can be recast in a local form,

$$\rho \dot{u} = \boldsymbol{\sigma} : \mathbf{d} + \rho r - \nabla \cdot \mathbf{q}, \quad (1.18)$$

where u is the specific internal energy, \mathbf{d} is the velocity gradient ($\boldsymbol{\sigma} : \mathbf{d}$ is known as a specific stress power), r is the internal heat source and \mathbf{q} is the heat flux vector. In finite element modeling, it is good practice to verify the validity of the solution by checking the energy balance.

CONSTITUTIVE EQUATIONS

Constitutive theories describe the material's response (macroscopic or microscopic) to applied loads and are theoretically sound only if they obey the thermodynamic principles, the conservation of energy and the positivity of the entropy rate.

Aluminum, the material studied here, depicts a nonlinear behavior and can be described by the assumption of an elasto-plastic behavior. The model presented in this thesis is restricted to rate-independent plasticity theory for the case of isotropic hardening of a metal. Fig. 1.2. illustrates the elasto-plastic constitutive behavior. The material responds elastically up to the point A. The plastic deformation occurs once the stress has reached the flow stress σ_A in the point A and the stress does not increase linearly any further, but follows a hardening law. In the point B, a material instability occurs and entails necking and/or shear bands. The region B-C characterizes a decrease of the flow stress related to geometrical (necking) and possible material (softening) effects.

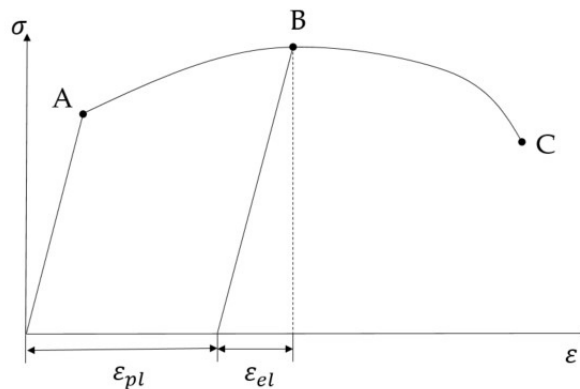


Fig. 1.2. An illustrative representation of the elasto-plastic material behavior.

In a small strain framework elasto-plastic constitutive theories start with decomposing the total strain $\boldsymbol{\varepsilon}$ additively into an elastic $\boldsymbol{\varepsilon}_{el}$ and a plastic strain $\boldsymbol{\varepsilon}_{pl}$,

$$\boldsymbol{\varepsilon} = \boldsymbol{\varepsilon}_{el} + \boldsymbol{\varepsilon}_{pl}. \quad (1.19)$$

For arbitrary loading paths, the incremental strain is decomposed into elastic and plastic strain increments,

$$d\boldsymbol{\varepsilon} = d\boldsymbol{\varepsilon}_{el} + d\boldsymbol{\varepsilon}_{pl}. \quad (1.20)$$

As the elastic deformations in the aluminum structure studied (see Chapter 3) are rather small compared to the plastic deformations, the elastic strain part is not of special interest in this thesis. The classical Hooke's law in its simplest form for the isotropic case is sufficient and adopted here to relate the stresses and strains in the elastic regime,

$$\boldsymbol{\sigma} = \mathbf{C} : \boldsymbol{\varepsilon}_{el}, \quad (1.21)$$

where \mathbf{C} is the stiffness tensor.

On the other hand, the plastic deformation is of a particular interest here. The essential characteristics of a plasticity model are represented by three sets of equations. First, the borderline between elastic and plastic behavior is defined by a yield criterion. Second, a flow rule describes the increment of the plastic strain from the load increment. And third, the evolution of the yield criterion with plastic strain is given by a hardening rule .

The stress at which yielding initiates is determined by the yield criterion, a scalar function of the stress tensor $\boldsymbol{\sigma}$ and a set of material (scalar and tensor) internal variables κ ,

$$f(\boldsymbol{\sigma}, \kappa) = 0. \quad (1.22)$$

A general representation (Eq. 1.22) of the specific yield criterion defines a surface in the stress space.

Elastic deformation is the result of the stress states within the yield surface. The yielding starts once the stress state has reached the yield surface and further loads cause the plastic deformation. Generally, three cases have to be distinguished,

$$f(\boldsymbol{\sigma}, \kappa) < 0, \quad (1.23)$$

$$f(\boldsymbol{\sigma}, \kappa) = 0 \text{ and } \dot{f}(\boldsymbol{\sigma}, \kappa) < 0, \quad (1.24)$$

$$f(\boldsymbol{\sigma}, \kappa) = 0 \text{ and } \dot{f}(\boldsymbol{\sigma}, \kappa) = 0, \quad (1.25)$$

which define the conditions for elastic behavior (Eq. 1.23), elastic unloading (Eq. 1.24) and plastic flow (Eq. 1.25).

Stress states outside of the yield surface do not exist. The plastic strain and the yield surface evolve, maintaining the stresses either in or on the yield surface. In this work, the classical von Mises idealization of the yield surface is adopted.

The plastic strain evolution is given by the flow rule,

$$d\boldsymbol{\varepsilon}_{pl} = d\lambda \frac{\partial Q}{\partial \boldsymbol{\sigma}} \quad (1.26)$$

with $d\lambda$ as the magnitude of the plastic strain increment and Q is the plastic potential. If the plastic potential Q is identical to the yield surface given by (Eq. 1.22.), i.e.

$$d\boldsymbol{\varepsilon}_{pl} = d\lambda \frac{\partial f(\boldsymbol{\sigma}, \kappa)}{\partial \boldsymbol{\sigma}} \quad (1.27)$$

the plastic strain increment is normal to the yield surface. This is called an associative flow rule, frequently used for metals. The result is a plastic strain increment proportional to the stress increment. For soils and granular materials where internal friction sliding leads to plastic deformation, non-associative flow rules are used instead.

Furthermore, a hardening rule determines the change of the yield criterion upon loading. As the material further deforms plastically, the yield stress evolves, in other words the yield surface moves, grows or shrinks. In this work, an isotropic hardening rule of the form

$$F(\boldsymbol{\sigma}) - \sigma_y(\kappa) = 0 \quad (1.28)$$

is adopted, where $F(\boldsymbol{\sigma})$ is a scalar function of the stress and $\sigma_y(\kappa)$ stands for the yield stress. Thus the yield surface evolves uniformly. This hardening type gives good results for structures under monotonic loading, as it is the case in the present work. When the equivalent plastic strain is taken for the hardening variable ($\kappa = \varepsilon_{pl}$), the hardening is referred to as strain hardening.

An essential output quantity specific to the constitutive model of plasticity that will be required for the definition of damage is a path-dependent plastic strain accumulated over the deformation history,

$$\varepsilon_p = \int d\lambda, \quad (1.29)$$

termed hereinafter as the accumulated equivalent plastic strain.

1.2 Characterization of the stress state

Ductile fracture is frequently preceded by large plastic deformations, and considerable stress and strain gradients develop around the fracture point. Multiaxial stress states must be determined accurately on the local level. To this end the stress tensor $\boldsymbol{\sigma}$ is decomposed into its hydrostatic (spherical) and deviatoric part, see Fig. 1.3.

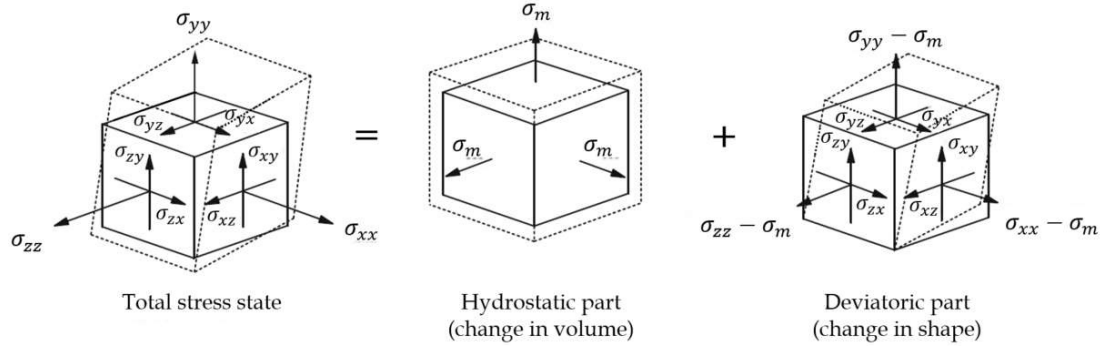


Fig. 1.3. Decomposition of the stress tensor. Adapted from (Öchsner 2016).

Decomposition of the stress tensor $\boldsymbol{\sigma}$ separates the hydrostatic stress tensor $\boldsymbol{\sigma}^o$ characterizing a pure volume change and deviatoric stress tensor \boldsymbol{s} describing a pure shape change, which can be written as

$$\begin{bmatrix} \sigma_{xx} & \sigma_{xy} & \sigma_{xz} \\ \sigma_{xy} & \sigma_{yy} & \sigma_{yz} \\ \sigma_{xz} & \sigma_{yz} & \sigma_{zz} \end{bmatrix} = \begin{bmatrix} \sigma_m & 0 & 0 \\ 0 & \sigma_m & 0 \\ 0 & 0 & \sigma_m \end{bmatrix} + \begin{bmatrix} s_{xx} & s_{xy} & s_{xz} \\ s_{xy} & s_{yy} & s_{yz} \\ s_{xz} & s_{yz} & s_{zz} \end{bmatrix}. \quad (1.30)$$

Assuming an isotropic material, a material model can be formulated using a related set of quantities (p, q, r) defined in terms of the first invariant I_1 of the stress tensor $\boldsymbol{\sigma}$, the second J_2 and third invariant J_3 of the deviatoric tensor \boldsymbol{s} ,

$$p = \frac{1}{3} I_1 = \frac{1}{3} \text{tr}(\boldsymbol{\sigma}) \quad (1.31)$$

$$q = \sqrt{3 J_2} \quad (1.32)$$

$$r = 3 \left(\frac{1}{2} J_3 \right)^{1/3} \quad (1.33)$$

where p is the mean stress² and q is the Von Mises equivalent stress³. The dimensionless hydrostatic pressure η defined by

$$\eta = \frac{p}{q} \quad (1.34)$$

is referred to as the stress triaxiality, an extensively used parameter in the literature on ductile fracture.

The space of principal stresses can be visualized in a Cartesian coordinate system $(\sigma_1, \sigma_2, \sigma_3)$ or a cylindrical coordinate system called Haigh-Westergaard stress space (ξ, ρ, θ) :

$$\xi = \frac{1}{\sqrt{3}} I_1 \quad (1.35)$$

$$\rho = \sqrt{2 J_2} \quad (1.36)$$

² The mean stress is denoted by σ_m in the executive parts (Chapter 2, 3, 4 and 5).

³ Von Mises equivalent stress is also called effective stress in the literature. It is denoted by σ_e the executive parts (Chapter 2, 3, 4 and 5).

$$\cos(3\theta) = \frac{3\sqrt{3}}{2} \frac{J_3}{J_2^{3/2}} \quad (1.37)$$

as shown in Fig. 1.4. The angular coordinate θ is a stress angle termed Lode angle (Lode 1926). The range of the Lode angle is $0 \leq \theta \leq \pi/3$. The value $\cos(3\theta)$ is called Lode angle parameter. The relation of the Lode angle θ to the normalized third invariant J_3 (see (Malvern 1969)) is given by

$$\cos(3\theta) = \left(\frac{r}{q}\right)^3 = \frac{27}{2} \frac{J_3}{q^3}. \quad (1.38)$$

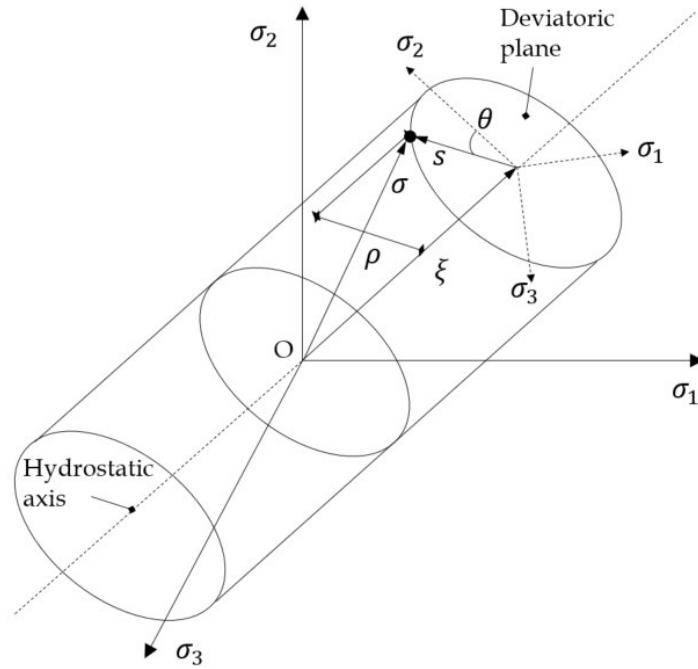


Fig. 1.4. The space of principal stresses: Cartesian coordinate system $(\sigma_1, \sigma_2, \sigma_3)$ and cylindrical coordinate system (ξ, ρ, θ) .

Isotropic material properties are invariant to a rotation of the coordinate system. The stress state at a material point can be uniquely characterized either by three principal stresses $(\sigma_1, \sigma_2, \sigma_3)$ or, on the other hand, by three stress tensor invariants $(I_1, J_2$ and $J_3)$ i.e. their ratios formulated as dimensionless parameters η and θ (Eq. 1.34 and Eq. 1.38).

(Bai 2008) gave the transformation equations from the stress-based form i.e. Cartesian coordinate system of principal stresses $(\sigma_1, \sigma_2, \sigma_3)$ to the spherical coordinate system in the mixed strain and stress invariants space $(\varepsilon_p, \eta, \theta)$. ε_p denotes the equivalent plastic strain. The transformation equations are given by

$$\sigma_1 = p + s_1 = p + \frac{2}{3} \sigma_{eq} \cos \theta = \left(1 + \frac{2 \cos \theta}{3\eta}\right) p \quad (1.39)$$

$$\sigma_2 = p + s_2 = p + \frac{2}{3} \sigma_{eq} \cos\left(\frac{2}{3}\pi - \theta\right) = \left(1 + \frac{2 \cos\left(\frac{2}{3}\pi - \theta\right)}{3\eta}\right) p \quad (1.40)$$

$$\sigma_3 = p + s_3 = p + \frac{2}{3}\sigma_{eq} \cos\left(\frac{4}{3}\pi - \theta\right) = \left(1 + \frac{2 \cos\left(\frac{4}{3}\pi - \theta\right)}{3\eta}\right)p \quad (1.41)$$

where s_1, s_2, s_3 are deviatoric principal stresses expressed in terms of the equivalent stress σ_{eq} and Lode angle θ . The relation of the equivalent stress σ_{eq} to the equivalent strain ε_p is defined by the strain hardening function.

A normalized Lode angle parameter $\bar{\theta}$ in the range of $-1 \leq \bar{\theta} \leq 1$ can be defined by transformation of the Eq. (1.38) to the normalized space and reads

$$\bar{\theta} = 1 - \frac{6\theta}{\pi}. \quad (1.42)$$

The above definition of the Lode angle parameter (Eq. 1.42) from (Bai 2008) will be adopted in this work. A physical interpretation of the parameter $\bar{\theta}$ is that it describes how far the material's stress state is from a pure shear stress state. Therefore, $\bar{\theta} = 0$ represents generalized shear, $\bar{\theta} = 1$ axisymmetric tension and $\bar{\theta} = -1$ axisymmetric compression.

All stress directions can thus be described by the dimensionless parameters stress triaxiality η (Eq. 1.34.) and Lode angle $\bar{\theta}$ (Eq. 1.42.). They will be used in this thesis to characterize the stress states and to define a stress state dependent fracture strain function referred to as the fracture locus.

1.3 Continuum Damage Mechanics

Generally, the concept of ductile damage studies the development of microvoids and pores caused by large plastic deformations. Fig 1.5. shows an engineering stress-strain diagram of a ductile aluminum alloy. The first region characterized by a uniaxial stress state and uniform strain can be very well described by damage-free plasticity theory. On the other hand, the highlighted region where a multiaxial stress state develops often calls for the consideration of material weakening due to microvoids induced by large plastic strains. It is emphasized that this region, characterized by multiaxial stress states, is of particular interest in this research. The first region having uniformly distributed strain is found to be extremely short (see Chapter 2), as opposed to the typical engineering alloys whose representative example is shown in Fig. 1.5.

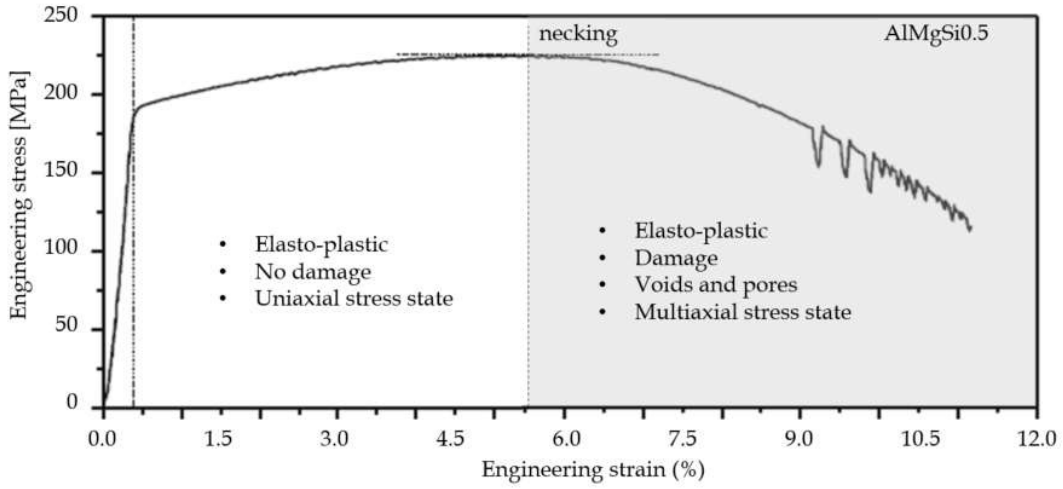


Fig. 1.5. Typical engineering stress-strain curve of a ductile aluminum alloy (AlMgSi0.5). The region of multi-axial stress upon elasto-plastic deformation is highlighted. Adapted from (Öchsner 2016).

There are two different general definitions of damage, both based on a scalar damage variable. The Lemaitre damage concept (Lemaitre 1985, 1986; Krajcinovic and Lemaitre 1987; Lemaitre and Desmorat 2005) defines a surface damage variable, whereas the Gurson damage models (Gurson 1977; Tvergaard and Needleman 1984; Nahshon and Hutchinson 2008) introduce the void volume fraction as the governing quantity

Consider a uniaxial tensile specimen whose representative volume element (RVE) is shown in Fig. 1.6. The initial, undeformed (undamaged) specimen is shown in Fig. 1.6. on the left hand side, whereas the deformed (damaged) specimen is illustrated on the right hand side. The specimen's total cross-sectional area is represented by A . Let A_C be the area of all the voids and microcracks in the cross-sectional area A . The effective area that resists the applied load is A_E . Now the surface damage variable can be defined in terms of these quantities,

$$D = \frac{\sum_i A_{C,i}}{A} = \frac{A_C}{A} = \frac{A - A_E}{A} \quad (1.43)$$

where D is in the range of $0 \leq D \leq 1$. The state $D = 0$ represents the undamaged material and $D = 1$ characterizes the specimen's failure. An alternative description of ductile damage can be defined using the void volume fraction i.e. porosity f . Let V denote the total volume of the RVE, V_C the volume of all the voids in the RVE and V_E the effective volume. Then the void volume fraction is given by

$$f = \frac{\sum_i V_{C,i}}{V} = \frac{V_C}{V} = \frac{V - V_E}{V} \quad (1.44)$$

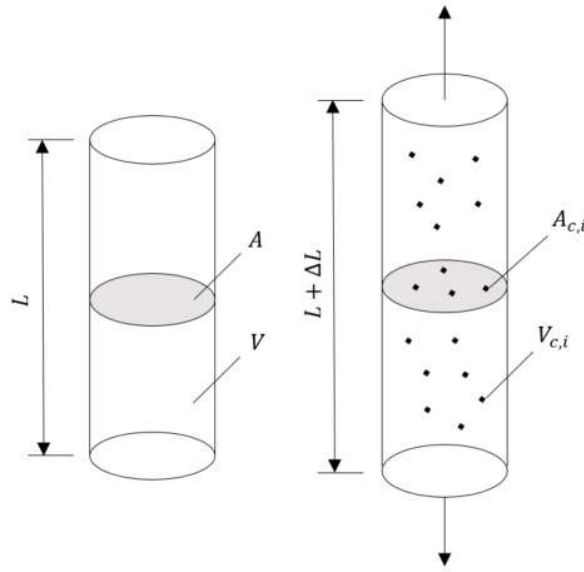


Fig. 1.6. Schematic representation of an undeformed (undamaged) and deformed (damaged) tensile specimen. Adapted from (Öchsner 2016).

A scalar description of damage implies the hypothesis of isotropy, i.e. the same distribution of defects in all directions. If the effective area is used to determine the stresses, the concept of effective stress says that the nominal stress σ is modified by the damage variable D and the effective stress is

$$\bar{\sigma} = \frac{\sigma}{1 - D}. \quad (1.45)$$

Furthermore, the hypothesis of strain equivalence says that the strain of the damaged material can be represented by the strain of the initial material,

$$\bar{\epsilon} = \epsilon. \quad (1.46)$$

Following the above effective stress concept, Hooke's law can be recast as

$$\sigma = (1 - D) E \epsilon \quad (1.47)$$

where E is the elastic modulus of the undamaged material. Furthermore, adaptations of the plasticity theory are required to consider the damage effect. The modified yield condition reads

$$\frac{f(\sigma)}{1 - D} - \sigma_y(\kappa) = 0. \quad (1.48)$$

In damage mechanics, an additional equation describing the evolution of the damage variable is needed. The increment of the damage variable dD in the conventional Lemaitre model has been developed on a thermodynamic basis and reads

$$dD = \frac{d\lambda}{1 - D} \left(-\frac{Y}{r} \right)^s \quad (1.49)$$

where r and s are model parameters. Y is referred to as the damage energy release rate. While the influence of one stress state parameter (stress triaxiality) is hidden in Y , the other essential stress state parameter (Lode angle parameter) is not considered. Therefore, in this work, a different damage evolution law will be adopted. A definition as simple as the linear damage accumulation rule is sufficient to capture all the stress state effects in the damaging process,

$$dD = \frac{d\varepsilon_p}{\varepsilon_f(\eta, \bar{\theta})} \quad (1.50)$$

insofar as the function ε_f describing the fracture locus of the material incorporates the dependency on both stress triaxiality η and Lode angle parameter $\bar{\theta}$. (Fischer et al. 1995; Gänser et al. 2000) referred to D in Eq. (1.50) as damage indicator because it merely indicates the onset of fracture but has no influence on the plastic flow, as opposed to what will be presented in this thesis.

Without any length scale definition in this damage theory, the concept remains restricted to applications to structures where failure is more likely to appear in zones with moderate stress and strain gradients, as already elucidated by (Fischer et al. 1995). To close this gap and be applicable to components where the failure occurs e.g. due to strain localization mechanisms common for sheet-metal structures, a length scale associated with an experimentally observable quantity will be introduced in Chapter 2.

1.4 Finite element discretization

A continuum having a defined boundary is hereinafter referred to as a domain. To solve a real world engineering problem composed of a complex domain subjected to defined boundary conditions, the Finite Element Method (FEM) is employed to find an approximate solution. The domain is decomposed into a finite number of subdomains i.e. finite elements. For every element, unknown field variables are expressed in terms of the assumed approximate functions i.e. interpolation functions. These interpolation functions are formulated by means of the values of the field variables for specific points called nodes.

Within the scope of this work, finite element simulations are performed in ANSYS Mechanical APDL⁴. A custom material model has been implemented to consider the damage (Eq. 1.50.) in the elasto-plastic constitutive equations. Large strain theory as it will be an issue in the aluminum structures is considered by means of updated Lagrangian algorithm.

⁴ APDL stands for Ansys Parametric Design Language and is the programming language used in ANSYS software.

CHOICE OF AN ELEMENT TYPE AND DENSITY

Typically, thin-walled structures are modelled by shell elements in many industrial settings because of their computational efficiency and robustness. Shell element solutions are suitable for modeling large deformation problems unless the fracture i.e. the necking through-the-thickness direction occurs. Therefore, fully three-dimensional mechanical fields are computed in this thesis using fine solid element discretization. In particular, eight node solid elements (SOLID185, (ANSYS Documentation)) having linear shape functions are used for 3D modeling of thin solid structures, see Fig. 1.7. 3D solid element solutions ensure capturing the high ductile fracture dependency on the three-dimensional and multiaxial local stress state developing in the structure. The fracture mechanism preceded by localized necking can be thereby described more accurately in a finite element analysis.

The element density in the region where the localization is expected has to be fine enough to capture this mechanism. The largest applicable element size in the zone of localization is imposed by the experimentally observed strain localization on the tested specimens. Specifically in this work, the resolution of the Digital Image Correlation (DIC) strain measurements dictates the largest finite element size able to capture all local effects observed. A length scale l will be introduced on the basis of an experimentally measurable quantity, that is, the width of the localization band captured by DIC. All finite element models are in the zone of expected localization discretized by fine finite element sizes smaller than the length scale parameter l . Another essential role of the length scale l is to prevent an excessive strain localization in the finite element model induced by the material softening present in the elasto-plastic constitutive equations. This is accomplished by employing a nonlocal regularization, as discussed in detail in Chapter 2.

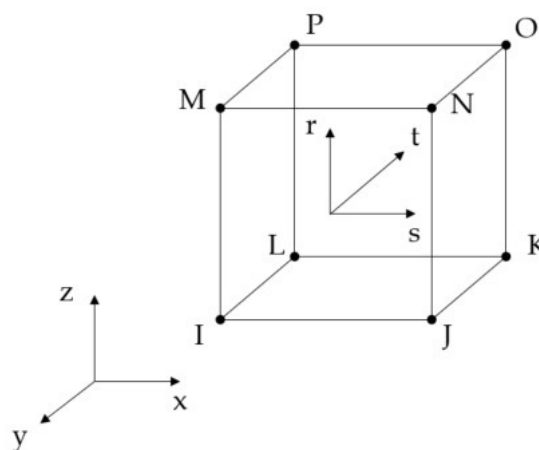


Fig. 1.7. Eight node solid element (SOLID185 from (ANSYS Documentation)) with associated nodes and local normalized coordinate system (s, t, r).

SOLVING A NONLINEAR STRUCTURAL ANALYSIS

The algorithm mostly applied for nonlinear finite element problems is the Newton-Raphson method which can be briefly articulated as follows (for details, see e.g. (Wriggers 2008)).

Let K be the coefficient matrix that is a function of unknown nodal. For a static structural analysis, the discretization by finite elements yields a set of simultaneous equations

$$K(X) u = F^a, \quad (1.51)$$

where vector F^a contains the applied loads. As the plasticity includes path-dependent nonlinearities, the solution requires an incremental analysis to capture the loading path correctly. This means that the final load F^a is applied in increments, see Fig. 1.8. The Newton-Raphson method solves the equations iteratively in every step⁵ (Bathe 1996):

$$K_{n,i}^T \Delta u_i = F_n^a - F_{n,i}^{nr} \quad (1.52)$$

$$\Delta u_{i+1} = u_i + \Delta u_i \quad (1.53)$$

where $K_{n,i}^T$ is the Jacobian (tangent) matrix for time step n , the index i refers to the current equilibrium iteration and $F_{n,i}^{nr}$ represents the restoring loads i.e. element internal loads computed from the current stress state. The general procedure can be summarized as follows:

- Assumption of u_0 . This is typically the converged solution of the previous step (for the first step, $u_0 = 0$),
- Computation of updated tangent matrix $K_{n,i}^T$ and the restoring load $F_{n,i}^{nr}$,
- Determination of Δu_i from the Eq. (1.52),
- Calculate the Eq. (1.53) for the next approximation and
- Proceed up to the point when convergence is achieved.

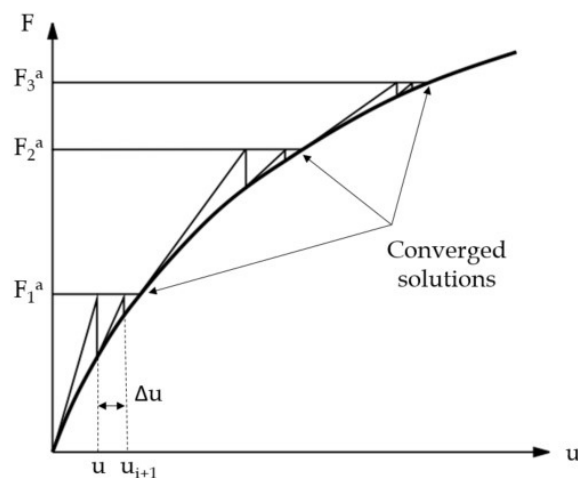


Fig. 1.8. Incremental Newton-Raphson method.

⁵ This process is referred to as the incremental Newton-Raphson procedure.

STABILITY PROBLEMS

Using the full Δu_i in the Eq. (1.53) may lead to solution instabilities in particular situations, e.g. when the load step increment is still too large. Therefore, a line search algorithm will be applied to improve the Newton-Raphson solution and ensure stability. The line search method scales the solution by a scalar value referred to as the line search parameter s . With this Eq. (1.53) is modified and then reads

$$\Delta u_{i+1} = u_i + s \Delta u_i. \quad (1.54)$$

The value of s falls within the range $0.05 \leq s \leq 1.0$ and is determined by minimisation of the energy of the system (Wriggers 2008; ANSYS Documentation).

Further convergence difficulties arise when the structure becomes unstable. In general, an instable response of structures is either related to multiple solutions for a certain load or to the loss of stiffness (e.g. induced by damage). The analysed structures in this thesis are subjected to either large displacement- or force-based loads until they fail. Further numerical stabilization of an unstable problem will be required in force-based computations where the structure becomes unstable due to large displacements resulting from small load increments prior to failure.

This instability problem can be addressed from different perspectives, i.e.:

- computation of a static as a “slow dynamic” analysis,
- applying displacements instead of forces, if possible,
- Riks method⁶ (Riks 1979) and
- a nonlinear stabilization by applying an artificial damping.

Computing a static analysis as a “slow dynamic” analysis allows to use dynamic effects (damping) to prevent the divergence of the Newton-Raphson algorithm. However, this is rather complicated way for solving instability problems. The type of the finite element analysis has to be changed, an appropriate time-integration has to be used and a proper damping factor should be applied.

A displacement-based simulation could not be performed for all structures analysed in this thesis. In particular, a thin-wall component exposed to internal pressure (discussed in Chapter 3) could not be analysed by applying displacement boundary conditions. This is because the displacements in the experiments could be measured accurately only for particular points, but not for the complete geometry. On the other hand, the pressure applied in the experiments is well known and therefore the boundary conditions in the finite element analysis could be accurately represented by applying the pressure in the finite element model as well.

The convergence of the Newton-Raphson method can be expected only within the region highlighted in Fig. 1.9., that is, up to the maximum of the load deflection curve. If there is no a unique solution for every load level, as it is the case for the load level F_4^4 in Fig. 1.9., the Newton-Raphson method cannot reach the solution. This region with critical behavior of the structure has to be known and overcome in the limit load

⁶ ANSYS Documentation refers to this method as the Arc-length method.

calculations. Due to this demand, a more general path-following solution methods were developed (Wriggers 2008).

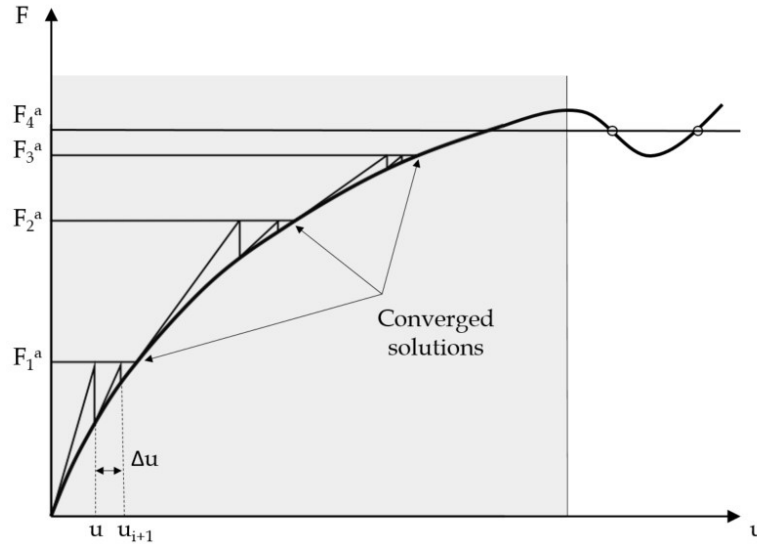


Fig. 1.9. Incremental Newton-Raphson method with highlighted convergence region.

The Riks method (Riks 1979) was developed first and it is a path-following solution method used for overcoming the global instability particularly when the force-based simulation is performed. This method can follow an arbitrary nonlinear solution path. Therefore, it can detect a part of the global force-displacement curve with negative slope, as depicted in Fig. 1.9. Nevertheless, the tracing of the load displacement response as complex as the path shown in Fig. 1.9. (after the highlighted region) will not be required here. Only the load displacement histories where the load level after reaching the maximum drops continuously will be computed.

Eventually, the nonlinear stabilization turned out to be the most efficient method of solving instability problems for specific structural analyses performed in this thesis. An artificial dashpot element is introduced in addition to every element node. In this way, one can add a numerical viscous damping to the nodes. In particular, the stabilization viscous forces F_v of the form

$$\mathbf{F}_v = d_v \mathbf{M} \mathbf{v}_v \quad (1.55)$$

are calculated and added to the global balance equations. In the Eq. (1.55) d_v is the damping factor, \mathbf{M} is an artificial mass matrix computed using unit density and \mathbf{v}_v is the vector of nodal (pseudo) velocity. The nodal velocity \mathbf{v}_v vector is calculated as the ratio of the displacement increment $\Delta \mathbf{u}$ to the time increment Δt ,

$$\mathbf{v}_v = \frac{\Delta \mathbf{u}}{\Delta t}. \quad (1.56)$$

Any affected node having a large displacement increment $\Delta \mathbf{u}$ will cause a large damping force that, in turn, stabilizes⁷ the node by reducing the displacement. As to the nodes that are stable, the stabilization forces are small in relation to the physical forces and therefore these artificial elements have a negligible effect on the results. This can be verified in the numerical model by comparing the stabilization energy to the element's potential energy.

The stabilization i.e. viscous forces \mathbf{F}_v are calculated using the damping factor d_f based on the specified energy dissipation ratio. To circumvent the divergence of the solution, the specified value has to be large enough, yet small enough to prevent an excessive artificial stiffness of the system. At first one should specify the value as small as 1.0e-4 and, if necessary, increase it gradually.

⁷ Stabilization method can be activated in ANSYS using the command "stabilize".

Chapter 2

Coupled damage variable based on fracture locus: Modeling and calibration⁸

A continuum ductile damage and failure model coupled with metal plasticity is presented, with the focus on capturing different failure mechanisms and prediction of the strain localization. The onset of diffuse necking and local thinning is observed in the early stage of experiment and it is caused by the very low strain hardening capability of the material under study. Uniaxial tensile tests have been performed on notched and shear samples, specifically designed to cover different stress states by varying both the notch radius and orientation with respect to the sample axis. The experiments have revealed strain localization caused by material softening. The latter is modelled by a coupled damage accumulation rule whose magnitude is dictated by the actual stress state and strain to fracture. Since the numerical model relies on the fracture strain determined by digital image correlation (DIC), which is dependent on the length scale imposed by the resolution of the DIC grid, an experimentally resolved length scale parameter l is introduced by nonlocal regularization of the material flow, based on large-deformation gradient theory. Apart from its common role of ensuring mesh independency, the length scale parameter obtains a new additional role: it makes the fracture locus calibration procedure robust under changes induced by different spatial averaging of the experimental fracture strain. The measured width of the strain localization equals to the regularization length scale parameter l used in finite element (FE) simulations, thereby ensuring tight correspondence of physical reality and numerical model on the basis of a measurable quantity. As a result, the nonlocal regularization term prevents the strain in the numerical model to localise to a higher extent than experimentally observed. Eventually, the fracture locus has been constructed as a function of stress triaxiality ratio and Lode angle parameter. The FE-modeling

⁸ This chapter has been published in International Journal of Plasticity as an open access article (<https://www.sciencedirect.com/science/article/pii/S0749641919305406>).

methodology is calibrated by force-displacement curves and surface strain profiles prior to failure, obtained by DIC for a subset of sample geometries. The predictive capability of the proposed methodology is demonstrated by computing and comparing FE results to another experimentally characterized sample, not used in calibration procedure, i.e. dog-bone specimen. It undergoes a complicated loading path different from the paths used in the calibration procedure. It has been shown that regularization of strains and metal plasticity model supplemented by a damage variable are indispensable for an overall agreement of experimental and numerical results. The unique numerical model formulation has proven capable of capturing strongly different ductile failure modes, which are experimentally observed and further discussed.

2.1 Introduction and motivation

Although modeling damage evolution and ductile fracture are mature fields of research, many details remain to be tackled for reliable predictions for complex geometries and loading scenarios. One of the challenges that have yet to be solved is the assembly of a unified numerical model capable of predicting the different behaviors of ductile materials under different regimes, i.e. various failure modes. Metal alloys have many real world applications ranging from large lightweight structures, over car bodies to tiny electronic components. In production and over the product life cycle, the material endures complex loading histories and combined tension-compression and shear loadings. Recently, research efforts covering all the full loading complexity have been undertaken (Torki 2019; Scales et al. 2019). The prediction of the material behavior under real loading conditions, not only modeling the behavior of tested samples under laboratory conditions, is still a challenging task, since the loading paths in the experiment and application differ significantly.

2.1.1 Literature overview

The state-of-the-art of ductile damage and failure modeling comprises concepts summarized in Table 2.1 and briefly reviewed below. The term *coupled model* means that all material parameters depend on a damage variable D calculated by means of the respective model in Table 2.1. By contrast, in the *uncoupled model* the damage parameter D is calculated to predict the fracture initiation, but it does not feed back to the elastic-plastic behavior of the material.

Table 2.1. Summary of selected ductile fracture models representing typical modeling approaches

Model and reference	Background	Stress state dependency	Type of approach
Fracture criterion (Freudenthal 1950)	Fracture indicator based on the total plastic work	None	Uncoupled
Rice & Tracey criterion (Rice and Tracey 1969)	Two dimensional fracture locus: equivalent strain to fracture strain as a function of stress triaxiality	Stress triaxiality	Uncoupled
Johnson-Cook criterion (Johnson and Cook 1985)	Fracture strain as a function of strain rate, temperature and stress triaxiality	Stress triaxiality	Uncoupled
Lemaitre continuous damage mechanics (CDM) model (Lemaitre 1985)	Based on continuum damage variable, effective stress concept and thermodynamics	Stress triaxiality	Coupled
Gurson-Tvergaard-Needleman (GTN) (Gurson 1977; Tvergaard and Needleman 1984)	Void nucleation and growth, the void volume fraction is the damage parameter	Stress triaxiality	Coupled
Shear modified Gurson model (Nahshon and Hutchinson 2008)	Added contribution to void damage growth that does not vanish when the mean stress $\sigma_m = 0$	Stress triaxiality, Lode angle	Coupled
Damage fracture model: crack initiation and propagation (Xue 2006; Xue and Wierzbicki 2007)	Damage accumulation induced by the plastic deformation and weakening factor introducing damage-related material softening	Stress triaxiality, Lode angle	Coupled
Bai and Wierzbicki's model with pressure and Lode dependence (Bai 2008; Bai and Wierzbicki 2008)	Three dimensional fracture locus combined with isotropic hardening dependent on hydrostatic pressure and Lode angle	Stress triaxiality, Lode angle	Uncoupled
GISSMO model (Neukamm et al. 2009; Haufe et al. 2010; Basaran et al. 2010)	Damage coupled to the stress tensor according to Lemaitre concept after the limit strain of diffuse necking; fading exponent reduces mesh-size effect	Stress triaxiality, Lode angle	Coupled, regularized

The concept of using uncoupled fracture indicators to predict ductile fracture goes back to 1950s when a criterion based on the total plastic work was proposed by (Freudenthal 1950). Many other different indicators have been proposed since then, on the basis of equivalent plastic strain (Datsko 1966), on the geometry of defects (Rice and Tracey 1969), on the void growth mechanism driven by principal stresses (Cockcroft and Latham 1968), among others. Pioneering works on the subject of the effect of the defects geometry on ductile damage was undertaken by (McClintock 1968a) and (Rice and Tracey 1969). It has been experimentally proven that nucleation and growth of voids accompanying large plastic flow causes a degradation of elasticity and introduces softening effect influenced by stress triaxiality (McClintock 1968a; Rice and Tracey 1969; Hancock and Mackenzie 1976). The material ductility

was characterized by the equivalent plastic strain to fracture ε_f and the stress triaxiality η (Bridgman 1952; McClintock 1968a; Rice and Tracey 1969; Johnson and Cook 1985), usually referred to as two dimensional fracture locus $\varepsilon_f = f(\eta)$.

Coupled modeling concepts come with the advantage of relating damage evolution with mechanical properties. A softening mechanism is present in micromechanical model formulations (Rice and Tracey 1969; Gurson 1977; Tvergaard and Needleman 1984; Nahshon and Hutchinson 2008; Tutyshkin et al. 2014; Brünig et al. 2017; Reddi et al. 2019). They are based on micro void growth, representing the ductile fracture process from a physical point of view. Another coupled approach is based on the widely accepted concept of damage mechanics, where a damage parameter D is included in the material law (Lemaitre and Chaboche 1990; Lemaitre 1985; Lemaitre and Chaboche 1990). Here an effective stress tensor σ is modified by applying $\sigma/(1 - D)$, representing the loss of load carrying cross-sectional area as a consequence of damage. A description of damage accumulation in a phenomenological way has been proposed by (Xue 2006) and (Xue and Wierzbicki 2007), where a power law damage rule is proposed and the weakening factor related to damage describes the material deterioration, with the aim of predicting crack initiation and propagation. However, the lack of experimentally based material parameters and complex numerical implementation often overshadow the advantages of coupled models. Hence applied numerical modeling for practical purposes often reaches again for uncoupled models.

Eventually, after studies showing that besides the stress triaxiality the Lode angle parameter related to the third invariant of the deviatoric stress tensor also has an important effect on ductile fracture (Zhang et al. 2000; Kim et al. 2004; Gao et al. 2010; Barsoum and Faleskog 2011) and experimental evidences (Bao and Wierzbicki 2004; Dunand and Mohr 2010; Bai and Wierzbicki 2008; Zhang et al. 2000), the uncoupled fracture criteria are developed whose heart is a three dimensional (3D) fracture locus $\varepsilon_f = f(\eta, \theta)$, i.e. the surface constructed in stress-strain space, in other words a function that returns the strain to fracture ε_f given the stress triaxiality η , and the Lode angle parameter θ . The concept of the incremental damage accumulation rule (Fischer et al. 1995) is employed to define the onset of fracture and enables to capture strongly nonlinear strain paths. The material strength unaffected by damage and difficulties in detecting the “onset of fracture” from experiment can be listed as main shortcomings of the uncoupled approach. Nevertheless, the simplicity of the numerical implementation, taking into account stress and strain history and calibration of material parameters from experiments have made fracture initiation models widely used, among others (Dunand and Mohr 2010; Khan and Liu 2012; Roth and Mohr 2016; Wang and Qu 2018; Roth and Mohr 2018). The GISSMO model (Generalised Incremental Stress State dependent damage MOdel) couples damage based on a 3D fracture locus to the local stress tensor. It has been developed at Daimler and DYNAmore (Neukamm et al. 2009; Haufe et al. 2010) for the prediction of failure in metal sheets.

Today there is a wide range of constitutive models available for modeling physical mechanisms that precede ductile fracture. (Malcher et al. 2012) assessed the well-established coupled damage constitutive models, Gurson-Tvergaard-Needleman

(GTN) model proposed by (Gurson 1977) and modified by (Tvergaard and Needleman 1984), as well as Lemaitre's damage concept (Lemaitre 1985), together with new model of metal plasticity proposed by (Bai and Wierzbicki 2008). (Malcher et al. 2012) concluded that, under combined loading, all models should be improved and further studied to enhance their prediction reliability. The contribution of (Li et al. 2011) also discussed the performance of an uncoupled ductile fracture indicator and two coupled damage models: the GTN model and Lemaitre's model. The authors closed with the conclusion that there is no concept that performs well both in the high and the low triaxiality regime. More recent reviews of ductile fracture models (Pineau et al. 2016; Benzerga et al. 2016) cover the latest advances of extended micromechanical Gurson models dealing with fracture mechanisms at both high and low triaxiality.

2.1.2 Motivation

The study of the previous references motivated the present contribution and the development of a generally applicable modeling concept under high and low triaxiality and combined loading. A three dimensional fracture locus will be therefore constructed and embedded into a coupled damage mechanics framework, instead of relying on plasticity unaffected by damage. The assumption of damage-free plasticity combined with classical von Mises idealization of the yield surface renders uncoupled fracture locus models incapable of predicting failure by shear band formation and other plastic instabilities in general 3D models. Strain localization, or loss of ellipticity occurs when the acoustic tensor becomes singular (Rudnicki and Rice 1975). For material undergoing associative plastic flow, this condition is not met unless strain softening is taken into account in the constitutive description. This means that for the materials whose plastic flow is strongly affected by ductile damage (nucleation and growth of voids caused by plastic deformation), damage-free plasticity cannot give good predictions for the force-displacement response and strain distribution.

Furthermore, the models based on a 3D fracture locus rely on the measurements of the fracture strain. The strain field is commonly characterized experimentally, e.g. by DIC techniques and computed numerically, e.g. by means of the finite element (FE) method (Beese et al. 2010; Dunand and Mohr 2010) to get access to the loading path, i.e. evolution of the stress triaxiality, Lode angle parameter and the equivalent plastic strain. Although the calibration strategy seems to be well-established, the so-determined strains will depend on a length scale dictated by the resolution of the DIC grid, which will hereinafter be termed *experimentally resolved length scale*. From the strain field just before the final failure (the instant of the material separation), the local maximum of the equivalent plastic strain will be identified and henceforth be termed resolved fracture strain. It is obviously length scale dependent. The dependency of the fracture strain on the experimentally resolved length scale and the importance of its incorporation into numerical models remains understated in the literature. To the best of the authors' knowledge, none of the models in the literature that rely on the fracture strain measurements takes into account the experimentally resolved length

scale in its numerical formulation. In Gurson type as well as Lemaitre damage type models, the failure energy depends on the element size in the FE model. The GISSMO model (Neukamm et al. 2009; Haufe et al. 2010; Basaran et al. 2010) does rely on damage and regularization, where a fading exponent is introduced solely to avoid mesh dependency and is therefore a function of an element size. However, we suggest to introduce the regularization as a function of the length scale over which the experimental strains are averaged in the determination of the fracture strain. The present work focuses on the fact that the gage length for strain measurements must correspond to the width of the localization band. In this way, the measured strain at fracture is the actual average strain occurring in the fracture initiation zone, i.e., the localization band.

The fracture locus is calibrated using finite element (FE) models that allow extracting the evolution of the stress triaxiality and Lode angle parameter as a function of the plastic strain. The simulations are only meaningful if the FE models are mesh independent even across the models for the multiple specimens needed for calibrating the fracture locus. Frequently in the literature the element size is chosen such that it is suitable for the particular specimen type and loading scenario to be modelled, e.g. just in shear specimens smaller element size is used in the zone of the expected shear band, whereas larger elements are used for other calibration specimens, e.g. (Qian et al. 2015)). In our work, we want to avoid having to adjust the mesh size to the individual type of specimen to be modelled. This makes our model mesh insensitive and thus ensures its general applicability to real geometries (even when a non-uniform mesh is required) and real loading scenarios different from the calibration experiments.

Gurson models are identified either using force-displacement data by optimization methods (Springmann and Kuna 2005) and Artificial Neural Networks (ANN) (Marouani and Aguir 2011), or using full-field displacement measurements serving as input for ANN (Abbassi et al. 2013). Similarly, an inverse analysis approach is also employed to identify the parameters of Lemaitre's damage model (Roux and Bouchard 2010; Bouchard et al. 2011). The complexity of the calibration procedure for the proposed model is kept low since the freedom in adjusting the damage model parameters is minimised due to experimentally measurable quantities. DIC strain measurements determine the fracture locus and impose the regularization length parameter to match the localization length scale. Only 1 parameter remains to be optimized from FE simulations to match the force-displacement response, as shown in the sections below.

This work presents a ductile damage model based on the 3D fracture locus, coupled to plasticity, relying on the fracture strain determined by DIC. The main novelty lies in the fact that the experimentally resolved length scale is taken into account by introducing a length scale parameter into the material law. This is done via nonlocal regularization of the material flow based on large-deformation gradient theory (Anand et al. 2012). It is emphasized that in addition to its common role of ensuring mesh independency, the length scale parameter obtains an entirely new, additional role: it makes the fracture locus calibration procedure robust under variation of the

spatial averaging of the experimental strain. The nonlocal regularization term produces an additional hardening contribution only in the region where the strain of the FE model tends to localise to a higher extent than experimentally observed. This solves two issues: the mesh size dependency of the numerical model and the influence of the resolution of the imaging technique on the measured fracture strain.

Modeling progressive material damage and failure is accomplished by supplementing the fracture locus model with:

- a damage variable, D , that accounts for the influence of the current stress state via the corresponding fracture locus in the damage accumulation rule. The damage variable D is a scalar quantity under the assumption of isotropic damage, accumulated by the plastic strain increment $d\varepsilon_p$ weighted over the current value of the function $\varepsilon_f = f(\eta, \theta)$, thus defining the three dimensional fracture locus;
- a non-local variable, e^p , that represents a weighted average of the equivalent plastic strain ε_p over the specified strain distribution function defined by the experimentally resolved length scale parameter l . An additional term in the numerical model based on large deformation gradient theory regularizes the strain fields in the finite element model.

We propose modeling strain softening linked to damage evolution dependent on the current stress state along the strain path. This methodology establishes the relation between the damage and the measurable quantity, i.e. the strain. To constitute such a relationship it is required to use accumulated damage as a failure criterion, as the damage is an internal auxiliary quantity that is not directly measurable.

Towards the goal of developing a numerical model by, instead of changing, complementing the current standards in FE modeling of ductile materials, the existing theories for ductile fracture locus (Lou and Huh 2013), damage mechanics (Lemaitre 1985) and regularization (Anand et al. 2012) are embedded into a unifying approach capable of fulfilling the expectations from a generally applicable damage model, i.e.:

- capturing a broad range of triaxialities and various failure modes dominated by void growth and coalescence under tension and shear,
- applicability for real world applications,
- mesh independence,
- calibration of material parameters from independent experiments covering various stress states,
- a minimum number of fit parameters and
- a physical foundation of the model.

While individual aspects of the damage mechanical phenomena listed above have already been extensively treated in the literature mentioned above, to the authors' knowledge there is no model that combines all concepts in a single unified approach. This will be attempted for the first time in the following sections.

The model performance will be assessed on the investigated aluminum alloy AA1050. Prestraining by the extrusion process renders the material much less ductile (see Fig. 2.4). In prestrained specimens, the onset of necking and strain localization occurs at very low local strains in the critical regions of tested tensile specimens. The material data is, therefore, extracted from post-necking region. The instant of the first detectable localization is not well identifiable. Therefore, we aim to model the progress of localization up to the point just before final failure. The localization stage prior to fracture cannot be reproduced by damage-free plasticity.

2.2 Towards a fully coupled damage plasticity model: governing equations

We begin our presentation with preliminaries of the incremental damage concept, where an increment of the plastic strain contributes to the damage increment weighted by the current value of a memory function f which represents the stress state influence on the damaging process. f is dependent on the stress triaxiality and the Lode angle parameter defined by (2) and (4), respectively. Subsequently, we propose and elucidate the model for progressive material deterioration: a stress state dependent damage variable coupled to metal plasticity. Furthermore, a continuum damage and failure model for a ductile metal is presented. Finally, it is shown how the proposed concept is used for the prediction of both, experimental force-displacement curve and strain field distribution prior to failure. It is emphasized that the mechanical behavior is modelled within a continuum mechanics framework, attempting to retain the minimal number of parameters to be calibrated.

2.2.1 Incremental damage concept

Assuming that damage accumulates somewhere in the continuum prior to failure, a damage indicator D is employed as a field variable to quantify it. Generally speaking, any uncoupled failure criterion based on a simple damage theory can be described by the relation

$$\int_0^{\varepsilon_f} f(\eta, \bar{\theta}) d\varepsilon_p = D, \quad (2.1)$$

with D as a damage parameter and a function $f(\eta, \bar{\theta})$ incorporating the stress state dependency of an underlying damage process. An increment of the equivalent plastic strain contributing to the accumulation of damage D is denoted as $d\varepsilon_p$, whereas ε_f is the fracture strain prior to structural failure. ε_f is given by the evolution path of stress triaxiality η and the Lode angle parameter $\bar{\theta}$ and herein will be defined as a maximum local equivalent plastic strain just before the structural failure. The void growth under hydrostatic tension, in the ductile fracture process, is defined by the stress triaxiality ratio.

$$\eta = \frac{\sigma_m}{\sigma_e} = \frac{I_1}{3\sqrt{3}J_2}, \quad (2.2)$$

where σ_m is the averaged stress i.e. hydrostatic stress, and σ_e is the equivalent von Mises stress. The same can be rewritten using the first invariant I_1 of the stress tensor and second invariant J_2 of the stress deviator. The deviatoric stress tensor controls the void shape change in the ductile fracture process and can be characterised by the Lode angle (Lode 1926; Zhang et al. 2000, 2000):

$$\theta = 1 - \frac{2}{\pi} \arccos\left(\frac{3\sqrt{3}}{2} \frac{J_3}{J_2^{3/2}}\right), \quad (2.3)$$

where J_3 is the third deviatoric invariant ($-\pi/6 \leq \theta \leq \pi/6$). Transformation of the equation (3) to the normalized space defines the normalized Lode angle parameter (Bai and Wierzbicki 2008) that is in the range of $-1 \leq \bar{\theta} \leq 1$ and reads:

$$\bar{\theta} = 1 - \frac{6\theta}{\pi}. \quad (2.4)$$

The normalized Lode angle can be interpreted as a parameter describing how far the material is from a pure shear stress state. $\bar{\theta} = 0$ designates generalized shear, whereas $\bar{\theta} = 1$ represents axisymmetric tension and $\bar{\theta} = -1$ axisymmetric compression.

The integral expression in Eq. (2.1) for ductile damage D has a range of $[0, 1]$. $D = 0$ corresponds to the undamaged state. It is assumed that damage initiates with the onset of plastic material flow. Therefore, an explicit damage initiation criterion is not required. It is emphasized that we are not assuming fracture initiation and softening only in the post-initiation range (like e.g. (Li and Wierzbicki 2010)) because it is not aimed to simulate crack propagation, rather damaging of an uncracked ductile solid. Once $D = 1$ is reached final failure occurs, i.e. the material is separated. The assumption of a stress-state independent critical value of damage holds, since the critical and maximum value of the damage parameter is $D = 1$ for the entire stress-state domain.

The increment of the damage indicator dD has the form of a linear damage accumulation rule:

$$dD = \frac{d\varepsilon_p}{\varepsilon_f(\eta, \bar{\theta})}, \quad (2.5)$$

where an increment of the equivalent plastic strain $d\varepsilon_p$ is weighted by the reciprocal return value of the function $\varepsilon_f(\eta, \bar{\theta})$ describing the locus of all possible loading paths until fracture. The form of the function $\varepsilon_f(\eta, \bar{\theta})$ is nonlinear and describes the dependency of the strain to fracture on the stress-state. The chosen ductile fracture model should be calibrated from a series of uniaxial tension tests on designed notched and shear samples with various notch radii and orientations in relation to the sample axis.

The concept of uncoupled fracture locus is straightforward as long as the loading is proportional. For loading paths with both stress triaxiality and Lode angle parameter held constant, integration of Eq. (2.5) returns

$$D = \frac{\varepsilon_p}{\varepsilon_f(\eta, \bar{\theta})} \quad (2.6)$$

and the shape of the fracture strain function $\varepsilon_f(\eta, \bar{\theta})$ can be determined by mechanical testing of various sample geometries, covering different stress-states and attempting to maintain proportional loading conditions. Experimental determination of the local strains prior to failure accompanied by numerical simulations of tested samples in order to get access to strain histories is the basis for the construction of a fracture locus surface. Once the fracture locus is defined, the damage accumulation rule (Eq. 2.5) can be employed to predict the instant and the location of fracture initiation for non-proportional loading paths and complex geometries.

2.2.2 Coupling a cumulative strain damage to elasticity and plasticity

In the framework of Continuum Damage Mechanics (CDM), the initiation and growth of microvoids and microcracks caused by large plastic deformations in metals is called “ductile plastic damage” (Lemaitre 1985). CDM models of ductile damage are derived on the basis of a continuum damage variable, the effective stress concept and thermodynamics (Lemaitre 1985; Lemaitre and Chaboche 1990; Lemaitre 1996). Associated to the strain equivalence hypothesis, the stress tensor is modified by damage and the effective stress tensor is defined, representing the loss of load carrying cross-sectional area as a consequence of damage. The damage strain energy release rate is associated to the damage variable D .

Ductile plastic damage is usually accompanied by material softening and possibly by strain localization, e.g. localized necking. To model such an event in a computational study, the constitutive law must take into account softening of the material. Instead of using definitions of damage and subsequently material softening using the volume fraction of voids, where the critical void ratio is often considered as a calibration constant, we establish the relation between internal damage with an observable quantity, the strain, because it is directly measurable for any sample geometry (and thus for various stress states developing in the samples) even in the presence of localised necking. Direct stress measurements are not possible and there are no analytical stress corrections due to necking for arbitrary sample geometry.

We reject the conventional simplifying assumption of the uncoupled damage theory described by Eq. (2.1) and state that the damage indicator does affect the plastic material flow in an isotropic manner. The magnitude of accumulated damage depends on the level of plastic deformation required to initiate ductile failure under the current loading path. Therefore, the damage scalar quantity D is calculated as an integral of the plastic strain increments at current stress-state conditions with respect to the defined fracture envelope $\varepsilon_f(\eta, \bar{\theta})$, as described by Eq. (2.2).

Accumulated damage manifests in loss of stiffness and decrease of both the material strength and remaining ductility, i.e. the material’s capacity to consume plastic work until material separation. Following the principles of widely accepted damage mechanics (Lemaitre and Chaboche 1990), a coupling of elasticity and plastic internal variables with the scalar isotropic damage variable is obtained. The yield condition is

$$\phi = \sigma_{eff}^2 - [(1 - D) \sigma_y]^2 \geq 0, \quad (2.7)$$

where σ_y is the yield strength of the undamaged material, whose evolution with plastic strain is described by the function

$$\sigma_y = \sigma_y(\varepsilon_p). \quad (2.8)$$

σ_{eff} is the effective stress of the damaged material, where the decrease of the material strength is described by a weakening factor defined as a linear function of the damage variable,

$$\sigma_{eff} = (1 - D) \sigma_{eq}, \quad (2.9)$$

with the equivalent stress σ_{eq} modified by the ductile plastic damage D . Under the hypothesis of the strain equivalence (Lemaitre 1985), the strain behavior of damaged and undamaged material is represented by the same constitutive equations. Consequently, by replacing D with the definition of damage according to Eq. (2.2), the stress-strain relation of the damaged material can be written as

$$\sigma_{eq} = \left[1 - \int_0^{\varepsilon_f} \frac{d\varepsilon_p}{\varepsilon_f(\eta, \bar{\theta})} \right] \sigma(\varepsilon_p) \quad (2.10)$$

stating that the weakening phenomenon of the material is driven by strain induced damage. The damage increment depends on the strain increment weighted over the fracture strain, which itself is a function of the current stress state. Once the rate of the damaging effect prevails over the effect of the rate of hardening, the material enters the softening regime.

The above statement is depicted in Fig. 2.1. The dashed line represents the undamaged material response described by Eq. (2.8). Three differently colored full lines show the true stress-strain curves of the material undergoing different loading paths. The blue (dotted) line corresponds to the blue (dark) domain of the fracture locus at high stress triaxiality. The strain required to enter the softening regime and finally to reach fracture is low here. On the other hand, the green (dashed) line conforms to the nearly zero stress triaxiality domain of the fracture locus. In the low stress triaxiality region the material may sustain larger deformations, because the level of material ductility is the highest in this regime, as most experiments and models suggest. Under shear deformations with low hydrostatic tension, instead of void growth mechanism, elongation and rotation of voids and their interaction causes ductile failure (Tvergaard 2009, 2012). The cyan (dash-dotted) stress-strain curve represents the domain with intermediate values of stress triaxiality. Therefore, the strain required to enter the softening regime is related to the capability of deforming plastically under a certain loading path before reaching the fracture strain.

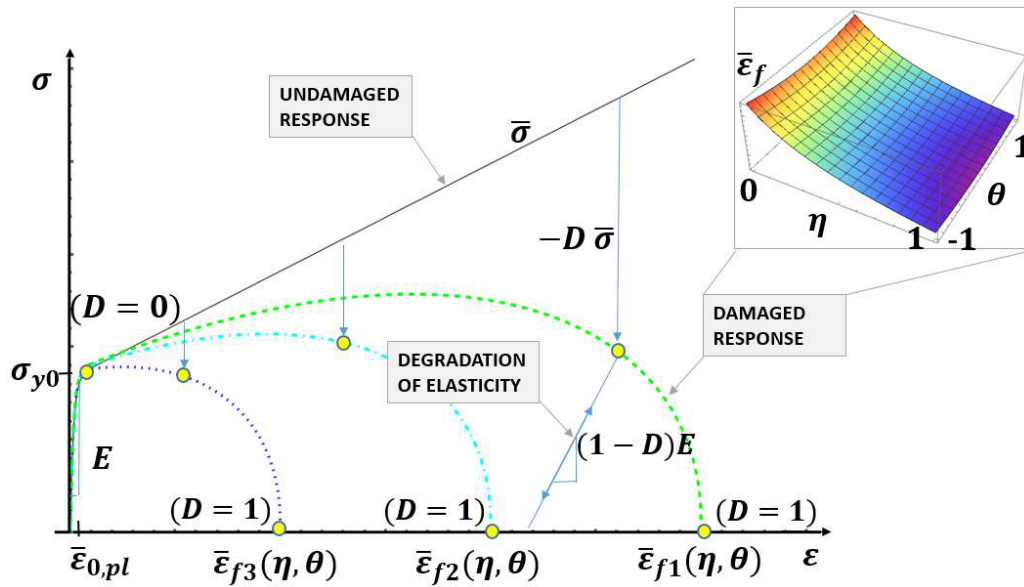


Fig. 2.1. Coupled damage variable for three different loading paths: weakening of the material driven by strain induced damage (schematic representation of Eq. 2.10). The inset shows the fracture locus ϵ_f in the space of stress triaxiality η and Lode angle parameter $\bar{\theta}$.

The amount of strain required to reach fracture depends on the calibrated shape of the fracture locus, the loading path and the corresponding stress states it was running through. For instance, in the regime of low stress triaxialities, for ideal constant loading paths the strain required to reach fracture is higher compared to the strain required in the high triaxiality domain. The influence of damage, represented by $(1 - D)$, is in general a non-linear function of the applied strain, except for the ideal case of a constant strain-history path, i.e. only if there is no change of stress triaxiality and Lode angle parameter during loading. This is possible just in special cases (Bao and Wierzbicki 2004; Brünig et al. 2008; Gao et al. 2010; Driemeier et al. 2010; Dunand and Mohr 2011; Roth and Mohr 2016, 2018).

Isotropic degradation of elasticity is assumed to follow the same rate as the decrease of the material strength,

$$\bar{E} = (1 - D_s) E, \quad (2.11)$$

where E is Young's modulus of undamaged elasticity, and \bar{E} is the effective modulus of damaged elasticity. The damage quantity D_s is referred to as the stiffness damage and it is not necessarily identical to the ductile damage D from the Eq. (2.9). A power law relation $D_s = D^\beta$ is adopted in the work of (Xue and Wierzbicki 2007), with a material constant $\beta \geq 1$. In the present research, following (Xue 2006), stiffness and ductile damage, D_s and D , respectively, are assumed to be equal.

2.2.3 Regularization term

Computation of the material softening induced strain localization (Rice 1976; Rudnicki and Rice 1975; Rice 1976) and shear band formation (Hutchinson and Tvergaard 1981) gives rise to loss of ellipticity and mesh-dependent solutions as discussed from different perspectives (Tvergaard et al. 1981; St. Pietruszczak and Mróz 1981; Belytschko et al. 1986)(Needleman 1988). The dissipated energy decreases as the mesh is refined (Li and Du X. 2010). Furthermore, incremental damage accumulation employs a function $\varepsilon_f = f(\eta, \bar{\theta})$, where the calculated fracture strains correspond to a certain length scale. Whether DIC is utilized to track the plastic flow and the development of localized strain during tensile test, or some other technique, the detected local fracture strain ε_f will depend on the resolved length scale. Therefore, taking into account the influence of the length scale is indispensable. Consequently, a resolved length scale has to be included into the material model not only to regularize the mesh size dependency, but also to justify the use of the fracture strains for model calibration purposes.

To this purpose, we introduce an additional term in our model formulation based on large deformation gradient theory for elastic-plastic materials. Regularization of numerical simulations with strain softening materials has been proposed by (Anand et al. 2012). In addition to the equivalent plastic strain ε_p , the authors have introduced a non-local variable e^p , representing a weighted average of the equivalent plastic strain ε_p :

$$e^p(\mathbf{x}) = \frac{\int_B \psi(\mathbf{y}:\mathbf{x}) \varepsilon_p(\mathbf{y}) dv}{\int_B \psi(\mathbf{y}:\mathbf{x}) dv}. \quad (2.12)$$

The equivalent plastic strain ε_p is averaged and weighted over a Gaussian distribution of the form

$$\psi(\mathbf{y}:\mathbf{x}) = \frac{1}{(2\pi)^{3/2} l^3} \exp\left(-\frac{|\mathbf{y}-\mathbf{x}|^2}{2l^2}\right), \quad (2.13)$$

with the length scale l as a measure of the material volume contributing to the nonlocality of the variable e^p . After mathematical manipulations, the authors (Anand et al. 2012) arrived at the Helmholtz-type partial differential equation for e^p ,

$$e^p - l^2 \Delta e^p = \varepsilon_p \quad (2.14)$$

and an implicit gradient theory is established based on a nonlocal yield criterion. The conventional hardening function $\sigma(\varepsilon_p)$ is modified in an additive manner:

$$\sigma_{eq} = \left[1 - \int_0^{\varepsilon_f} \frac{d\varepsilon_p}{\varepsilon_f(\eta, \bar{\theta})}\right] [\sigma(\varepsilon_p) + L(\varepsilon_p - e^p)], \quad (2.15)$$

becoming then a function of both equivalent plastic strain ε_p and nonlocal plastic strain e^p . The contribution of the additional term $L(\varepsilon_p - e^p)$ is positive in the center of a strain localization where the rate of strain accumulation is the highest and ε_p has the highest value, while it is negative on the edges of the areas of localized strain. This allows to control the width of the strain localization band. The length scale l should

be determined from experimental observations (e.g. the width of a shear band from DIC). It prevents localization of the plastic flow in the numerical simulations. For an adequate amount of gradient regularisation, the value of L should be calibrated using experimental results of tension tests, in a way that both global load-deformation response and local strain distribution are well described.

2.3 Ductile fracture experiments and model calibration

The proposed numerical model requires the following experimental data to be identified:

- plasticity parameters, e.g. yield stress and hardening exponent, describing the undamaged material response,
- fracture locus parameters, defining the shape of the fracture locus and
- regularization parameters, accounting for the resolved length scale.

The foregoing damage plasticity FE model has been implemented in the ANSYS Mechanical environment by means of APDL (ANSYS Parametric Design Language) coding.

The macroscopic mechanical response of the sheet material is characterized by a series of tensile tests. The DIC technique is utilized to track the development of local strains on the sample surface during tensile test, enabling us to observe diffuse necking and shear banding until final rupture occurs. Scanning Electron Microscope (SEM) observations of the sample fracture surface provide an insight into the typical mechanisms causing the fracture of a ductile material – void growth and coalescence dominated by hydrostatic tension and shear failure due to elongation and interaction of voids, as presented below (Fig. 2.11).

2.3.1 Material and experiments

Miniature tensile test samples are extracted from the bottom of the aluminum cans (A1050) by wire electrical discharge machining of a wire diameter of 0.35 mm. The cans are manufactured by an impact extrusion process, with the bottom diameter $d=30$ mm and the bottom thickness $t=0.56$ mm. Three types of sample geometries are specifically designed to cover different stress-states, as shown in Fig. 2.2: notched samples ($R=1.00$ mm, $R=0.25$ mm), shear samples ($\alpha=45^\circ$, $\alpha=0^\circ$) and dog-bone samples (gauge width \times length = 2.00 \times 5.00 mm). Tested tension samples will hereafter be referred according to the list of abbreviations given by Table 2.2.

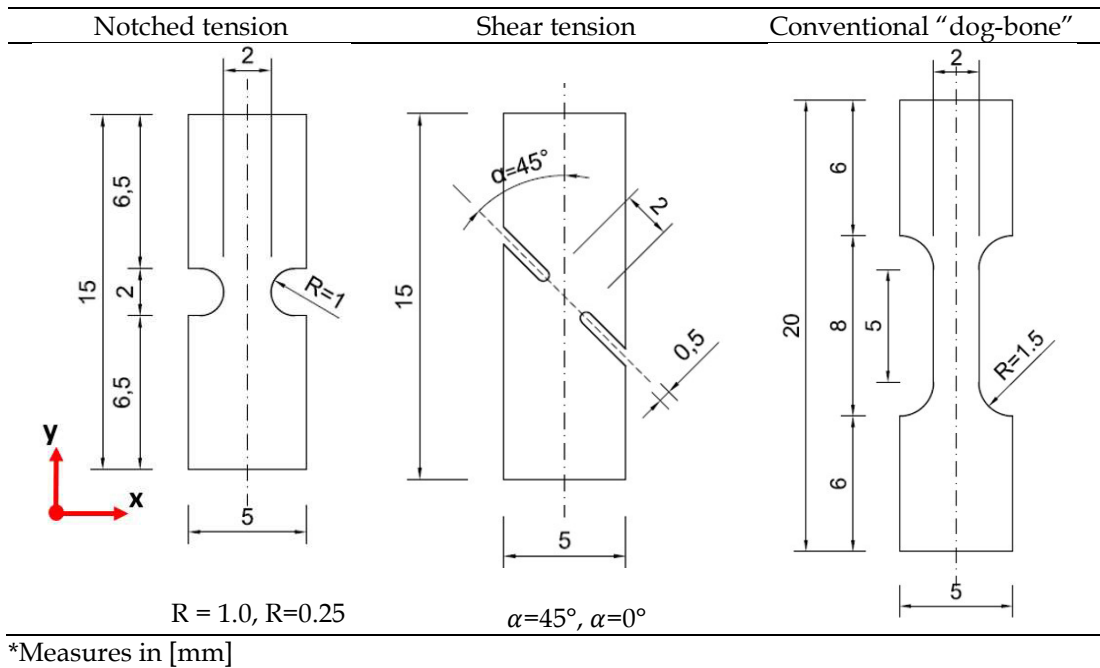


Fig. 2.2. Tension test samples of aluminum alloy AA1050 designed to capture various stress states.

Table 2.2. List of abbreviations

Abbreviation	Explanation
notchR025	Notched tension specimen with radius of the notch R=0.25 mm
notchR1	Notched tension specimen with radius of the notch R=1.00 mm
shear0	Shear tension specimen with angle $\alpha=0^\circ$ (see Fig. 2.2)
shear45	Shear tension specimen with angle $\alpha=45^\circ$ (see Fig. 2.2)
dog-bone	Conventional dog-bone tension specimen
EXP	Experimental result
SIM	Simulation result

Tensile testing is performed by a Bond-tester (Sigma Condor from XYZ-Tec) with a crosshead stroke resolution of 0.03 μm and a sample holder specifically designed for clamping miniature specimens. It is intended to keep the strain rate of the same order at the gauge section level for all tested samples. For this purpose, the tests were conducted using a fixed cross head speed depending on the sample geometry. The dog-bone sample is loaded at 400 $\mu\text{m/s}$ and this is taken as a reference testing velocity. The average strain rate of the specific sample is estimated from a preliminary FEM analysis and a correction factor is applied to the reference testing velocity. The notched samples are then loaded at 10 $\mu\text{m/s}$ and the shear samples at 70 $\mu\text{m/s}$, since the strains in the notched and the shear samples evolve faster compared to the strain in the dog-bone sample. The recorded force displacement curves are summarized in Fig. 2.6.

For the investigation of possible plastic anisotropy of the material, dog-bone samples are cut out in different orientations with respect to the direction of material flow during the extrusion process ($\beta=0^\circ$, $\beta=45^\circ$, $\beta=90^\circ$). Evidently, the anisotropic properties turned out to be insignificant, see Fig. 2.3. To investigate the potential strain rate dependency of the characterized material, tensile tests on additional notched ($R=4.00$ mm) samples and shear (with angle $\alpha=15^\circ$) samples were performed for different strain rates. These tension tests were conducted with varying velocities from 4 to 1000 $\mu\text{m/s}$ for notched and from 15 to 700 $\mu\text{m/s}$ for shear sample, both revealing that the dependency on the strain rate is negligible. Since both the anisotropy and strain rate investigations showed only minor significance, they are not considered any further in this work.

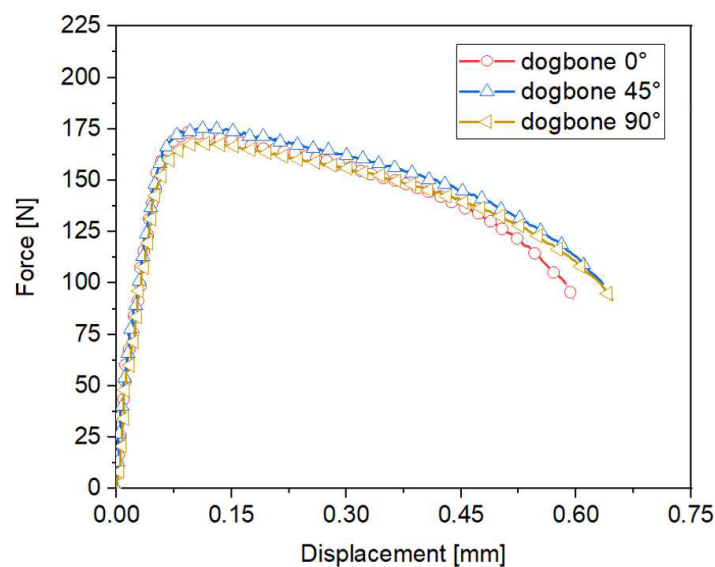


Fig. 2.3. Force-displacement curves of extruded AA1050 in three different orientations with respect to the extrusion flow: 0° , 45° , 90° .

The surface displacement is measured with planar Digital Image Correlation (DIC) using the software VEDDAC7. The natural surface pattern of the sample turned out to provide enough features for a 2D DIC analysis, thus no additional speckle pattern has been applied to the specimen surface. The images are acquired using a digital camera (microDAC@standard, 1624x1234 pixel) at frame rate of 14 pictures/s. The camera is positioned in front of the sample surface, ensuring that the field of view covers the whole sample gage region. DIC measurements of strain accumulation are done gradually with increasing spatial resolution: 10 pixels, 6 pixels, 3 pixels. 1 pixel corresponds to the distance of 0.012 mm between measurement points. Naturally, the smaller the pixel distance between the measurement points, the higher is the computed equivalent strain. The finest possible resolution with 3 pixels between measurement points is considered as relevant for the determination of fracture strains, because it gives the best achievable result with the available experimental setup and software. It is emphasized that these strains are valid for the resolved length scale, which will be taken into account in the numerical model. The distribution of the DIC strain fields on the specimen surface is shown in Fig. 2.5.

To demonstrate the influence of prestraining induced by the manufacturing process, one dog-bone sample is directly cut out from the aluminum can and tested, whereas the second one is subjected to heat treatment after cutting. The used heat treatment profile consists of three sections: (1) a warm-up phase from 25°C to 415°C with a ramp time of 2h, (2) a heat treatment phase at 415°C with a dwell time of 2h, and (3) a post heat treatment phase from 415°C to 250°C with a ramp time of 5h. Tensile testing of both prestrained and annealed samples are performed with a velocity of 400 $\mu\text{m/s}$. Fig. 2.4 shows the structural response of strain-hardened and annealed aluminum: the strain-hardened sample shows higher yield strength and reduced ductility. By contrast, the annealed sample has lower yield strength and can sustain remarkably larger strains, as expected. It is emphasized that the goal of the present research is the characterization and modeling of the strain-hardened aluminum (see Fig. 2.4, red curve).

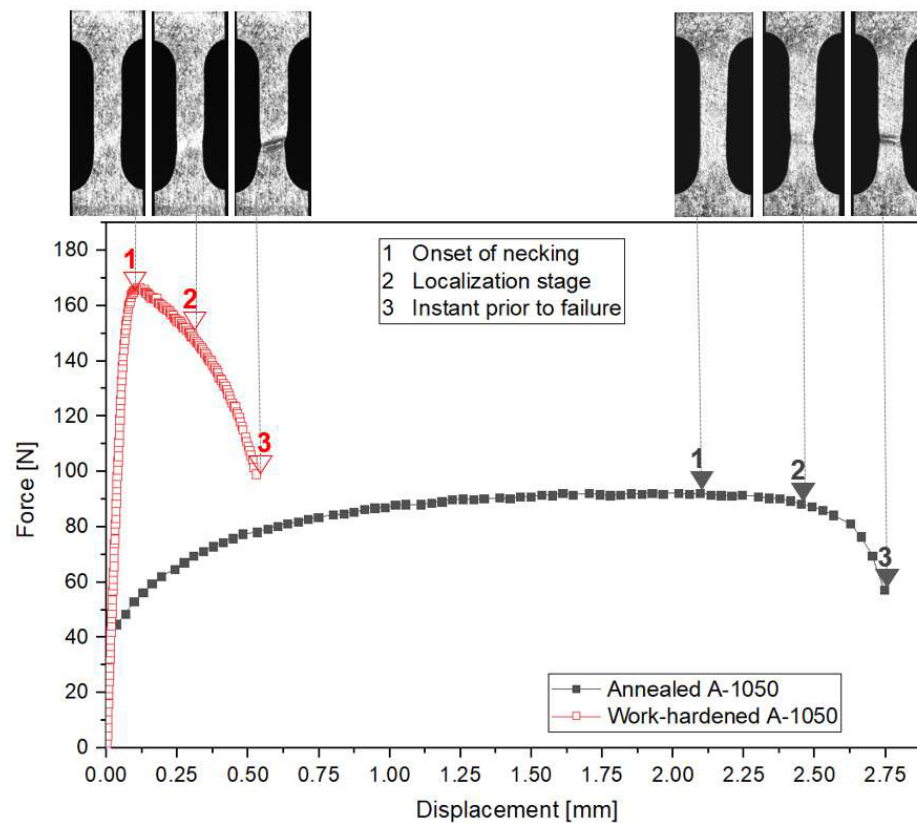


Fig. 2.4. Force-displacement curve of AA1050: annealed and work-hardened dog-bone sample.

Fig. 2.4 also demonstrates the onset of necking at a very early stage for strain-hardened aluminum. This indicates a very low remaining hardening capability of the material. Almost instantaneously after the elastic zone, necking starts in the annealed sample, see label “1” in Fig. 2.4. The identification of the hardening function $\sigma_y(\epsilon_p)$ from uniaxial tension experiments is straightforward as long as the material subject to testing can sustain large strains before necking, i.e. necking is postponed by the material’s hardening capability (Hill 1952; H. W. Swift 1952). It is well known fact that

the standard tensile test only allows to identify the hardening behavior up to the point of necking (Coppeters et al. 2011). However, in the present research, a large hardening region without necking, suitable for identification of the plasticity law, was not observed, making the modeling task more challenging. The experimental evidences show that all sample geometries show the same behavior of necking at extremely low strains because the material is initially strain hardened to a great extent due to the extrusion process. This causes early necking and abrupt strain concentration observed from tensile tests, as demonstrated in the following. Therefore, all material parameters related to damage will be inversely determined from the post-necking behavior of the specimen.

2.3.2 Computational models

The modeling has been performed in two stages. First the *undamaged* mechanical response of tension samples must be considered using a suitable damage-free plasticity model. Then the damage parameters are to be identified through an experimental-numerical analysis of ductile fracture experiments, yielding the physically more meaningful, *damaged* mechanical response of a proposed coupled damage-plasticity law, which combines the theories of (Lemaitre 1985), (Lou and Huh 2013) and (Anand et al. 2012).

2.3.2.1 Plasticity model

Classical J_2 plasticity is used to model the plastic flow of the undamaged material matrix of aluminum AA1050. Von Mises idealization of the yield surface is adopted, because of the material's negligible plastic flow anisotropy, confirmed by mechanical tests in different orientations with respect to extrusion flow. Voce's isotropic hardening law is chosen to model the stress-strain relation of the undamaged material matrix:

$$\sigma(\varepsilon_p) = \sigma_0 + R_0 \varepsilon_p + R_\infty (1 - e^{-b \varepsilon_p}) \quad (2.16)$$

where the parameters σ_0 , R_∞ and b are determined from the pre-necking behavior with uniform strain in uniaxial tension. Due to the reduced hardening capability introduced by prestraining, there are uncertainties regarding to calibration of parameter R_0 , controlling the slope of the hardening curve at the large strains. Based on the hypothesis of a very low remaining hardening potential, a non-hardening model with $R_0 = 0$ is assumed and eventually verified by comparing the experimental and simulated mechanical response of tension specimens at the end of the calibration procedure. Due to this straightforward application of the non-hardening model by setting parameter R_0 to zero, the Voce law was chosen. The remaining Voce parameters $\{\sigma_0, R_\infty, b\}$ determining the initial yield stress, σ_0 , the difference between the saturation and the initial yield stress, R_∞ , and hardening parameter governing the rate of saturation, b , can be determined from the material behavior before necking of the uniaxial tensile specimen.

2.3.2.2 Ductile fracture model

A combined experimental-numerical analysis is carried out in order to determine the form of the fracture locus. Firstly, the experimental strain to fracture $\varepsilon_{f,EXP}$ is determined from tensile tests. Secondly, preliminary FE simulations of all tensile tests are performed, mainly serving the purpose of extracting the loading paths to fracture.

To determine the fracture strain, the onset of fracture must be identified. This can be done based on the first detectable discontinuity in the measured surface displacement field (Dunand and Mohr 2010). However, our experiments did not show such a clear discontinuity and no sudden drop in the load displacement curve was observed. Therefore, we define the fracture strain ε_f as the maximum local equivalent plastic strain just before the instant of the final failure of the specimen, as shown in Fig. 2.5. Before reaching the final failure, no macrocrack is observed.

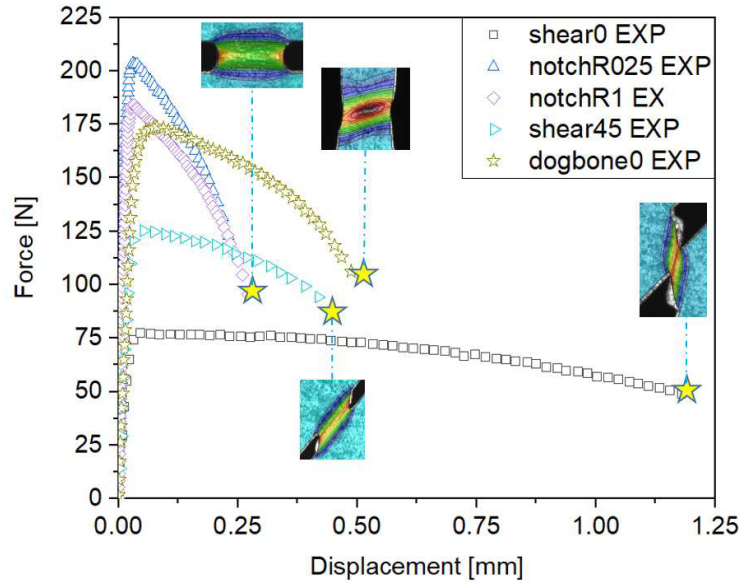


Fig. 2.5. Ductile fracture experiments: force-displacement curves and DIC equivalent strains. The instant prior to failure (★) determines the instant of the onset of fracture

The planar strains ε_{xx} and ε_{yy} are computed by DIC software. Assuming volume conservation, the third strain component in thickness direction ε_{zz} is calculated. Finally, the total equivalent strain to fracture is obtained (shear strain components γ_{yz} and γ_{zx} are neglected):

$$\varepsilon_{f,EXP} = \sqrt{\frac{1}{2} (\varepsilon_{xx}^2 + \varepsilon_{yy}^2 + \varepsilon_{zz}^2) + 3 \gamma_{xy}^2}. \quad (2.17)$$

All experiments are simulated using Voce's plasticity model. Only one-half of each tensile sample is modelled by introducing appropriate symmetry boundary conditions in xy -plane. 8-node solid elements with 0.043 mm element size are used for all finite element models, with 7 elements in thickness direction. In displacement-controlled FE simulations, the measured planar DIC displacements are applied at the

top and the bottom boundaries of the FE model of the sample. Since the coordinates of the DIC measurement points generally do not coincide with the nodal coordinates of the FE model, displacements from DIC are mapped to the FE mesh by linear interpolation (ANSYS Documentation).

Conventionally, it is assumed that the location of the highest equivalent plastic strain coincides with the location of the onset of fracture (Dunand and Mohr 2010). Therefore, the most highly strained integration point is normally chosen for extracting the strain histories, i.e. the evolution of equivalent plastic strain as a function of stress triaxialities and Lode angle parameters. This assumption holds in our particular case of notched-tension samples in the center of the sample gauge region where two critical factors, i.e., the fastest rate of plastic strain accumulation and high triaxiality, appear simultaneously. However, the most critical stress state with regard to ductile fracture initiation is the plane strain tension, which comes from the general form of the ductile fracture locus and its plane strain valley (see Fig. 2.8). Therefore, regarding the shear fracture specimens, fracture might initiate at the free boundaries, not necessarily in the specimen's gauge section. The reason is the particularly rapid increase of the damage indicator due to the increase of stress triaxiality from initially $1/3$ to higher values in the plane strain valley. The stress triaxiality might drift to higher values at the free boundary if the tensile stresses prevail in the respective zone, whereas the specimen's centre remains essentially in the shear stress state with both stress triaxiality and Lode angle parameter ~ 0 . The lower the strain hardening capability, the lower is the risk of reaching a critical state at the free boundary (Roth and Mohr 2018). Nevertheless, even if the fracture does actually initiate at the free boundary, the information gained from the tested sample can still be used by extracting the loading path of that particular material point which first reaches the critical damage $D = 1$. This defines the location of ductile fracture initiation. It will, henceforth, in the work be referred to as the *critical point*.

Eventually, the *critical loading paths*, i.e., the loading path at the critical point, for calibration of the ductile fracture locus are extracted (see Fig. 2.6) not only based on the assumption of the maximum equivalent plastic strain, but also taking into account the stress state evolution. Note that a sharper notch ($R=0.25$ mm) does not induce significantly higher triaxiality and lower fracture strain, compared to a larger notch ($R=1.00$ mm) (see Fig. 2.5). As a matter of fact, the fracture strains of the respective samples are approximately equal. This agrees with the work of (Mirone and Corallo 2010) who found that, at the local scale, the common assumption that a sharp notch leads to high triaxiality and low fracture strain may not always apply; generally it applies in the context of neck-averaged quantities, like the logarithmic strain and true stress. However, from a local viewpoint, if the notch is sharp enough so that the fracture initiates on the outer specimen surface, the local fracture strain may be larger than the current logarithmic fracture strain (Mirone and Corallo 2010).

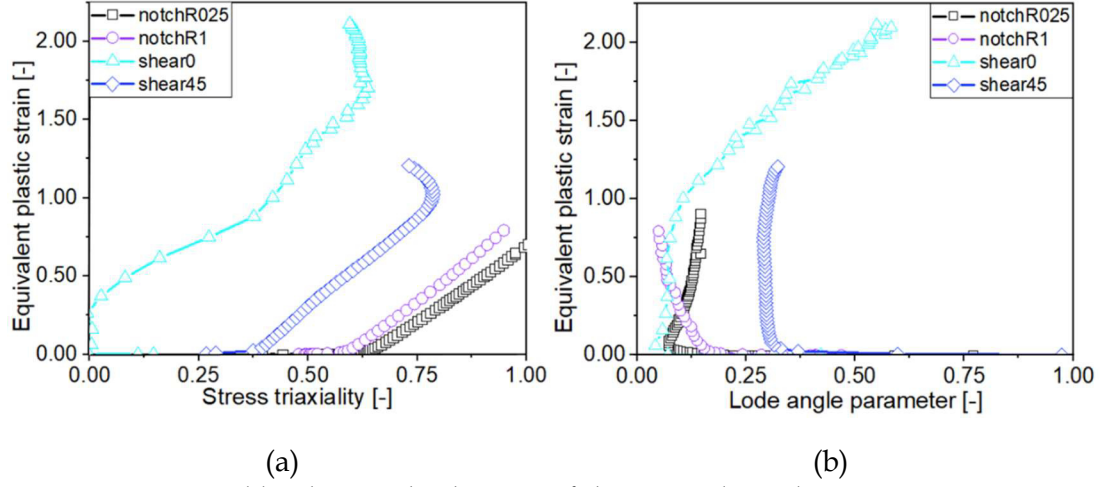


Fig. 2.6. Critical loading paths: history of the equivalent plastic strain vs. stress triaxiality (a) and Lode angle parameter (b) extracted from FEM simulations of ductile fracture experiments at the critical point.

Using the loading paths at the critical material point in tension specimens, the parameters of the ductile fracture model proposed by (Lou and Huh 2013) and modified by (Lou et al. 2014), are determined. The model was first introduced in its original form by (Lou et al. 2012). The choice of the model was guided not only by the ability of describing the dependence of the fracture strain on the current stress state with sufficient accuracy, but also by the objective of keeping the number of material parameters at minimum. (Gänsler H.P. et al. 2001) have shown that as long as damage accumulation is proportional to the accumulated plastic strain and the stress triaxiality ratio, different models give very similar results. Therefore, the mathematical description of the employed ductile fracture model seems to be of minor importance. The model of Lou considers a damage accumulation induced by nucleation, growth and coalescence of voids. The nucleation of voids is assumed to be proportional to the equivalent plastic strain ε_p , the void growth is modelled by a function of the stress triaxiality η , and shear coalescence of voids is described by a function of the Lode parameter $L \cong -\bar{\theta}$. Based on the latter model (Lou and Huh 2013), the fracture locus of a AA1050 aluminum alloy can be described by:

$$\varepsilon_f(\bar{\theta}, \eta) = \frac{c_3}{\left(\frac{2}{\sqrt{\bar{\theta}^2 + 3}}\right)^{c_1} \left(\frac{\langle 1 + 3\eta \rangle}{2}\right)^{c_2}} \quad \langle x \rangle = \begin{cases} x & \text{when } x \geq 0 \\ 0 & \text{when } x < 0 \end{cases} \quad (2.18)$$

where the parameters $\{c_1, c_2, c_3\}$ are to be identified. The material constant c_1 modulates the effect of the normalized maximum shear stress on shear coalescence of voids. The curvature and with it the Lode angle dependency of the constructed fracture locus rise with c_1 (Lou and Huh 2013). The material constant c_2 models the effect of the stress triaxiality on void growth. With increasing c_2 , the influence of the stress triaxiality is magnified on the equivalent plastic strain to fracture (Lou and Huh 2013). The material constant c_3 represents the magnitude of the fracture locus and has no influence on its final shape. Since the critical loading paths are non-linear, an initial guess of the fracture model parameters $\{c_1, c_2, c_3\}$ is estimated based on the measured

DIC strain, the averaged values of stress triaxiality η_{av} as well as Lode angle parameter $\bar{\theta}_{av}$:

$$\eta_{av} = \frac{1}{\varepsilon_f} \int_0^{\varepsilon_f} \eta(\varepsilon_p) d\varepsilon_p \quad (2.19)$$

$$\bar{\theta}_{av} = \frac{1}{\varepsilon_f} \int_0^{\varepsilon_f} \bar{\theta}(\varepsilon_p) d\varepsilon_p \quad (2.20)$$

The final set of fracture model parameters is obtained by evaluating the integral expression for the non-linear loading path (see Eq. 2.2). The parameters $\{c_1, c_2, c_3\}$ are found by means of least-squares optimization of

$$\{(c_1, c_2, c_3)\} = \{(c_1, c_2, c_3) | \sum_{i=1}^{N_s} (D_i(c_1, c_2, c_3) - 1)^2 \rightarrow \min\}, \quad (2.21)$$

with

$$D_i = \int_0^{\varepsilon_f} \frac{d\varepsilon_p}{\varepsilon_f(\eta, \bar{\theta})} = 1 \quad \text{for} \quad \varepsilon_f = \varepsilon_{f,EXP} \quad (2.22)$$

being the damage indicator for each sample geometry i .

N_s denotes the number of tensile samples used for the calibration of the ductile fracture model. The so-determined fracture locus of the extruded aluminum AA1050 is shown in Fig. 2.7.

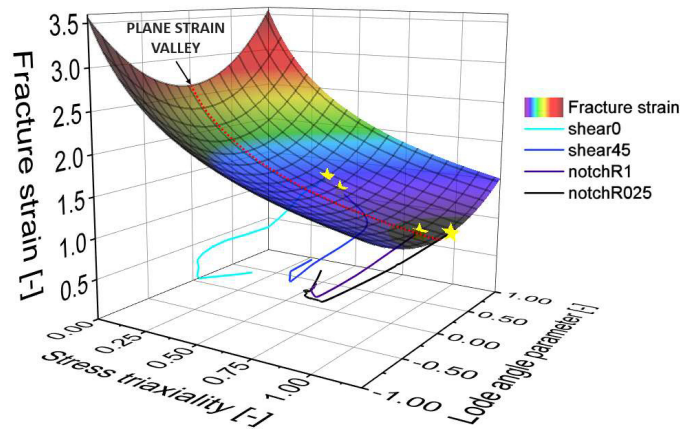


Fig. 2.7. Identified fracture loci of AA1050. Parameters of the ductile fracture model proposed by (Lou and Huh 2013): $c_1=2.082$, $c_2=0.557$, $c_3=2.423$. The figure shows a fracture locus (surface) together with both loading paths (lines) and fracture strains used for calibration (★).

2.3.2.3 Length scale

The smallest identifiable length scale is around one pixel. SEM images of the fracture surface reveal the width of the failure site, i.e. the width of the localised strain band.

In our specific case the estimated width of the failure site area is 0.2 mm, whereas the resolved length scale is 3 pixels = 0.037 mm.

The DIC strain distribution corresponding to the tested sample that exhibits the most extreme localization and, therefore, has the narrowest strain band is chosen for a representative profile to determine the length scale l . The equivalent strain profile $\varepsilon(x)$ is extracted from the planar DIC strains of the shear0 sample along a horizontal line in the center of the specimen, as shown in Fig. 2.8. The strain distribution function $\varepsilon(x)$ may be approximated by a one-dimensional Gaussian function:

$$\varepsilon(x) = \varepsilon_0 \frac{1}{\sqrt{2\pi}l} e^{-\frac{(x-x_0)^2}{2l^2}}. \quad (2.23)$$

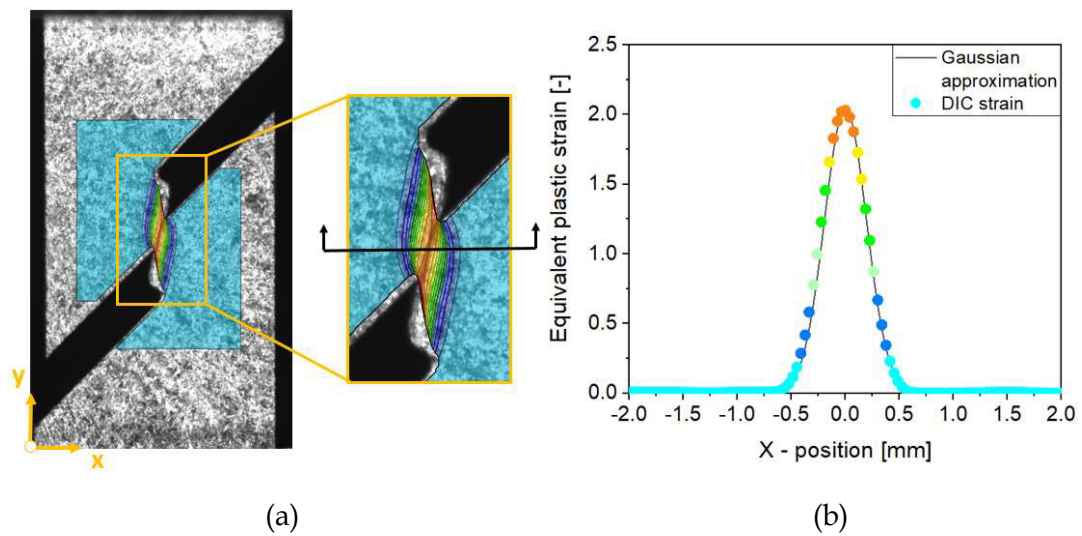


Fig. 2.8. Representative strain profile for determination of experimentally resolved length scale: (a) planar distribution of the equivalent plastic strain determined by Digital Image Correlation and (b) approximation of the central strain profile by Eq. 2.23 with $l=0.195$ mm and $\varepsilon_0=1$.

The parameter l is determined by fitting the one-dimensional function $\varepsilon(x)$ (see Eq. 2.23) to the measurement points of the representative DIC strain profile ($l = 0.195$ mm). The parameter controlling the amount of regularization (see Eq. 2.11), L , has been found iteratively by comparison of the simulated with the experimental force-displacement response of the representative shear0 sample (Fig. 2.9).

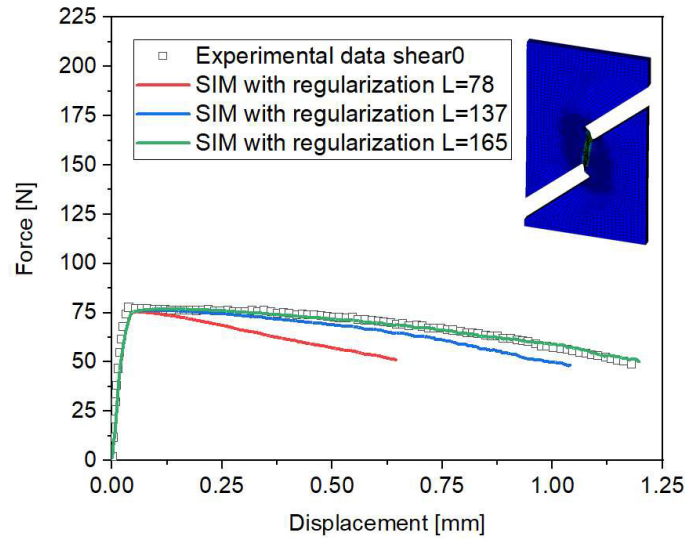


Fig. 2.9. Calibration process of the parameter L controlling the amount of regularization: the iterative fitting procedure by comparing experimental and simulated force-displacement curves. The length scale parameter l is fixed ($l = 0.195$ mm).

2.4 Results and discussion

Table 2.3 summarizes the identified damage-plasticity model parameters for the extruded aluminum alloy AA1050. Finite element simulations of ductile fracture experiments are performed to validate the predictive power of the coupled damage parameter concept also in extreme cases, i.e., ductile fracture at high triaxiality and shear fracture at low triaxiality.

Table 2.3. Material parameters used for modeling aluminum alloy AA1050

Plasticity model	σ_0 [MPa]	R_0 [MPa]	R_∞ [MPa]	b [-]
	120.895	0.000	34.499	851.118
Ductile fracture model	c_1 [-]	c_2 [-]	c_3 [-]	
	2.082	0.557	2.423	
Regularization parameters	l [mm]	L [MPa]		
	0.195	167.125		
Elastic parameters	E [MPa]	ν [-]		
	70 000	0.33		

The numerically obtained global force-displacement curves computed by the coupled damage model are compared with experimentally recorded ones in Fig. 2.10. It can be seen that the overall agreement of the load responses obtained by the coupled damage indicator with experimental data is satisfactory. The material responds markedly different under different regimes and the coupled damage indicator can capture it due to its incremental definition accounting for the stress evolution. In terms of the load response, (Li et al. 2011) have reported a greater discrepancy between the finite element simulation and the experiment when the sample geometry approaches the shear0 type. Here, a good agreement of the force-displacement curves

for the shear0 sample is achieved thanks to the coupled damage model and the implemented regularization method. The contribution of the regularization effect is extremely important in the regime where the tensile test sample exhibits strong localization of the plastic flow. Note that the shear0 sample shows the best agreement because the respective sample was used in the calibration process of the regularization parameter L , see Fig. 9. The identified value of parameter L was purposely adopted and applied for all other samples, with the intention of having a unique parameter set. This, in turn, is the reason why the deviation for the other samples is slightly larger, see Fig. 10. A closer look at the main ductile fracture mechanisms predicted by the coupled damage indicator is further discussed in the following subchapters.

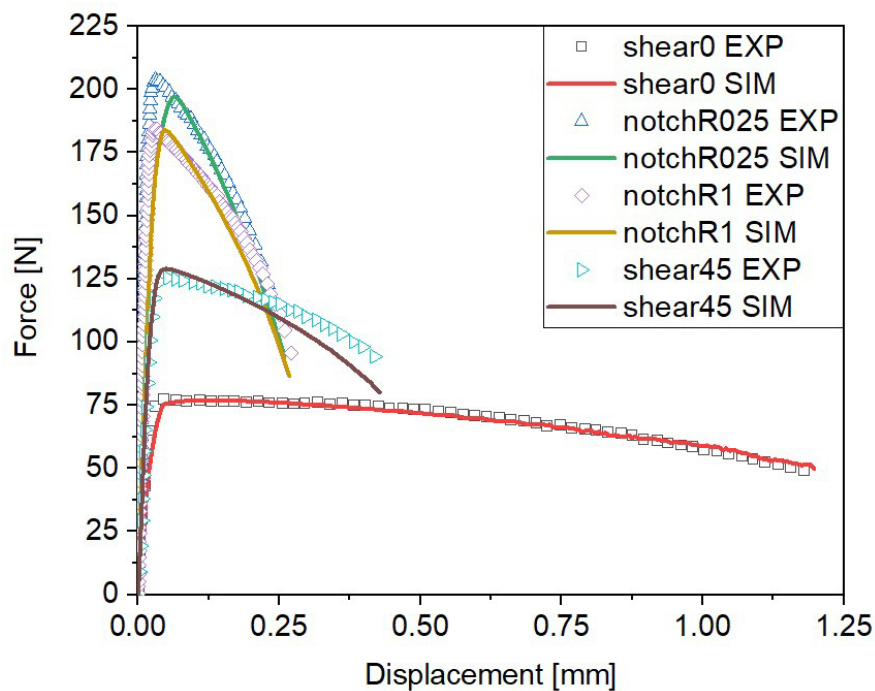
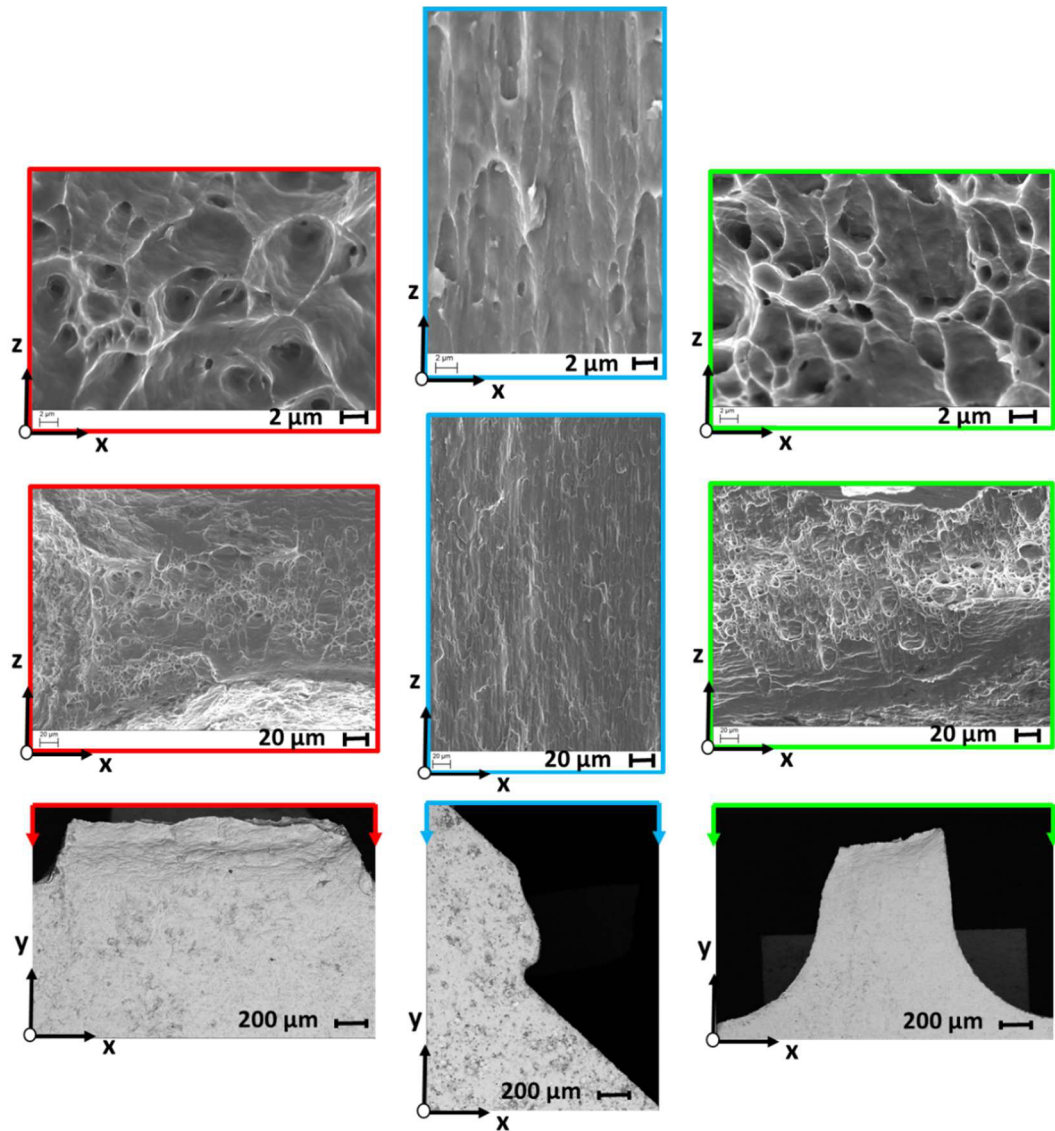


Fig. 2.10. Experimental vs. numerically predicted force-displacement curves of various tests: The FEM simulations use a coupled damage model.

Fig. 2.11 shows SEM micrographs of the fracture surfaces of broken tension specimens and give an insight into the micromechanics of the underlying ductile damage process. The interplay between tensile stress and shear stress determines the dominating fracture mode. This competition between tensile and shear stress can be evaluated by the stress triaxiality value η . Ductile failure due to void growth and coalescence (Fig. 2.11a) occurs at high triaxiality values ($\eta > 0.3$) where positive hydrostatic stress dominantes. Ductile failure due to the elongation of voids and coalescence (Fig. 2.11b) is governed by shear stress and occurs at low triaxiality values ($\eta < 0.3$). The combination of these two modes (Fig. 2.11c) is accompanied by a pronounced shift of the stress state during deformation: the stress triaxiality drifts from initial uniaxial tension ($\eta = 1/3$) to very high values ($\eta > 0.5$). The latter strain path

corresponds to conventional dog-bone specimens where the development of a diffuse neck promotes the increase of triaxiality.



(a) (b) (c)

Fig. 2.11. Scanning Electron Microscope (SEM) micrographs of various ductile fracture mechanisms: (a) ductile failure due to void growth and coalescence observed at the failure site of the notched specimen R025, (b) shear dominant failure and sheared voids at the failure site of the shear specimen 0° , (c) mixed mode failure: combination of ductile and shear failure observed at the failure site of a dog-bone sample.

2.4.1 Shear tension samples

The shear fracture surface of a shear0 sample reveals very little necking of the gage section in thickness direction (see Fig. 2.12a). It is the Poisson effect that causes thinning of the material in the respective zone. However, due to the specific sample

geometry, there exists a zone of zero thickness change. The material's cross-sectional area does not decrease by a greater proportion than the material strain-hardens, thus preventing the prominent necking instability. Therefore, in this sample one can more easily distinguish between the material- and geometry-related effects on the load response. An FE simulation in uncoupled mode is unable to reproduce the force-displacement curves from the experiment (see Fig. 2.12b). Based on the better agreement of the experiment with the numerical result in coupled mode, one can draw the conclusion that the effect of damage plays a significant role when the material undergoes very large deformations. Note that no explicit damage initiation criterion is used in the material model. Fig. 2.13a shows the comparison of experimentally and numerically obtained distributions of the equivalent plastic strain of the shear0 sample surface. Fig. 2.13b shows that the coupled damage indicator successfully predicts the instant of the fracture initiation. Both the equivalent plastic strain and the damage parameter are plotted at the instant of maximum applicable load prior to failure. The location of the fracture initiation, where the damage parameter reaches unity first, tends to be on the free boundary rather than the gauge section. Because a sharp notch appears during loading, the triaxiality increases (Fig. 2.6) close to the free boundary, i.e., structural failure initiates at this location.

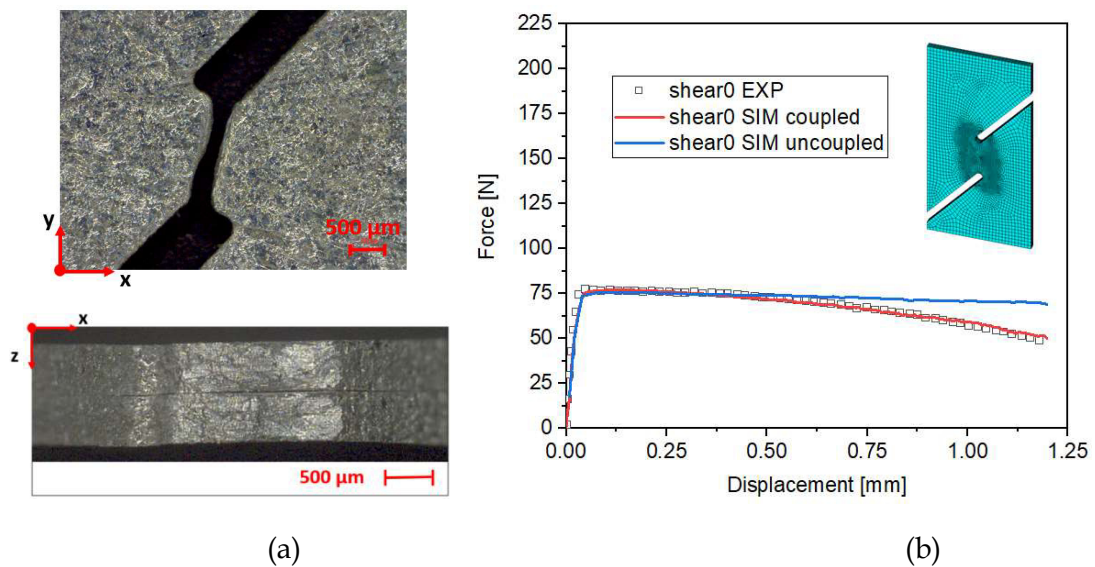
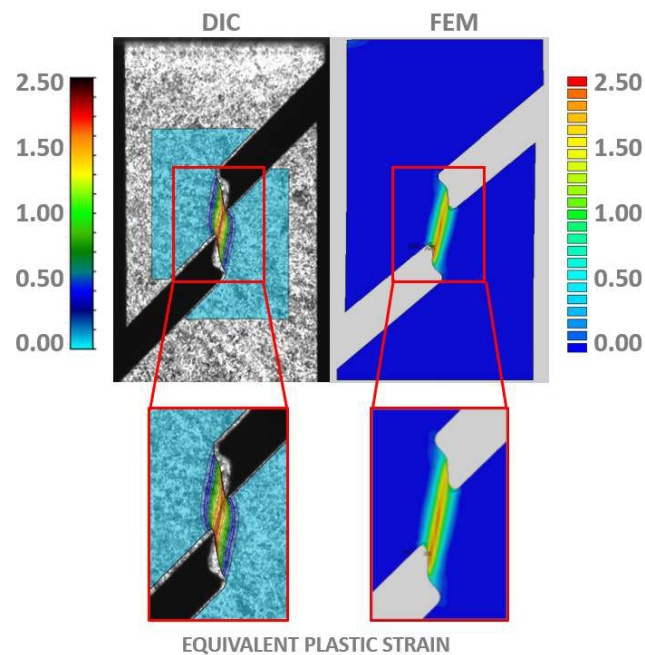


Fig. 2.12. Shear sample: (a) fracture surface and (b) force-displacement curves of coupled and uncoupled damage model compared with experiment, where the inset shows FE mesh.

The surface strain field determined experimentally by Digital Image Correlation (DIC) is compared with the numerical results in Fig. 2.13a. The distribution of the damage parameter displayed in Fig. 2.13b implies that fracture initiates on the free boundary of the gauge section. For the calibration of the fracture locus it is actually desirable to use the fracture strain for the stress state developing at the specimen center, where the stress state varies less in comparison to the free surface.

Nevertheless, calibration of the fracture locus by means of an integration procedure, as shown in chapter 2.3.2.2., allows to capture the nonlinear stress state evolution. In this way, the experimentally determined fracture strain still can be used, although the fracture has not initiated in the specimen center. An increased risk of fracture initiation at the free boundary as compared to the central area is due to higher triaxiality and as a consequence a fast increase of damage. Consequently, the critical location of fracture initiation does not conform with the location of maximum plastic strain. When closely looking at the evolution of mechanical fields in the shear specimen (Fig. 2.6), one concludes that the damage evolution accelerates with increasing triaxiality and slows down with increasing Lode angle. Thus, the increase of the Lode angle parameter partially compensates the effect from the increase of stress triaxiality. This explains the fact that the shear specimen has the largest fracture strain among all investigated specimens. Recent laminographic observations show that voids even form in a material subjected to pure shear loading (Roth et al. 2018), thus supporting the modeling assumptions of the present coupled damage framework.



(a)

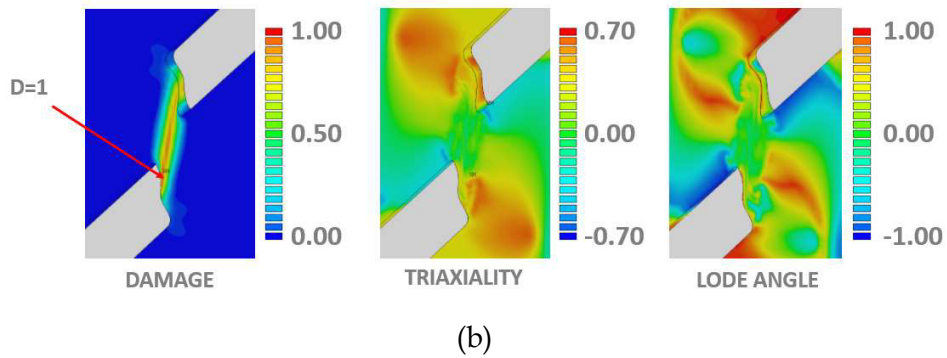


Fig. 2.13. Shear tension sample: (a) Equivalent plastic strain (specimen surface): Digital Image Correlation (DIC) vs. simulated distribution of the equivalent plastic strain and (b) plot of damage with the critical element reaching damage $D=1$ (specimen center), distribution of stress triaxiality and Lode angle parameter.

2.4.2 Notched tension samples

From a macroscopic point of view, a pronounced diffuse necking accompanies the deformation of the notchR1 specimen, as shown in Fig. 2.14a. The rate of necking in the direction perpendicular to the sample surface progresses fast and, therefore, boundary conditions have an important effect on the overall mechanical response in this regime. Micromechanically, the failure mechanism of the notched tension specimen is dominated by void growth (McClintock 1968; Rice and Tracey 1969; Hancock and Mackenzie 1976). Hydrostatic tension, i.e. an extreme increase of the triaxiality is the main driving factor leading to failure. Fig. 2.14b compares numerical predictions of a coupled and an uncoupled model with experimental data. Evidently the geometrical effect, i.e. the decrease of the cross section due to necking, does not sufficiently account for the declining force-displacement curve. In addition, material softening due to damage must be taken into account.

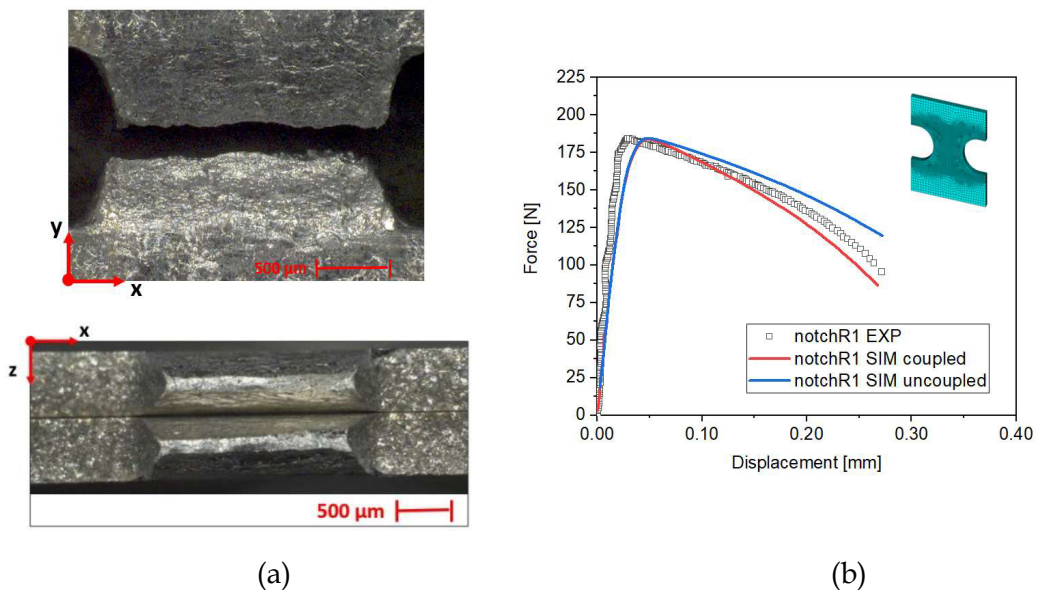


Fig. 2.14. Notched tension sample: (a) fracture surface and (b) force-displacement curves of coupled and uncoupled damage model compared with experiment. The inset shows the FE mesh.

Fig. 2.15a compares experimentally measured, DIC, with numerically computed, FEM, strain fields. The fracture strain of the notched tension sample is much lower ($\epsilon_f = 0.6$) compared to the shear0 sample ($\epsilon_f = 2.5$). Prior to ductile failure, extreme plastic localization occurs. Fig. 2.15b shows that in this case fracture indeed initiates at the location of maximum strain. The highest strain rate develops in the specimen center, where also the stress triaxiality increases rapidly (>0.7) and the Lode angle parameter approaches 0. The shape of the calibrated fracture locus (Fig. 2.7) suggests that the combination of the high triaxiality and Lode angle parameter close to 0 indicates the most critical stress state domain. Plastic strain in the notchR025 sample develops exactly at the location with these critical stress state conditions. Accordingly, the critical location of fracture initiation coincides with the location of maximum plastic strain.

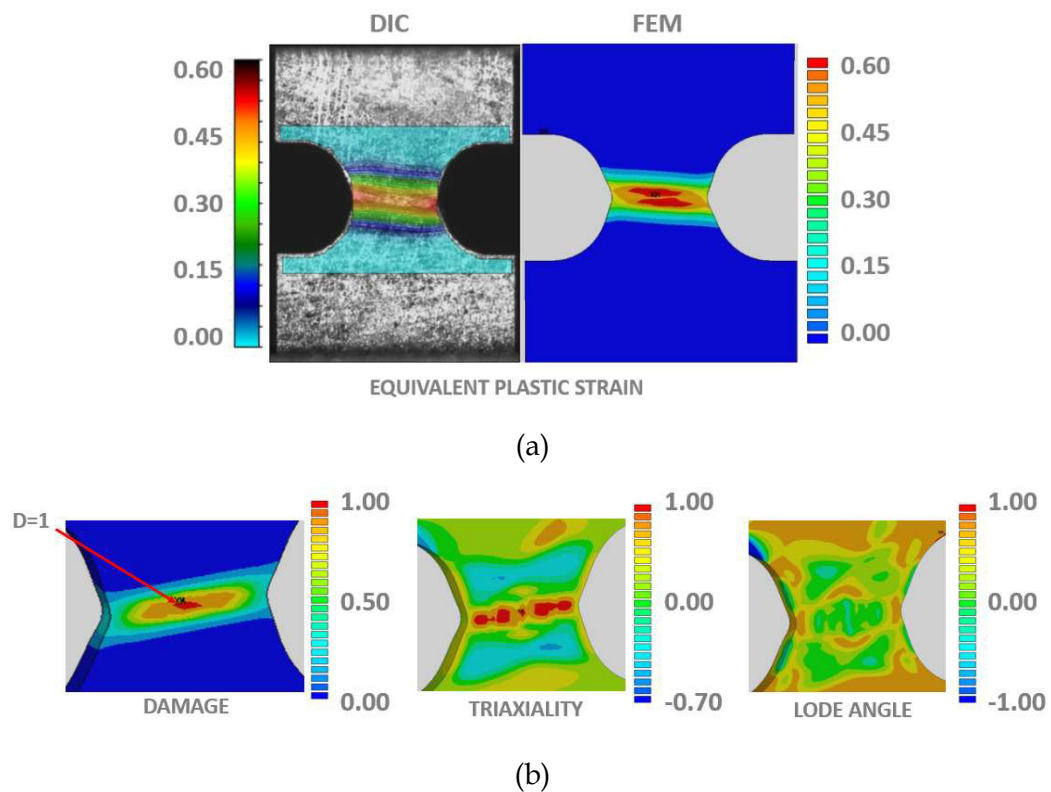


Fig. 2.15. Notched tension sample: (a) Equivalent plastic strain (specimen surface): experimentally measured (DIC) vs. simulated distribution of plastic strain, (b) damage parameter at the critical element reaching damage $D=1$, distribution of stress triaxiality and Lode angle parameter.

2.4.3 Conventional “dog-bone” tension test

It is emphasised that only shear and notched tension tests are used for the calibration of the damage model. The experimental data of conventional dog-bone specimens is excluded from material parameter calibration and serves mainly the purpose of validation of the present model. Thus the predictive capability of the model is demonstrated for a specimen shape and a loading path that has not been used for the calibration procedure (Fig. 2.16).

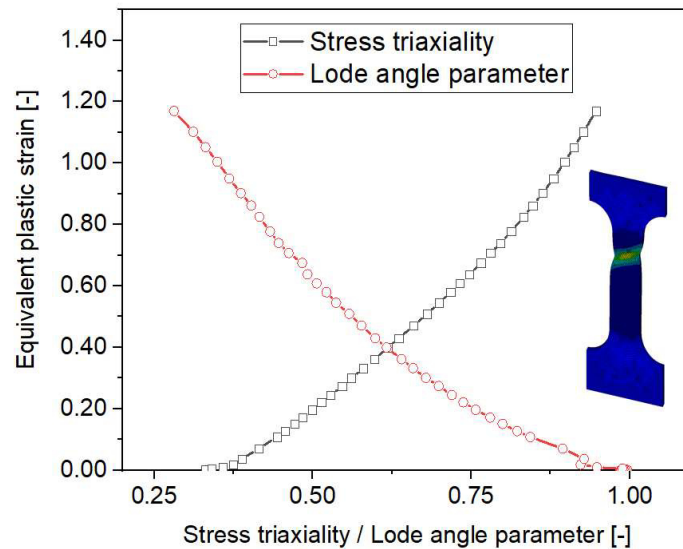


Fig. 2.16. Loading path of the dog-bone tension specimen: history of the equivalent plastic strain as a function of stress triaxiality and Lode angle parameter.

Fig. 2.17a shows two types of instabilities of failure in the dog-bone tension test. Macromechanisms referred to as diffuse and localized necking are bifurcations types preceding the failure of a dog-bone tension test. Fig. 2.17b shows that shear band formation commences soon after initial plastic yielding. The agreement of the simulated force-displacement curve using a coupled model with the experimentally measured curve is generally quite satisfactory, even though the model slightly overpredicts the damage influence at low strains and underpredicts it at high strains. One reason is that the parameters are not re-adjusted to this specific specimen. Instead the set of parameters calibrated from notched and shear tension tests is applied also for the dog-bone specimen. The uncoupled model does not perform equally well, because it can only reproduce the purely geometrical necking effect but does not account for the material softening.

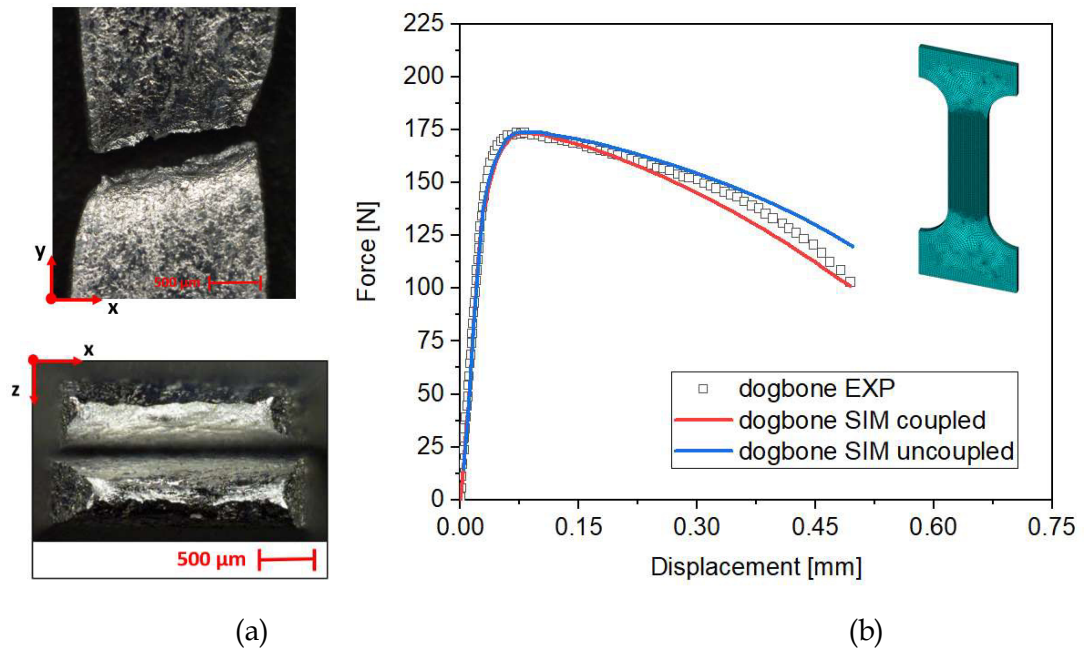
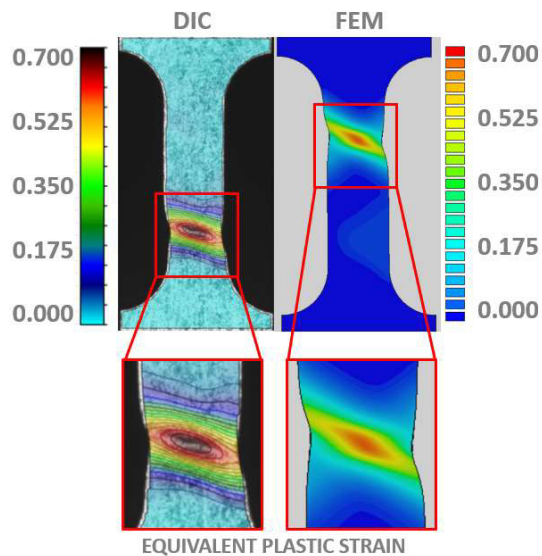


Fig. 2.17. Dog-bone tension test: (a) fracture surface and (b) force-displacement curves of coupled and uncoupled model compared with an experiment.

Fig. 2.18a shows the equivalent plastic strains on the surface of a dog-bone tension test. Both diffuse and localized necking are predicted well by the numerical model. Fig. 2.18b indicates the fracture initiation in the center of a shear band. Both rapid increase of the strain rate and stress state conditions are determining the fracture initiation in the center of plastic localization. Increasing stress triaxiality (>1) and decreasing the Lode angle parameter (close to 0) drift the damage parameter to the most critical plane strain valley.



(a)

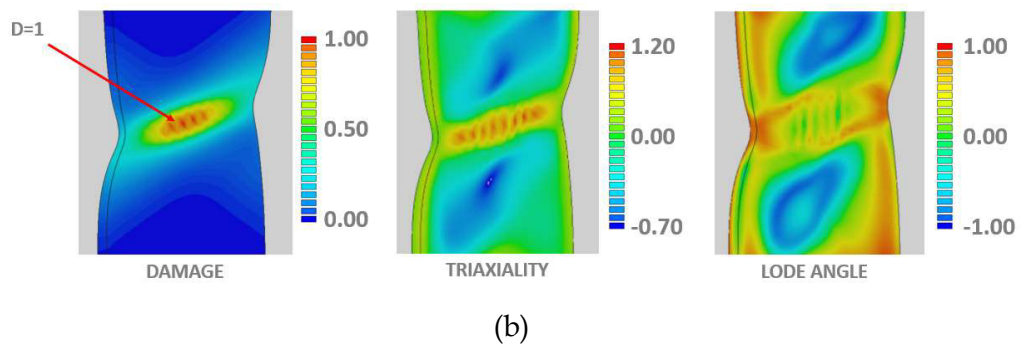


Fig. 2.18. Dog-bone tension test: (a) Equivalent plastic strain (specimen surface): experimental Digital Image Correlation (DIC) vs. simulated using coupled damage model and (b) plot of damage with the critical element reaching damage $D=1$, distribution of stress triaxiality and Lode angle parameter (specimen center).

Mesh independence of the 3D numerical model is achieved with the help of the strain regularization method introduced by (Anand et al. 2012). The numerical results for a coarse mesh and a 3x finer mesh are highlighted in Fig. 2.19. The first column shows the standard equivalent plastic strain ε_p , while the second column represents a “smeared” plastic strain e_p , weighted over a Gaussian approximation function, see Eq. (2.12). The third column depicts the contribution of the regularization term ($\varepsilon_p - e_p$) in the constitutive law. A positive contribution in the center of strain localization and a negative one at the edges are neutralizing the width of the localization band.

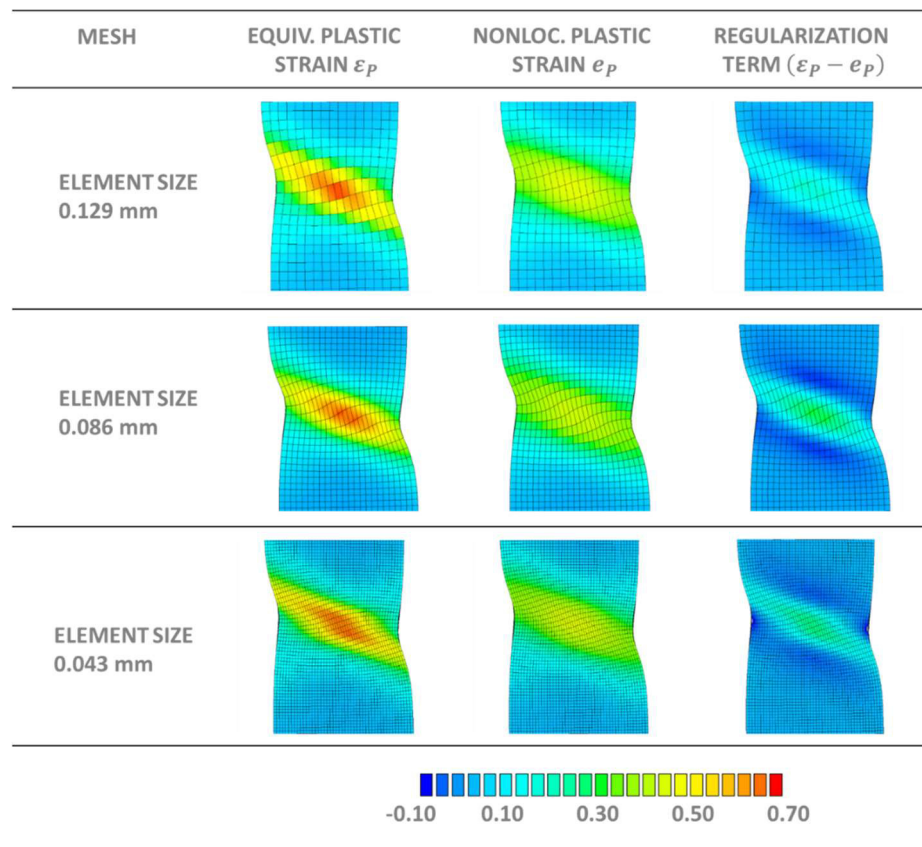


Fig. 2.19. Regularization of shear bands using large-deformation gradient theory proposed by (Anand et al. 2012). Standard equivalent plastic strain ε_p ; nonlocal plastic strain e_p representing a weighted average of ε_p neutralizing the width of the band by the difference of ε_p and e_p having a positive contribution in the center of strain localization and negative one at the edges (specimen surface).

2.5 Conclusions

A damage variable based on the fracture locus has been embedded into coupled metal plasticity. The predictive capability of the coupled and uncoupled damage model has been assessed. The analysis of the numerical results leads to the following conclusions:

1. Despite their obvious shortcomings uncoupled damage models are still in frequent use in the literature. It is thus worthwhile mentioning that uncoupled damage models provide only non-conservative predictions whereas the presented coupled damage model based on the fracture locus concept results in much more reliable predictions of the softened material response, as has been quantified in this work. This supports the conclusions of (Driemeier et al. 2015) who illustrated the need of going back to coupled models, especially when a ductile material undergoes large deformations with significant changes in the microstructure in terms of void evolution.

2. The metal plasticity model coupled with a damage variable based on the fracture locus is capable of capturing various loading paths and ductile failure modes, namely ductile fracture at both high and low triaxialities. This is because the influence of the damage variable on the hardening behavior results in a true stress-strain curve dependent on the history of the stress triaxiality and Lode angle parameter. The importance of the strong stress-state effect on the plastic behavior of isotropic metallic materials has already been elucidated in the literature (Gao et al. 2011).
3. Besides stress triaxiality, the effect of the Lode angle parameter on ductile fracture, although less intuitive, is proven to be equally important as an accelerating factor leading to structural failure. This is due to a drift of the stress state in the direction of the plane strain valley of the fracture surface (fracture locus). Capturing all these stress state effects on the damaging process is possible by the coupled ductile fracture locus model presented in this work using the least number of parameters possible. Specifically, 3 parameters of the fracture locus are fixed from experiments, as well as the length scale l . Only 1 regularization parameter L is to be optimized from simulations. (Driemeier et al. 2015) argue that the material model should perform well using as few parameters as possible, having a physical meaning.
4. The calibration of the ductile fracture mode should account for the non-proportionality of the loading path. It is then able to cover the different material behavior under different regimes by a unique numerical model formulation by coupled damage variable. Finding the final set of the fracture locus parameters by the presented optimization procedure, where damage D is evaluated by integration of every single strain path, for every optimization step, is an advanced method of calibrating the fracture locus. In this way, the non-linear loading paths are taken into account. A simple approximation of strain-averaged triaxiality and Lode angles recognised as inappropriate to define a fracture locus (Basu and Benzerga 2015; Thomas et al. 2016) thus can be avoided.
5. The strain regularization introducing the experimentally resolved fracture strain is indispensable for a good overall agreement of experiment and simulation. The presented model considers the length scale over which the experimental strains are averaged while determining the fracture strain by imaging techniques. In contrast to the former approaches from the literature, the present work focuses on the fact that the gage length for strain measurements must correspond to the width of the localization band. In this way, the measured strain at fracture is the actual average strain occurring in the fracture initiation zone, i.e., the localization band. This measured width of the strain localization equals to the regularisation length scale parameter l used in finite element simulations, thereby ensuring tight correspondence of physical reality and numerical model on the basis of a measurable length.

The presented generally applicable damage model is of high practical use for more reliable failure predictions and design of structural parts made of metal alloys in general (e.g. aerospace, automotive and electronics community) thanks to the more robust model calibration. Changes induced by different spatial averaging of the experimental fracture strain, dependent on the resolution of the applied imaging technique, are possible now to be incorporated in the numerical model via the introduced experimentally resolved length scale. More precisely, the model predicts the fracture initiation (damage $D=1$) in a structure independent of the scale of the experimentally determined fracture strain.

Acknowledgements

The author gratefully acknowledges the financial support under the scope of the COMET program within the K2 Center “Integrated Computational Material, Process and Product Engineering (IC-MPPE)” (Project No 859480). This program is supported by the Austrian Federal Ministries for Climate Action, Environment, Energy, Mobility, Innovation and Technology (BMK) and for Digital and Economic Affairs (BMDW), represented by the Austrian research funding association (FFG), and the federal states of Styria, Upper Austria and Tyrol. TDK Electronics is thanked for providing the material.

Chapter 3

Coupled damage variable based on fracture locus: Prediction of ductile failure in a complex structure⁹

This article focuses on predicting the instant of failure in a real scale component of complex geometry and loading using a ductile damage model calibrated exclusively on small-scale laboratory specimens of relatively simple shape. The ductile behavior of a strain hardened aluminum alloy AA1050, formed into a thin-walled component, is modelled by a coupled ductile fracture locus model presented in a recent study (Baltic et al. 2020a). The component is exposed to high internal pressure and has a safety vent designed for safe pressure handling. The extensive plastic deformation in the safety vent leads to localised ductile failure occurring at a limit load. The pertaining material parameters were calibrated solely from basic ductile fracture experiments in the preceding work (Baltic et al. 2020a), where the bottom section of the thin-walled component was machined into notched and shear samples to characterize different states of stress and to construct a well-defined fracture locus. Although the calibrated material model relies on the local fracture strain measurements, it involves a regularization as a function of the length scale defined as a width of the observed localization band from Digital Image Correlation (DIC) analysis. In the current study the calibration on small-scale specimens is complemented by a large-scale specimen to determine the length scale correction crucial for capturing the correct width of the localization band in the analysed structure. This is necessary because the failure initiation zones of the calibration specimens and the real size structure, i.e. their gauge lengths where the localization band appears, vastly differ in size. Finite element (FE) model results are

⁹ This chapter has been published in International Journal of Solids and Structures as an open access article

(<https://www.sciencedirect.com/science/article/pii/S0020768320304042>).

compared to measurements of the deformation of the aluminum component under pressure and maximum load prior to failure. The numerical and experimental results show an excellent agreement and consistent fracture predictions for various mesh discretizations.

3.1 Introduction and motivation

Ductile damage and failure modeling is essential for a broad spectrum of metallic materials' applications, ranging from large lightweight structures over car bodies to tiny electronic components. Increasing the efficiency of structures, whether in the sense of weight reduction or higher load resistance while maintaining given safety requirements, is a constant demand nowadays. Optimizing structures by numerical means calls for reliable, yet simple-to-use material models to be useable for simulating real world applications.

The reviews of (Pineau et al. 2016; Benzerga et al. 2016; Besson 2009) witness the substantial work and progress made in the field of ductile damage and failure modeling. There are many different aspects of the theory comprising state-of-the-art models, however, all of them have one and the same ultimate goal – a reliable prediction of failure in real structures and thereby a high practical use for design solutions to guarantee the quality and safety of structures. The latest Sandia Fracture Challenge (Kramer et al. 2019) assessed different ductile failure modeling approaches of 21 research teams in an additively manufactured steel structure containing through holes and internal cavities. 12 of them employed local damage as a fracture modeling method and most of them predicted the correct fracture process, though only 2 teams were able to calculate a global force-displacement behavior within the experimental bounds. Despite the encouraging results of sophisticated stress state dependent damage models, the complexity of the calibration procedure often hinders their industrial application, e.g. in the aerospace, automotive and electronics communities. Many details remain to be tackled for reliable predictions of damage in complex geometries and for complex loading scenarios, particularly in the sense of assuring a tight correspondence of material model constants with experimentally measurable quantities, along with using as few parameters as possible. Simulations of engineering structures call for simple model calibration procedures with limited freedom in adjusting material constants.

The literature reports on a large number of methodologies combining experimental and numerical approaches adopting an inverse characterization of the constitutive model, e.g. by using local displacement and strain fields (Kajberg and Lindkvist 2004; Kim et al. 2013), global force-displacement curve (Springmann and Kuna 2005; Tardif and Kyriakides 2012), or force-average axial strain curve (Knysh and Korkolis 2017), among others. However, the material behavior of specimens under laboratory conditions typically differs to a great extent from a component's behavior under real loading scenarios. (Zribi et al. 2013) determined the constitutive parameters of 2 tubular materials from tension tests and tube bulge tests. The authors reported an excellent agreement of the experimental bulge response with numerical results using

material parameters inversely identified from bulge tests. On the other hand, the numerical simulations using parameters obtained from a tensile test showed somewhat smaller deformations i.e. a harder response than measured.

Predictions of ductile fracture location and deformation under given load are also elaborated in the literature. For example, (Qian et al. 2015) predicted the fracture location in ball punch deformation specimens by employing the Johnson-Cook fracture model calibrated from a set of differently shaped tension specimens. (Abbassi et al. 2013) reported a good qualitative correlation between the numerically predicted and the experimentally determined damage location after cracking in an elliptical bulge test. In their study the Gurson-Tveergard-Needleman (GTN) model was calibrated using full-field displacement measurements of a notched specimen serving as input for Artificial Neural Networks (ANN). (Cao et al. 2015) compared six models of three ductile damage approaches for fracture modeling in cold forming processes, namely uncoupled phenomenological models (Bai and Wierzbicki 2008), coupled phenomenological models (Lemaitre 1986; Xue 2006; Cao et al. 2014) and micromechanical models (Tvergaard and Needleman 1984; Xue 2008). The authors reported on accurate results in terms of maximum damage location, whereas only the GTN model showed satisfactory results for the instant of fracture. Local damage models demand an enrichment by regularization methods, using e.g. nonlocal approaches like (Engelen et al. 2003; Anand et al. 2012) or micromorphic approaches (Forest 2009; Aslan et al. 2011). The latter was recently successfully applied to strain localization phenomena in a ductile single crystal (Ling et al. 2018). Nonlocal formulations average certain state variables around every single integration point, thereby spreading the strain evolution in every integration point to the surrounding domain. The size of this domain is to be defined by a characteristic length scale. Introducing nonlocality by gradient-based methods (e.g. (Anand et al. 2012) offers the great advantage of simple implementing a nonlocal variable as a nodal variable in the finite element framework. On the other hand, micromorphic theories make use of derivatives of displacement field and introduce additional degrees of freedom representing the microstructure's deformation and rotation. As additional degrees of freedom are related to classical mechanical variables on a constitutive level, this method is numerically efficient.

This article focuses on the prediction of the instant of fracture in a real scale component of complex geometry under multiaxial loading. The ductile behavior of a strain hardened aluminum alloy AA-1050, extrusion formed into a thin-walled component is modelled by means of a coupled ductile fracture locus model (Baltic et al. 2020a, 2020b). The model belongs to the group of fracture initiation models widely used in applied mechanics (Bao and Wierzbicki 2004; Dunand and Mohr 2010; Khan and Liu 2012; Roth and Mohr 2016; Lou et al. 2017; Deole et al. 2018; Ha et al. 2018; McDonald et al. 2019), though in an uncoupled manner. The component is exposed to high internal pressure and has a rupture point on the bottom section designed for safe pressure handling, termed hereinafter a *safety vent*. The main mechanisms triggering component failure due to rupture of the safety vent are large deformation, diffuse necking, and strain localization in the form of a shear band, along with ductile material damage. The pertaining material parameters were calibrated in the

preceding work (Baltic et al. 2020a) exclusively from ductile fracture experiments conducted on various specimens designed to cover a wide range of stress states. The calibration specimens experienced various loading paths covering the domain of the particular loading path occurring in the real structure. This ensures calibration of the material model independent of the real loading scenario occurring in the aluminum component.

The material's constitutive equations reflect a physically based description of the damage process dependent on the loading path to fracture. The model relies on local fracture strain measurements; however, it involves a regularization as a function of the length scale over which the experimental strains are averaged for determining the fracture strain, termed herein *experimentally resolved length scale*. The mesh independence of the numerical model is thereby ensured, guaranteeing thus correct fracture predictions in complex structures across different and arbitrary mesh discretizations. It is worthwhile mentioning that, apart from eliminating mesh dependency, the length scale makes the fracture locus calibration robust under variation of the spatial averaging of the experimentally measured strain field. More precisely, the changes induced by different spatial averaging of the experimental fracture strain, imposed by the resolution of the applied imaging technique (e.g. Digital Image Correlation, DIC), are incorporated in the model via the regularization term. In the preceding work (Baltic et al. 2020a), we adopted an experimentally resolved length scale equal to the width of the localization band observed by DIC. The gauge length for strain measurements thus corresponds to the width of the localization band and the reported fracture strain is the actual average strain occurring in the fracture initiation zone, i.e the localization band.

In contrast to classical approaches from literature, where an inverse analysis is used to find the model parameters for a specific loading scenario, the present work focuses on predicting the failure scenario in a real-life structure by means of a stress-state dependent damage model established solely from calibration specimens. It is the aim of this work to assure the model predictability for a diversity of design solutions concerning the safe pressure handling in the component. The changes of the key geometric characteristics may induce significant changes of the evolution of the stress-state under loading which must be captured by the model. Moreover, an attempt is made to adapt the experimentally resolved length scale to capture the width of the localization band in the real size component consistently, as its gauge length size where the failure initiates deviates markedly from the gauge length size of the laboratory specimens. To this end, the calibration procedure from original small-scale specimens is complemented by large-scale dogbone specimens, whose dimensions are twice the ones of the small-scale dogbone specimen. The width of the localization band for small- and large-scale specimen is analysed by DIC, hence enabling a simple length scale correction which is numerically confirmed afterwards.

3.2 Computational model: calibration from laboratory specimens

To characterise the material the aluminum thin-walled structure is made of, a geometrically simplified design was used, see Fig. 3.1a. The respective design does not have a safety vent; a detailed geometry of the weakened point that serves explicitly for controlling the maximum tolerable load prior to failure in the actual design is omitted for the sake of extracting the material characterisation specimens. Potential deformation-induced anisotropy of the structure's wall due to the extrusion forming process, as observed for tubular materials (Korkolis and Kyriakides 2008a, 2008b, 2009, 2011a, 2011b; Tardif and Kyriakides 2012; Ha et al. 2018), is not tackled in this study. The focus is entirely on the bottom section of the component, since this is the region of interest where the safety vent is located in the actual design, as it will be shown in the later sections. Therefore, the tension specimens are machined from the bottom part of 0.55 mm thickness. Specimen geometries include dogbone as well as various notched and shear specimens as shown in Fig. 3.1b.

To the reader's convenience the coupled ductile fracture locus model employed in the sequel will briefly be summarized in the following section. For more details about the pertaining ductile fracture experiments the reader is referred to (Baltic et al. 2020a).

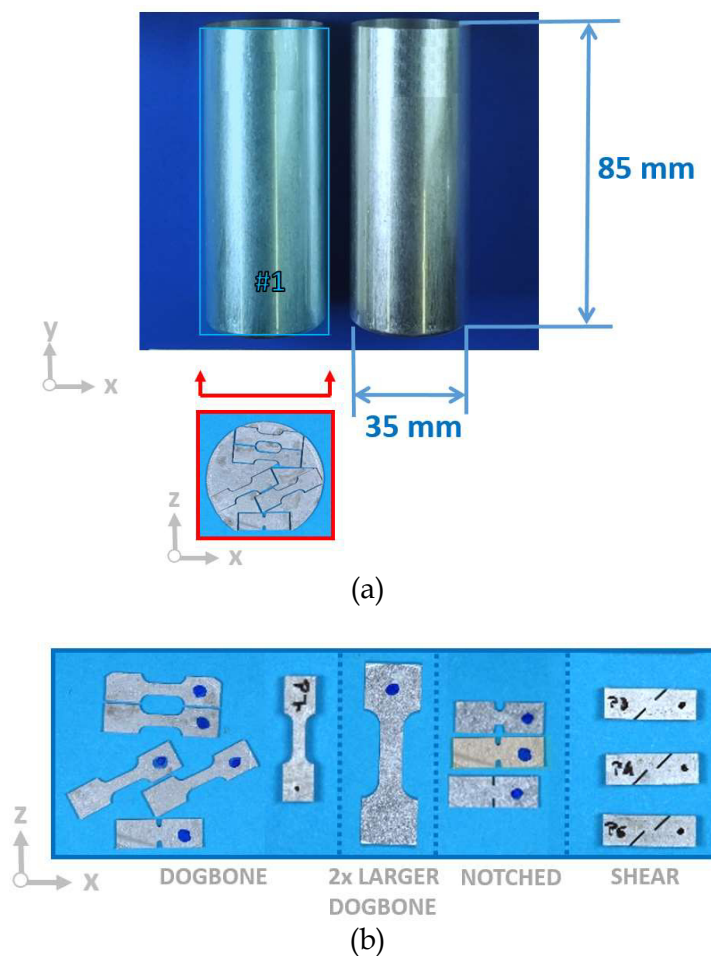


Fig. 3.1. Material characterisation: specimens cut out from a thin-walled aluminum component. (a) geometry of the structural component, (b) specimen geometries

machined from the bottom part of 0.55 mm thickness: dogbone, notched and shear tension specimens.

3.2.1 Coupled ductile fracture locus: governing equations

(Baltic et al. 2020a) embedded the existing theories for ductile fracture locus (Lou and Huh 2013), damage mechanics (Lemaitre 1985) and regularization (Anand et al. 2012) into a unifying approach and proposed to model strain softening linked to damage evolution dependent on the current stress state along the strain path. The equivalent stress of the damaged material is defined as

$$\sigma_{eq} = \left[1 - \int_0^{\varepsilon_f} \frac{d\varepsilon_p}{\varepsilon_f(\eta, \bar{\theta})} \right] [\sigma(\varepsilon_p) + L(\varepsilon_p - e^p)], \quad (3.1)$$

where

- a linear damage accumulation rule, $\int_0^{\varepsilon_f} \frac{d\varepsilon_p}{\varepsilon_f(\eta, \bar{\theta})} = D$, is employed to quantify the ductile damage D assumed to accumulate somewhere in the continuum prior to failure. $d\varepsilon_p$ denotes the differential increment of the equivalent plastic strain ε_p . Once the fracture strain prior to structural failure ε_f is reached, D equals to 1, making it the critical failure limit.
- a three dimensional fracture locus $\varepsilon_f(\eta, \bar{\theta})$ defines a surface constructed in stress-strain space. It is a function that returns the fracture strain ε_f at constant stress triaxiality η and Lode angle parameter $\bar{\theta}$. The stress triaxiality η is defined as a ratio of the hydrostatic stress σ_m to the equivalent von Mises stress σ_e , i.e.

$$\eta = \frac{\sigma_m}{\sigma_e}. \quad (3.2)$$

- For the Lode angle parameter, a definition according to (Bai and Wierzbicki 2008) is adopted who transformed the Lode angle θ (Lode 1926; Zhang et al. 2000, 2000) to the normalized space and defined a Lode angle parameter $\bar{\theta}$,

$$1 \leq \bar{\theta} = 1 - \frac{6\theta}{\pi} \leq 1. \quad (3.3)$$

- a weakening factor defined as a linear function of the damage variable, $[1 - \int_0^{\varepsilon_f} dD]$, affects the plastic flow of the undamaged material, $\sigma(\varepsilon_p)$;
- a regularization term, $L(\varepsilon_p - e^p)$, modifies a conventional hardening function $\sigma(\varepsilon_p)$ in an additive manner and regularizes the strain fields in the finite element model by a non-local variable, e^p . It represents a weighted average of the equivalent plastic strain ε_p over the specified strain distribution function (Eq. 3.7 and Eq. 3.8 below). The parameter L should be calibrated to produce an adequate amount of regularization.

Potential anisotropic plastic flow was investigated by mechanical experiments in three different orientations (0° , 45° , 90°) with respect to the direction of material flow in the course of the extrusion (Fig. 3.2a). It was expected to find a prominent direction

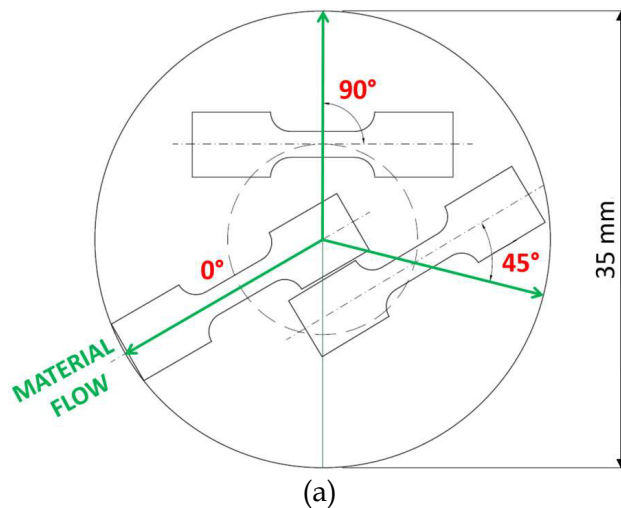
dependency, however, it turned out that anisotropic properties have only a minor significance. The force displacement curves resulting from tensile tests in different orientations evidently show planar isotropy of the material (Fig. 3.2b). Further evaluation of the slope of the plastic width strain (the strain in the specimen width direction) versus plastic thickness strain (the strain in specimen out-of-plane direction) curve is shown in Fig. 3.2c on the example of dogbone 0° specimen under the assumption of volume conservation. This also shows a minor direction dependence, as the Lankford coefficient was found to be 0.95. For Hill's anisotropic quadratic yield function (Hill 1948), the case of isotropic plastic flow is recovered for the Lankford ratios equal to 1. This error of 5% in the initial yield surface was acceptable in the context of the present work, as the main objective is to achieve accurate predictions in the final stage, i.e. at the point of fracture. Therefore, we refrain from considering anisotropic yield functions (discussed in e.g.(Barlat et al. 2005)) any further in this work, unlike e.g. (Kuwabara et al. 2005; Giagmouris et al. 2010; Chen et al. 2018a; Chen et al. 2018b); (Chen et al. 2018b) where the structure's thin wall material is characterized.

Although more general descriptions of matrix yielding (e.g. (Hershey 1954) and (Hosford 1972)) might be more suitable for materials with face centred cubic lattice such as aluminum (Soare 2016), classical von Mises idealization of the yield surface was adopted in the context of the present work. The reason is that for the structural application concerned, an accurate prediction of the final point of fracture is particularly important, as already elucidated above.

Therefore, the plastic flow of the undamaged material matrix is modelled by classical J_2 plasticity. The stress-strain relation of the undamaged material matrix is assumed to follow Voce's isotropic hardening law,

$$\sigma(\varepsilon_p) = \sigma_0 + R_0 \varepsilon_p + R_\infty (1 - e^{-b \varepsilon_p}) \quad (3.4)$$

where the material constants $\{\sigma_0, R_0, R_\infty, b\}$ are to be identified from the material behavior before necking of the uniaxial tensile specimen.



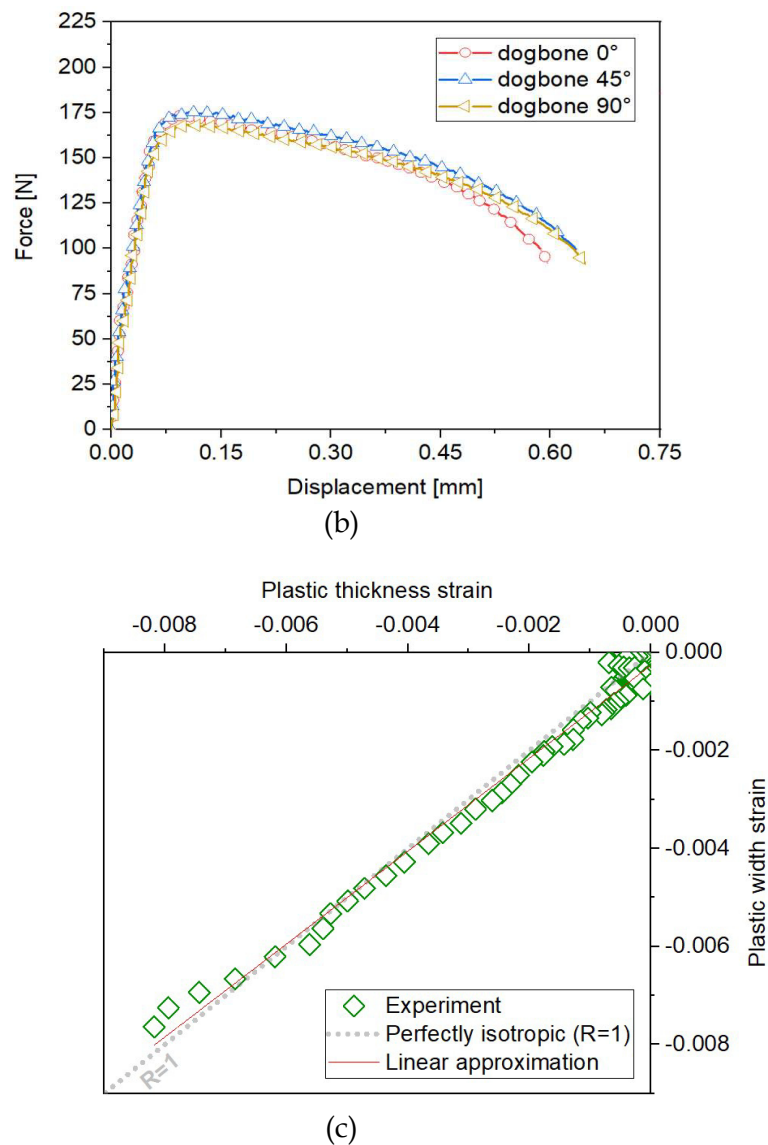


Fig. 3.2. Experimental characterization of flow anisotropy: (a) dogbone specimens machined in different orientations with respect to extrusion flow from the bottom section, (b) force displacement curves of differently oriented dogbone specimens, (c) plastic width strain versus plastic thickness strain curve.

The material enters the softening regime once the rate of the damaging effect is more dominant than the rate of hardening, as depicted in Fig. 3.3. The black solid line shows the plastic flow of the undamaged material, $\sigma(\varepsilon_p)$. Three other lines show the true stress-strain curves of the material undergoing different loading paths. The blue (dotted) line corresponds to the blue (dark) domain of the fracture locus at high stress triaxiality, where the strain required to enter the softening regime and finally to reach fracture is low. The green (dashed) line conforms to the nearly zero stress triaxiality domain of the fracture locus, where the material may sustain larger deformations because the level of material ductility is the highest in this regime, as most experiments and models suggest. Under shear deformations with low hydrostatic

tension, instead of a void growth mechanism elongation and rotation of voids and their interaction causes ductile failure (Tvergaard 2009, 2012). In between these extremes there is the cyan (dash-dotted) stress-strain curve representing the domain with intermediate values of stress triaxiality. The strain required to enter the softening regime is thus related to the capability of deforming plastically under a certain loading path before reaching the fracture strain. Fig. 3.3 also shows isotropic degradation of elasticity, assumed to follow the same rate as the decrease of the material strength,

$$\bar{E} = (1 - D_s) E, \quad (3.5)$$

where E is Young's modulus of undamaged elasticity, and \bar{E} is the effective modulus of damaged elasticity. The damage quantity D_s , representing a decrease of the material stiffness from a macroscopic point of view (Lemaitre 1985), is referred to as the stiffness damage to distinguish it from the definition of ductile damage employed in Eq. (3.1), where damage D is associated with void nucleation, growth and coalescence from the microscopic point of view (McClintock 1968b; Rice and Tracey 1969). In this work, stiffness and ductile damage, D_s and D , are assumed to be equal, likewise in (Xue 2006).

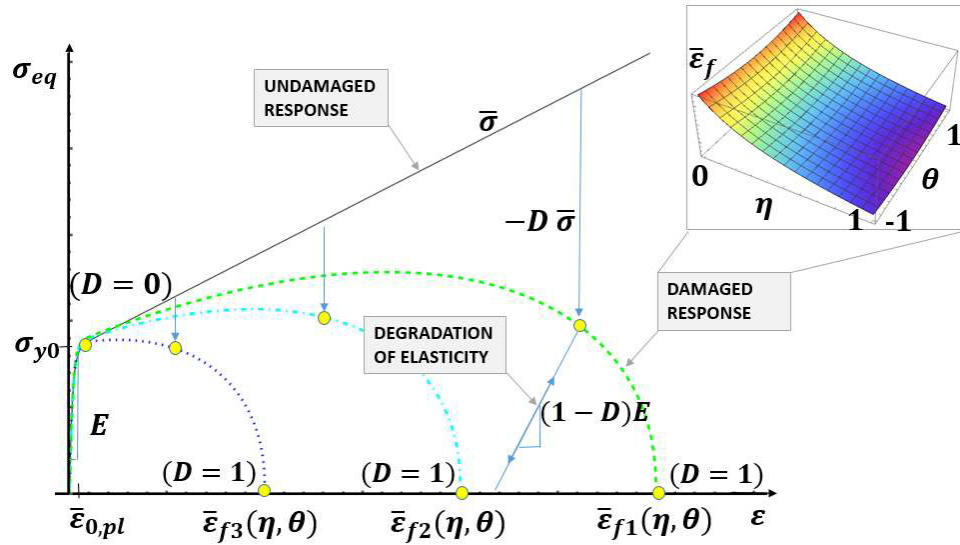


Fig. 3.3. Coupled damage variable for three different loading paths (Baltic et al. 2020a): weakening of the material driven by strain induced damage (schematic representation of Eq. 3.1). The inset shows the fracture locus ε_f in the space of stress triaxiality η and Lode angle parameter $\bar{\theta}$.

The underlying linear damage accumulation rule hypothesis is a simple form of mapping all possible fracture surfaces obtained from different strain paths onto a single fracture locus given by (Lou and Huh 2013),

$$\varepsilon_f(\bar{\theta}, \eta) = \frac{c_3}{\left(\frac{2}{\sqrt{\bar{\theta}^2 + 3}}\right)^{c_1} \left(\frac{\langle 1 + 3\eta \rangle}{2}\right)^{c_2}} \quad \langle x \rangle = \begin{cases} x & \text{when } x \geq 0 \\ 0 & \text{when } x < 0 \end{cases} \quad (3.6)$$

where the material constants $\{c_1, c_2, c_3\}$ are to be found. c_1 and c_2 modulate the stress state dependency of underlying damage process, whereas c_3 represents the magnitude of the fracture locus and has no influence on its final shape. The fracture strain, ε_f , is herein defined as a maximum local equivalent plastic strain just before structural failure.

The additional regularization term, $L(\varepsilon_p - e^p)$, based on large deformation gradient theory for elastic-plastic materials (Anand et al. 2012), is introduced to ensure mesh independency and robustness of the model calibration. When Digital Image Correlation (DIC) is utilized to track the plastic flow and the development of localized strain during tensile test, the so-determined local fracture strain will depend on a length scale dictated by the resolution of the DIC grid, in the introduction already referred to as *experimentally resolved length scale*. The regularization of numerical simulations of strain softening materials proposed by (Anand et al. 2012) is achieved by introducing a non-local variable e^p , representing a weighted average of the equivalent plastic strain ε_p :

$$e^p(\mathbf{x}) = \frac{\int_B \psi(\mathbf{y}:\mathbf{x}) \varepsilon_p(\mathbf{y}) dv}{\int_B \psi(\mathbf{y}:\mathbf{x}) dv}. \quad (3.7)$$

The equivalent plastic strain ε_p is averaged and weighted over a Gaussian distribution of the form

$$\psi(\mathbf{y}:\mathbf{x}) = \frac{1}{(2\pi)^{3/2} l^3} \exp\left(-\frac{|\mathbf{y}-\mathbf{x}|^2}{2 l^2}\right), \quad (3.8)$$

with the length scale parameter l as a measure of the material volume contributing to the nonlocality of the variable e^p . After mathematical manipulations, the authors (Anand et al. 2012) arrived at the Helmholtz-type partial differential equation for e^p ,

$$e^p - l^2 \Delta e^p = \varepsilon_p \quad (3.9)$$

and an implicit gradient theory is established based on a nonlocal yield criterion. The conventional hardening function $\sigma(\varepsilon_p)$ is modified in an additive manner, as shown above in Eq. (3.1). The contribution of the additional term $L(\varepsilon_p - e^p)$ is positive in the center of a strain localization where the rate of strain accumulation is the highest and ε_p has the highest value, while it is negative on the edges of the areas of localized strain. This allows to control the width of the strain localization band in the numerical model.

The set of basic ductile fracture experiments conducted on the designed tension specimens (Fig. 3.1) allowed to identify the following model parameters (as shown in Table 3.1):

- plasticity parameters of Voce's isotropic hardening law given by Eq. (3.4),
- ductile fracture locus parameters of the model proposed by (Lou and Huh 2013), determining the surface $\varepsilon_f = f(\eta, \bar{\theta})$ given by Eq. (3.6) and

- regularization parameter L (Eq. 3.1) of the method proposed by (Anand et al. 2012) and length scale parameter l accounting for the experimentally resolved length scale (Eq. 3.8).

For details about the calibration procedure the reader is referred to (Baltic et al. 2020a). For completeness, the experimentally and numerically obtained global force-displacement curves of the calibration specimens computed by the calibrated set of parameters (Table 3.1) are provided in Fig. 3.4. Note that at the point of structural failure the overall force is nonzero, as there is still some remaining load carrying area while other elements have already reached the damage value of 1 and therefore lost their load carrying capacity. This is in accordance with the experiments, as the tensile specimen fails suddenly without time-resolvable crack propagation because the amount of elastically stored energy is sufficient to induce an unstable crack growth as soon as the crack is initialized.

Table 3.1. Material parameters used for modeling the aluminum alloy AA1050 (Baltic et al. 2020a)

Plasticity model	σ_0 [MPa]	R_0 [MPa]	R_∞ [MPa]	b [-]
	120.895	0.000	34.499	851.118
Ductile fracture model	c_1 [-]	c_2 [-]	c_3 [-]	
	2.082	0.557	2.423	
Regularization parameters	l [mm]	L [MPa]		
	0.195	167.125		
Elastic parameters	E [MPa]	ν [-]		
	70 000	0.33		

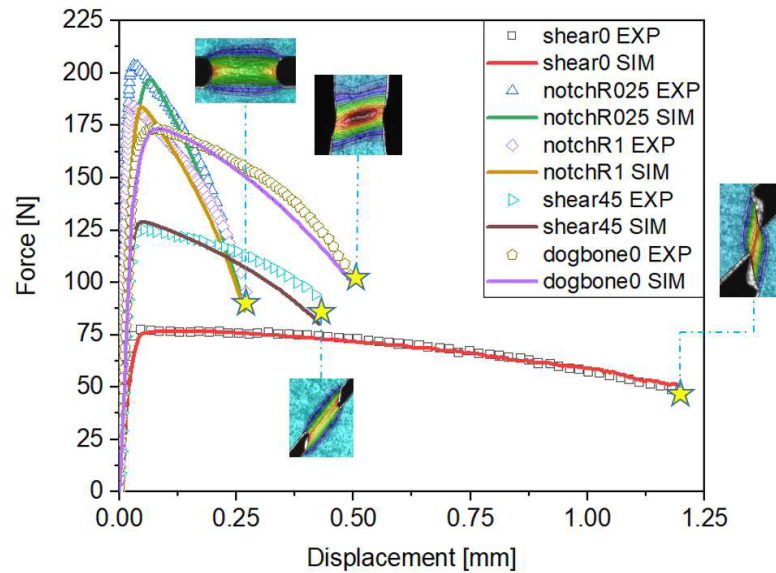


Fig. 3.4. Experimental vs. numerically predicted force-displacement curves of basic ductile fracture experiments and DIC equivalent strains (Baltic et al. 2020a): tensile tests of specimens undergoing various stress states. The star (★) marks the instant prior to failure.

The so-composed numerical model is the basis for the prediction of ductile failure in a complex structure. Before doing so, the length scale correction of the employed regularization method must be addressed to ensure a proper prediction at length scales different from that of the laboratory specimens. Therefore, the calibration on the small-scale tests is completed by a calibration on an additional large-scale experiment as described in the following sections.

3.2.2 Length-scale correction via large-scale model

The numerical model relies on the fracture strain measurements done by Digital Image Correlation (DIC) analysis. The implemented regularization method distributes the strains of the finite element model over a width defined by the length scale parameter, l . This width is purposely set equal to the width of the localization band as resolved by the DIC analysis, $l = 0.195$ mm, so that the gauge length for the local fracture strain measurements corresponds to the width of the localization band observed by DIC.

The so-determined length scale parameter l is calibrated for the localization band observed by DIC analysis in small-scale tests of miniature tension specimens (Fig. 3.1). Additionally, a large-scale specimen, i.e., a two times larger dogbone compared to the miniature dogbone specimen, is tested to determine the length-scale correction necessary for the re-scaled model. On the basis of geometrical similarity in the plane of shearing, we presume that the ratio of the length scale l to the corresponding gauge width w is proportional to the ratio of the scaled length scale l_s to the corresponding scaled gauge width w_s :

$$\frac{l}{w} = \frac{l_s}{w_s} \quad (3.10)$$

The miniature dogbone specimen has a gauge width of $w = 2$ mm, whereas the gauge width of the larger dogbone is $w_s = 4$ mm. The unknown length scale l_s to be applied in the re-scaled model is then determined by Eq. (3.10). To verify the above hypothesis (Eq. 3.10), the finite element predictions are validated by tests on dogbone specimens of different sizes. The fracture strains of both specimens are determined by a DIC analysis conducted with the same resolution of the DIC grid, i.e., 3 pixels (0.037 mm).

Fig. 3.5 shows the comparison of the experimental and numerically predicted force-displacement responses of a miniature dogbone specimen and a twice larger dogbone specimen. The insets show the DIC strains compared to the finite element model strain distributions. A very good agreement of experimental and predicted data is observed, thus supporting the adopted simple length-scale correction given by Eq. (3.10).

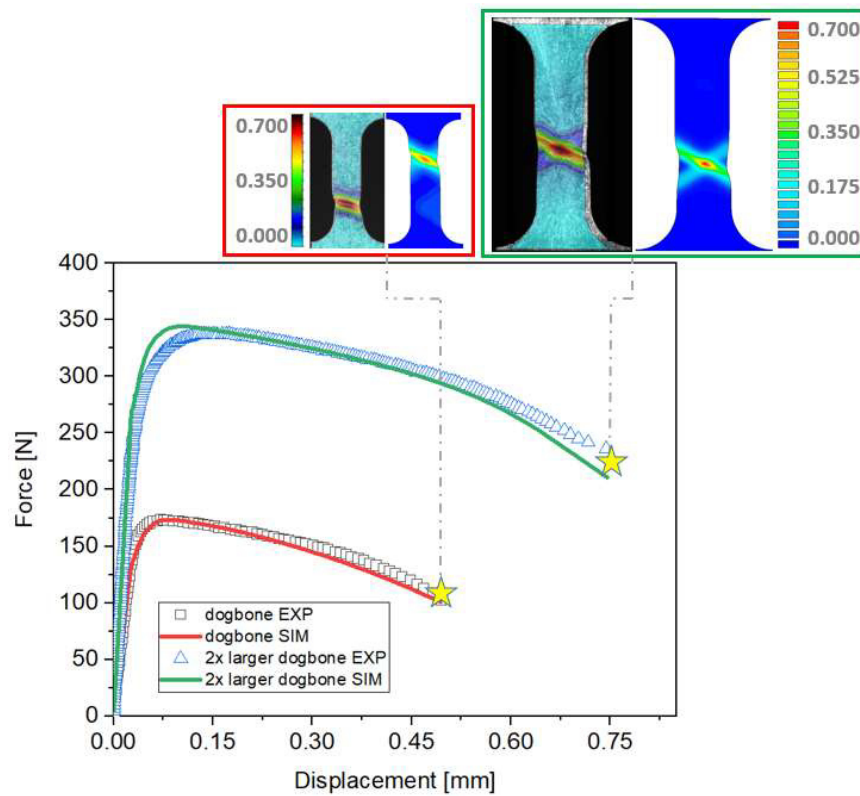


Fig. 3.5. Experimentally vs. numerically predicted force-displacement responses of a miniature dogbone specimen and a twice larger dogbone specimen. The star (★) marks the instant prior to failure. For the miniature dogbone the length scale parameter is $l = 0.195$ mm; for the larger dogbone the length scale parameter is $l_s = 0.390$ mm.

3.3 Application to a complex structure exposed to multiaxial loading

Unlike the simplified design of the thin-walled component used for material characterization (Fig. 3.1), the actual structure design has a rupture point in the middle of the bottom part as a safety feature in the mechanical system. Fig. 3.6 shows the details of the safety vent both from the outside perspective and a cross section view, taken from stereo microscopic observations. The right hand-side of the figure shows the corresponding views of the finite element model. Over the product life cycle, the structure endures growing internal pressure. A multiaxial stress state develops within the critical safety vent zone. The maximal endurable internal pressure will henceforth be termed the *burst pressure*.

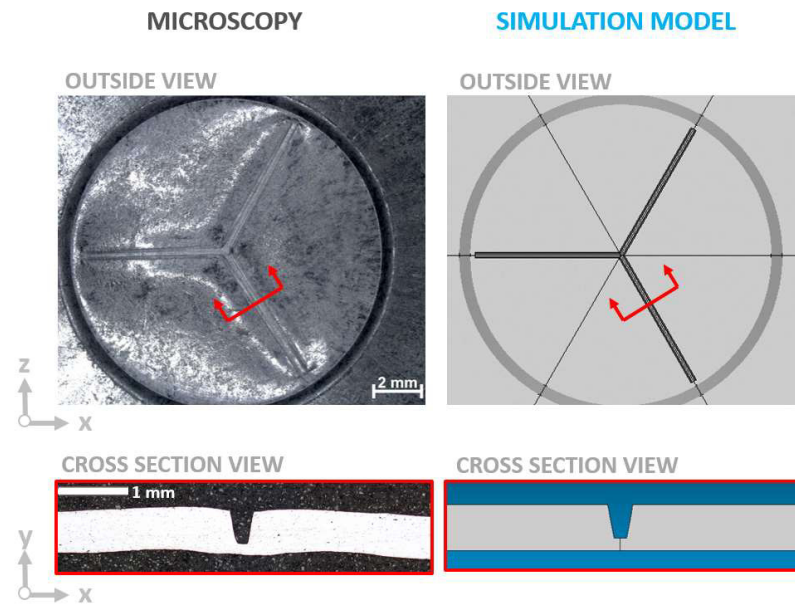
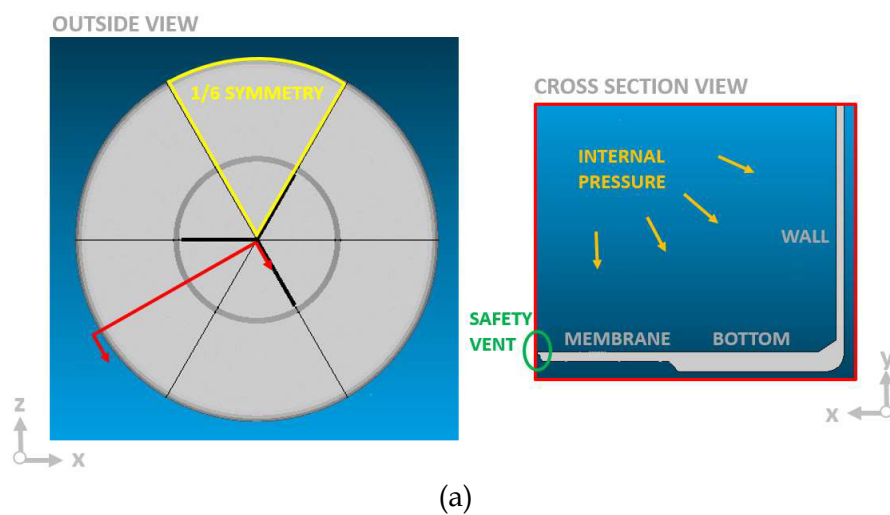


Fig. 3.6. Geometrical details of the analysed structure: outside and cross section views of the thin-walled aluminum component

3.3.1 Boundary conditions and loading of the mechanical system

The structural component is modelled with geometric 1/6-symmetry, as shown in Fig. 3.7a, to reduce the computational costs. Symmetry boundary conditions are specified on the cross-section surfaces (Fig. 3.7b), thus generating the constraints for displacement DOFs in the normal direction of the cross-section planes. The structure is fixed on the top of the wall (Fig. 3.7b), whereas the pressure is applied to all interior surfaces of the structure (Fig. 3.7b).



(a)

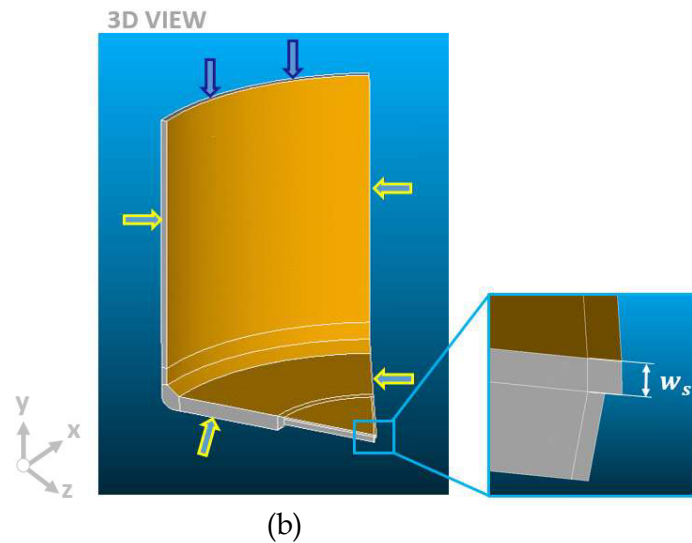


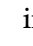


Fig. 3.7. Simulation model of the analysed mechanical system: (a) outside and cross section views, (b) 3D view with indicated boundary conditions: symmetry planes (), displacement in Y-direction set to zero on the top surface (), pressure on the interior surfaces (). The inset shows the gauge width w_s where the shear band forms.

3.3.2 Finite element model

The vent region represents a failure site and therefore the respective zone of interest must be discretized with high resolution. As it can be seen from the cross section views in Fig. 3.6, the geometrical dimensions of the safety vent are significantly smaller in size compared to the rest of the structural dimensions. Particularly the thickness of the vent detail, indicated as w_s in Fig. 3.7b, is remarkably small. In fact, the thickness of the vent detail, $w_s = 0.15$ mm, is the gauge length in the plane where the shear band forms prior to component failure and leads to a length scale parameter of $l_s = 0.015$ mm after applying the length scale correction (Eq. 3.10). Hence, the length scale of $l_s = 0.015$ mm represents the expected width of the strain localization band forming in the safety vent, imposing thus a minimal finite element size in the vent zone. Note that the corrected length scale l_s deviates ~ 10 orders of magnitude from the original length scale l determined from the calibration specimen, assuring thus that the regularization method distributes the strains of the numerical model across a realistic width.

The remaining parts of the structure are discretized by a coarser finite element mesh to keep the total number of elements within computationally manageable bounds, as shown in Fig. 3.8. The boundary between the fine mesh in the vent zone and the coarse mesh is placed far enough away from the vent in order to not affect the zone where plasticity and damage develop. The two regions with dissimilar mesh patterns are bound together by appropriate tie constraints. The complete structure is modelled by linear solid elements with full integration, used rather than shell elements because of the high ductile failure dependency on the three-dimensional and multiaxial local

stress state developing inside the structure. As a matter of fact, the mechanism of fracture preceded by localised necking, as revealed by the material characterization experiments, can be captured more accurately by solid elements.

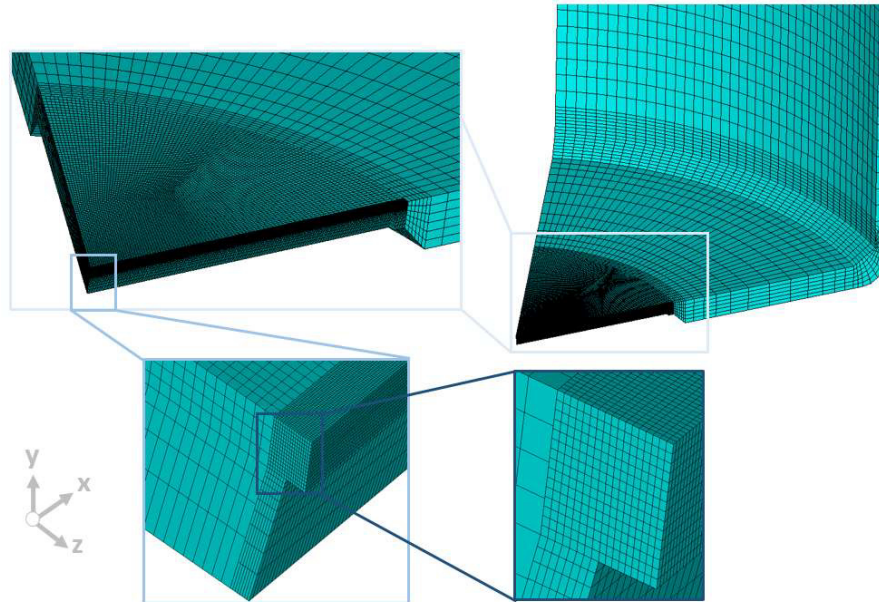


Fig. 3.8. Finite element model of the thin-walled structure: non-conformal mesh in the safety vent region

The mechanical system is loaded by a pressure P in small pressure increments, $\Delta P = 0.01$ MPa, in a static simulation performed under ANSYS Mechanical. The pressure P keeps increasing monotonically until the damage variable D reaches the value $D = 1$ in the first critical element, indicating that the burst pressure has been reached.

A large displacement increment is observed for small load increments ΔP after reaching the critical pressure of $P = 1.5$ MPa in the finite element simulation, i.e. at the onset of failure. This instability problem is known to pose convergence difficulties in implicit FE computations and requires numerical stabilization by artificial damping as well as enhancing the Newton-Raphson solution method by a line search algorithm (ANSYS Documentation). Therefore, a dashpot element was added at each node of a solid element, but only after reaching the critical pressure P . The accuracy of the numerical result was checked by comparing the stabilization energy to the total potential energy; the stabilization energy was found to be much less than the potential energy, i.e. within an acceptable tolerance of 1%.

3.4 Results and discussion

The FE results are compared to the measurements in terms of the burst pressure and the deformation under pressure prior to failure in Fig. 3.9. The evaluation point for determining the displacement both in the FE model and the experiment is the centre point on the bottom section indicated in Fig. 3.9b. Both the numerical and the

experimental results for the burst pressure show an increasing trend of the limit load with increasing membrane thickness. The reported values of the burst pressure show an excellent agreement with experimental data (Fig. 3.9a), confirming that the instant of failure has successfully been predicted. The simulations, however, generally slightly underpredict the displacement of the centre point in the bottom section (see the inset in Fig. 3.9b) for all investigated membrane thicknesses. The deviations of the numerically predicted maximum deformation prior to failure from the experimentally determined one may not necessarily be attributable to model inaccuracies but may also be due to the fact that deformation measurements in the midst of bursting are difficult to perform and thus known to be unreliable. By contrast, it is comparatively easy to measure the burst pressure, which will thus be used as a criterion for validating the numerical model. For comparison, the numerical results without non-local regularization are also shown in Fig. 3.9. and point to the underestimated predicted burst pressure for lower maximal deformation prior to failure. This was expected, as the strain-induced damage accumulates faster because the excessive strain localization is not prevented in this case. In addition, it is worth mentioning that a weak- or no-coupling significantly underestimate the structure's response, which was shown in a comparative study.

A close-up view of the failure site of the aluminum structure after testing under pressure is shown in Fig. 3.10. The micrographs captured by Scanning Electron Microscopy (SEM) show the shear lips on the fracture surface, see Fig. 3.10a. Contour lines of the stress triaxiality plot and Lode angle parameter are visualized in Fig. 3.10b. The contours are pointing to the high triaxiality in the failure zone (0.80) and Lode angle parameter close to 0.

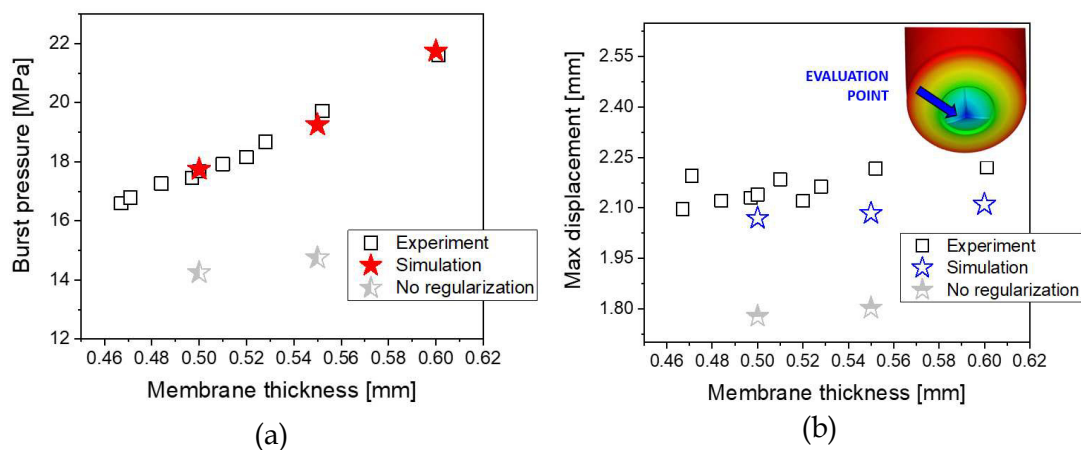


Fig. 3.9. Experimental vs. numerically predicted results for thin-walled aluminum component: (a) burst pressure for a variety of membrane thicknesses and (b) deformation prior to failure.

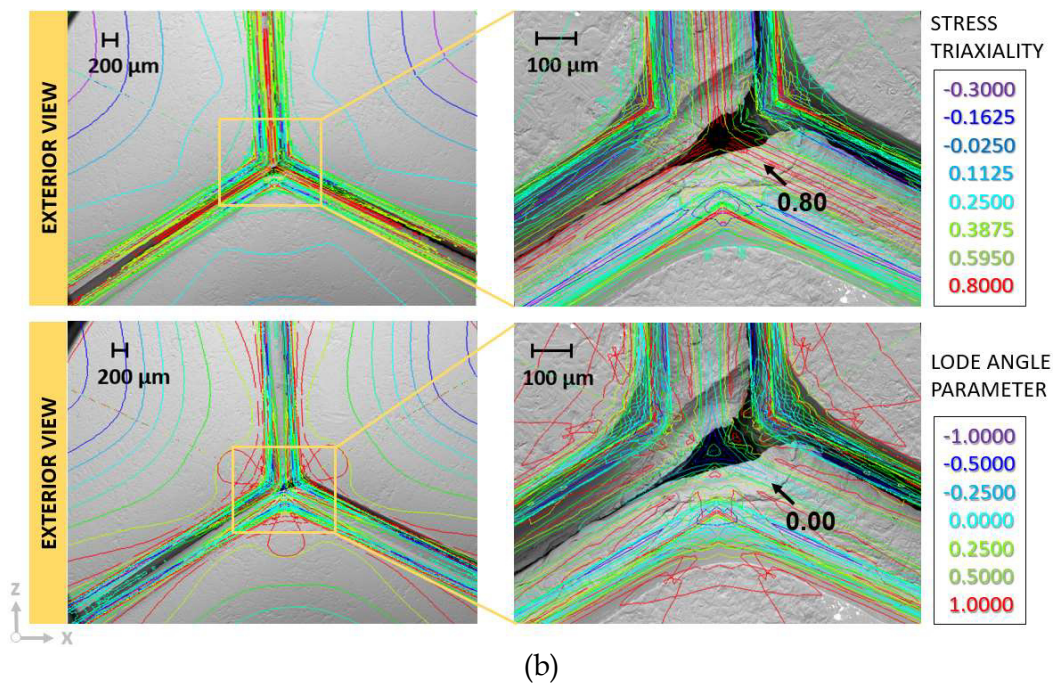
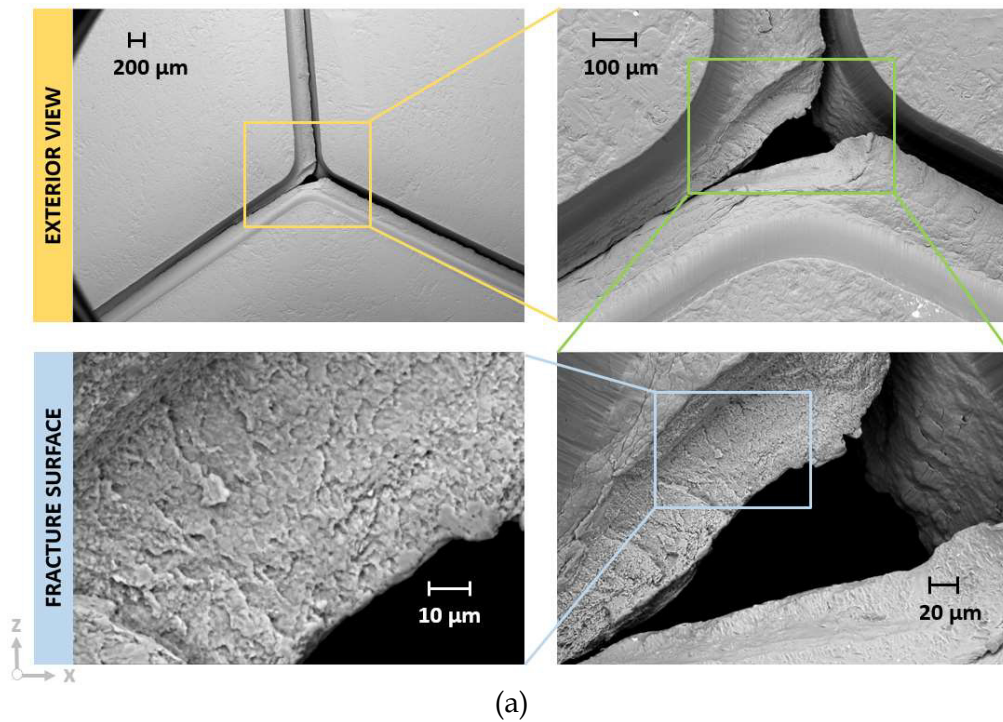


Fig. 3.10. Overview of the fracture surface of the failed aluminum component after testing: (a) Scanning Electron Microscopy (SEM) micrographs show a ductile fracture mechanism in the structure, revealing a sheared fracture surface; the centrepiece is broken out. (b) overlap of the stress triaxiality and Lode angle parameter contour lines from the simulation.

The comparison of the failure mechanism predicted by the numerical model and the mechanism documented by SEM is shown in Fig. 3.11. The damage plot indicates the location of the initiation of failure at the outer corner of the vent detail, marked as “damaged region” in Fig. 3.11. Detail C in the same figure depicts the distribution of stress triaxiality and the Lode angle parameter in the failed part. It can be seen that the highest value of stress triaxiality is concentrated near the outer corner, explaining thus the location of the maximal damage ($D=1$) as well. Simultaneously, the Lode angle parameter is close to 0 in the respective region, thereby accelerating the damage accumulation.

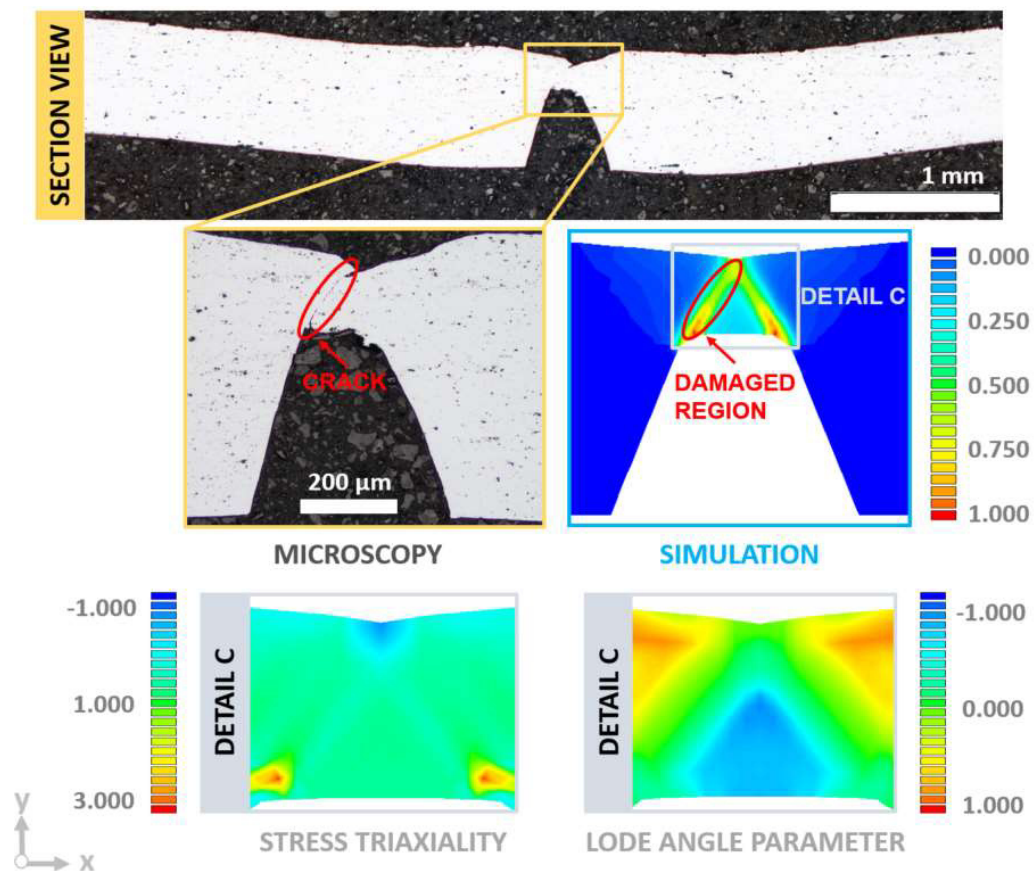


Fig. 3.11. Comparison of the failure mechanism predicted by the numerical model with the SEM documentation of the failed component: plot of damage as well as distributions of stress triaxiality and Lode angle parameter in the damaged zone.

The localization takes the form of a band of one tenth the band width observed in the calibration specimens. Note that the applied length scale correction allows to control the plastic strain localization in the FE model, convoluted by a Gaussian function of a width given by the variance l^2 (Eq. 3.8). The regularization method ensures thus the localization phenomena to be captured correctly in structures whose gauge lengths, i.e. the failure initiation zone, markedly differ in size, merely by adjusting the length scale parameter l determining the width of the localization band. The predicted

localization band in the failure zone (vent) for various mesh discretizations of the FE model is shown in Fig. 3.12. Three numerical models with different element sizes were set up; all of them have finite element sizes smaller than the length scale parameter $l = 0.015$ mm. The simulated distributions of the localised plastic strain agree well for different mesh resolutions, thus showing virtually no mesh dependency.

Ideally, for establishing an accurate value for the local fracture strain in a calibration specimen, the DIC strain measurements would have to approach to grain-level measurements, as highlighted by (Scales et al. 2016; Scales et al. 2019). However, it must be ensured that the experimentally observed strain localization is actually resolved by the finite element (FE) model discretization with reasonable computational costs. This will generally be an issue in real engineering structures where the damage zone is expected to be small compared to the component's dimensions. Hence, optimally the DIC resolution does not have to be overly fine but should be sufficient to pick up the local effects. As shown in Fig. 3.9a, the numerical prediction of the instant of fracture will still be correct, if and only if the experimentally resolved length scale by DIC is included in the model, which in this work is done via the parameter l . As a matter of fact, for materials undergoing large plastic deformation exaggerated DIC resolution could lead to extremely high local strains. Capturing them in a FE model would call for an excessively small element size, making the computation of a real world structure overly expensive.

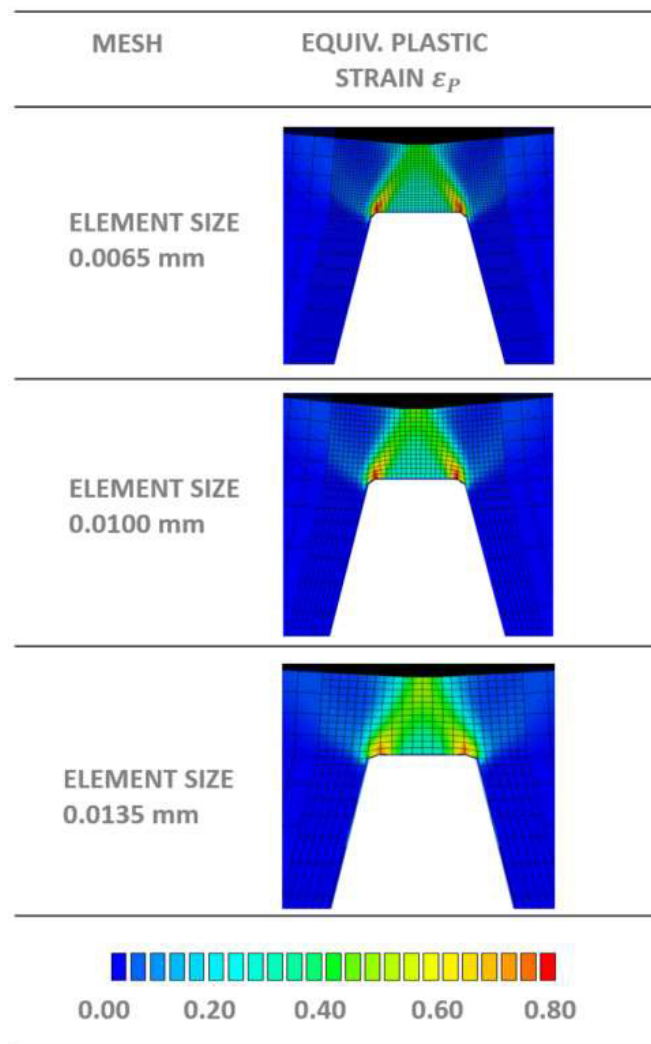


Fig. 3.12. The localization band in the structure for various 3 mesh discretizations of the FE model: plot of the equivalent plastic strain ϵ_p .

3.5 Summary and conclusion

We presented an application of the coupled ductile fracture locus model calibrated from miscellaneous ductile fracture experiments to a real scale aluminum component exposed to multiaxial loading. Not only the failure location prediction, but also the prediction of the instant of failure is in very good agreement with the experimental findings. The failure at the maximum endurable pressure of the structure is determined in the simulation as the point where the damage variable reaches the critical value $D = 1$. It is emphasized that both qualitatively and quantitatively correct failure predictions are reported in this work.

The main original contributions of the presented work are:

1. Experimentally validated, accurate failure predictions of the limit load, i.e. the burst pressure of the safety vent of an aluminum component, are achieved without inverse calibration for one specific loading scenario

occurring in the analysed structure. It is emphasized that the model performed well even in the case of an intricate geometry experiencing stress states ranging from plane-stress to plane-strain dominance where a competition between a tensile- and shear-dominated fracture mode is expected.

2. The model's true predictive ability was put at test in a scenario unknown a priori. The material constants were determined independent of the loading conditions in the real component. This guarantees the model reliability also for varying component designs having different distributions of the stress state parameters (stress triaxiality and Lode angle parameter). This provokes a different damage accumulation history tracked along the entire loading path by the presented model.
3. The presented model allows to use an arbitrary mesh for a complex structural geometry as long as the element size is small enough to capture the local effects. The distribution of localised plastic strain in the FE model virtually does not change for different mesh discretizations, confirming the reliability of the regularization method. The width of the localization band is realistically captured for failure zones vastly different in size, highlighting thus the importance of the simple length scale correction proposed for structures differing orders of magnitude from calibration specimens.
4. Realistic representation of the analysed engineering problem demonstrates the efficacy of the employed modeling approach. The presented stress state dependent and regularized damage model is simple-to-use and applicable to real world complex structural parts.

The model finds its application in attaining any given design target of the analysed component because it will perform reliably for arbitrarily modified geometrical designs. It is of a great use for achieving challenging goals that conflict each other, like reaching simultaneously both the lower burst pressure and a reduction of maximum deformation.

Acknowledgements

The author gratefully acknowledges the financial support under the scope of the COMET program within the K2 Center "Integrated Computational Material, Process and Product Engineering (IC-MPPE)" (Project No 859480). This program is supported by the Austrian Federal Ministries for Climate Action, Environment, Energy, Mobility, Innovation and Technology (BMK) and for Digital and Economic Affairs (BMDW), represented by the Austrian research funding association (FFG), and the federal states of Styria, Upper Austria and Tyrol. TDK Electronics is thanked for providing the material.

Chapter 4

Ductile crack formation modeling in pre-cracked solids using coupled fracture locus theory¹⁰

Ductile fracture locus models are extensively used in applied mechanics to predict the initiation of failure thanks to the ease of numerical implementation and simple calibration from experiments. The coupled fracture locus theory (Baltic et al. 2020a) has proven capable of predicting ductile failure of uncracked specimens experiencing various loading paths. Here, an attempt is made to investigate its potential to model complicated failure modes in pre-cracked structures. To verify the generality of the concept relying on the local stress state dependent fracture strain, the material model from (Baltic et al. 2020a) is adopted without any recalibration. A tensile test specimen with a side notch and a pre-crack is fabricated from an off-the-shelf engineering aluminum alloy. Mechanical testing revealed two dissimilar failure patterns whose ambiguity is elaborated in the numerical study. The coupled fracture locus theory combined with the local damage / element deletion approach is adopted as a local failure modeling method. The model features the stress-state dependent softening process resulting in a true stress-strain response dependent on the history of the stress triaxiality and Lode angle parameter. The numerical results show failure process predictions that are in accordance with experimentally observed failure modes in terms of the failure paths and the global force-displacement response. Fundamentally different failure processes, i.e. the mechanisms of strain localization and classical crack propagation, have been rather well captured. These results suggest high predictive capabilities of the method employed, which captures well the stress-state dependent damaging process governing the development of the failure mode.

¹⁰ This chapter has been submitted for publication in a peer-reviewed journal.

4.1 Introduction

The local damage and element deletion method as a ductile fracture modeling method has already been extensively treated in the literature and the latest Sandia Fracture Challenge (Kramer et al. 2019), but also predecessors (Boyce et al. 2014; Boyce et al. 2016), witness its success. In the latest computational challenge, where researchers were invited to predict crack initiation and propagation in an additively manufactured steel structure without knowing the experimental outcome, more than half of the participating groups employed the local damage approach. In fact, many of them identified the correct crack path in the analysed structure. Although the predictions of the crack pattern were encouraging, only a minority was able to calculate a global force-displacement response within the experimental bounds.

Damage modeling to predict the ductile failure can be used either in the framework of in a *coupled* or *uncoupled concept*, depending on whether the damage parameter influences the elastic-plastic behavior of the material or not. Most of the research efforts into ductile failure that follow the coupled concept and local damage use micromechanically based Gurson-like models (Gurson 1977; Tvergaard and Needleman 1984; Nahshon and Hutchinson 2008). Although more realistic, coupled concepts are somewhat impractical to use in engineering problems because of the rather complex material parameter determination. Applied mechanics, therefore, often reaches for uncoupled concepts because of the ease of numerical implementation and simple calibration from experiments, see e.g. (Bao and Wierzbicki 2004; Teng et al. 2008; Dunand and Mohr 2010; Khan and Liu 2012; Roth and Mohr 2016; Lou et al. 2017; Pack et al. 2018; Deole et al. 2018; McDonald et al. 2019). These uncoupled failure criteria, whose heart is a fracture locus that quantifies the dependency of ductile failure on the stress state (Bao and Wierzbicki 2004), have found increasing interest and application (Teng and Wierzbicki 2006; Mohr and Treitler 2008; Bai and Wierzbicki 2015; Pack and Mohr 2017; Ha et al. 2018). To circumvent a sudden deletion of a finite element, a partially coupled approach was developed (Li and Wierzbicki 2010; Beese et al. 2010; Paredes et al. 2016), where the damage-induced softening was introduced only in the post-initiation range.

Recently, the fracture locus theory was applied as a fully coupled concept in a damage mechanics framework (Baltic et al. 2020a, 2020b), keeping however the advantages of the uncoupled fracture locus models. The model features the stress-state dependent damaging process resulting in a true stress-strain response dependent on the history of the state variables. The plastic responses of tension samples experiencing a wide range of stress states were predicted with only very few model parameters. The model relies on the measured local failure strains; however, it involves a regularization as a function of the length scale over which the experimental strains are averaged for determining the fracture strain. Apart from ensuring mesh independency, the length scale, determined from experiments as the width of the shear band observed by Digital Image Correlation (DIC), makes the fracture locus calibration robust under variation of the spatial averaging of the experimental strain. Simulation results showed successful fracture initiation predictions in uncracked specimens undergoing various stress state evolutions.

In this work, the coupled fracture locus theory is used to model the failure evolution in a pre-cracked structure. A tensile test specimen with a side notch and a pre-crack is designed to initiate failure in a sheet metal with a thickness of 0.55 mm. The specimen is fabricated from an engineering component made of a commercial aluminum alloy. Mechanical tensile testing together with DIC analysis revealed two different crack patterns. A computational model of the tension experiment is built-up and studied using the coupled ductile fracture locus model (Baltic et al. 2020a), where the stress-state dependent damaging process rules the failure path. The competition between two failure patterns, with and without dominating strain localization, is numerically analysed and further discussed.

4.2 Experiments

4.2.1 Material, specimen design and testing

An aluminum alloy AA-1050 is chosen for the present study, belonging to the class of wrought commercial alloys. A broad spectrum of applications of this alloy ranges from large lightweight structures over car bodies to tiny electronic components.

All specimens are extracted by electrical discharge cutting (wire diameter of 0.25 mm) from a structural component made from 0.55 mm thick sheet. Side-notched tensile specimens are therefore machined and a pre-crack is initiated by cyclic loading with a stress ratio of $R = 0.1$. All specimens are 12 mm wide and feature a side notch radius of 0.25 mm. The exact specimen dimensions are given in Fig. 4.1. The lengths of the pre-cracks finally introduced into the individual specimens (a_0) are measured using a digital microscope (Shuttle Pix P400R), as shown in Fig. 4.2. The mean value of the measured pre-crack lengths is about 3.00 mm. In Fig. 4.2, a specimen is exemplary shown after the cyclic loading to initiate the pre-crack, where the two pictures present two different resolutions.

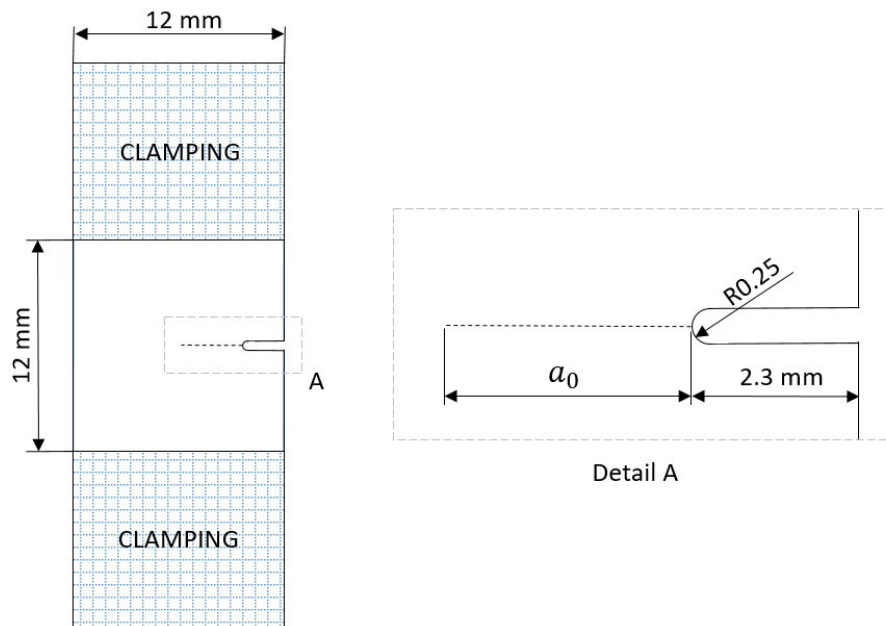


Fig. 4.1. Geometrical details of the pre-cracked specimen. The hatched areas of the specimen indicate the clamping regions.

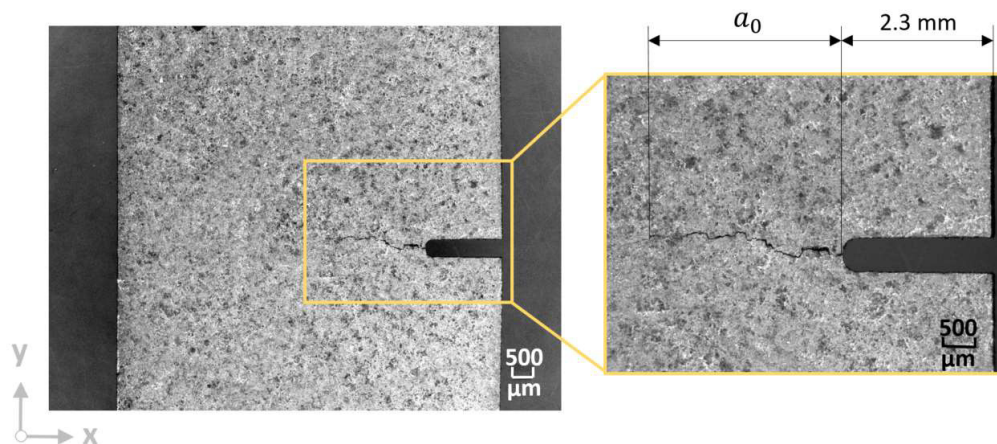


Fig. 4.2. Digital microscope image of the final specimen geometry showing the introduced pre-crack (close-up).

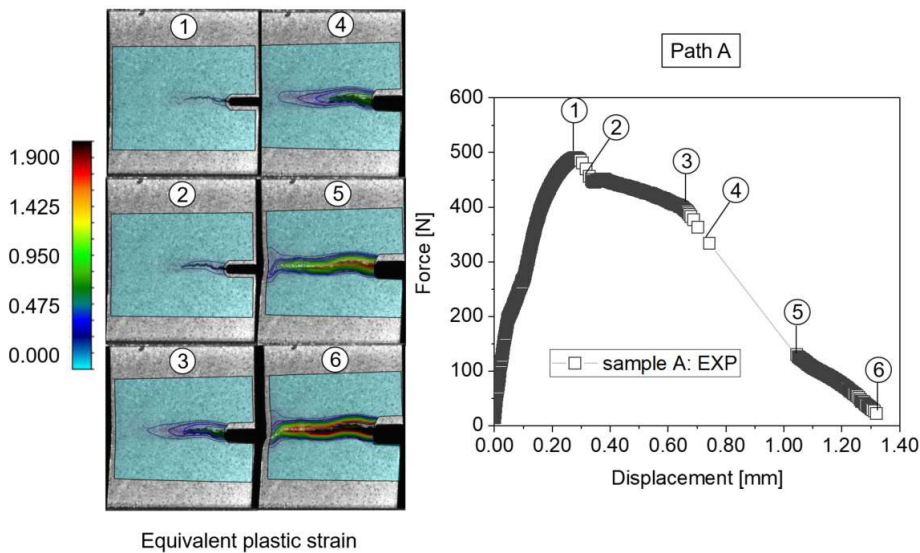
Tensile testing is carried out on a Bond-tester (Sigma Condor from XYZ-Tec) with a crosshead stroke resolution of $0.03 \mu\text{m}$ and a sample holder particularly designed for clamping miniature specimens. All experiments are performed under displacement control at a constant crosshead velocity of $0.1 \mu\text{m/s}$. During the experiment, about 1300 pictures are taken by means of a digital camera (microDACstandard, 1624×1234 pixel) positioned in front of the sample surface ensuring that the field of view covers the whole specimen. Using these photographs, the DIC analysis is conducted as well using the software VEDDAC7 (from Chemnitzer Werkstoffmechanik GmbH). As the natural surface pattern turned out to give enough features for DIC analysis, no additional speckle pattern was applied to the specimen's front face. The results of the

DIC analysis of the specimen's front face are used to apply the exact displacement histories in the simulation on the specimen boundary.

4.2.2 Experimental results

Three out of the four tested pre-cracked specimens exhibited a slanted failure path B as exemplarily displayed for one of the three in Fig. 4.3b, while the fourth exhibited an essentially straight failure path A as shown in Fig. 4.3a. In comparison to the specimen exhibiting the horizontal evolution (type A, Fig. 4.3a), the specimens undergoing the failure behavior of type B showed a higher peak force and more delayed force drop (see Fig. 4.3b). The force-displacement history of the specimen exhibiting failure behavior of type A (Fig. 4.3a) has a different, more complex profile.

Although a pre-crack had been introduced, the main mechanisms triggering the specimen's failure following the failure path B are diffuse necking and localization of the strain into a shear band, along with material ductile damage. Once the strain is extremely localised, the failure occurs simultaneously along the entire zone of localization, i.e. the material is suddenly separated, under unstable crack growth. The same mechanisms initiated the failure of uncracked specimens studied in (Baltic et al. 2020a). By contrast, the failure process in the specimen exhibiting the failure path of a type A features observable crack growth, i.e. the material separates gradually starting from the pre-crack and following the line of final failure as the deformation progresses.



(a)

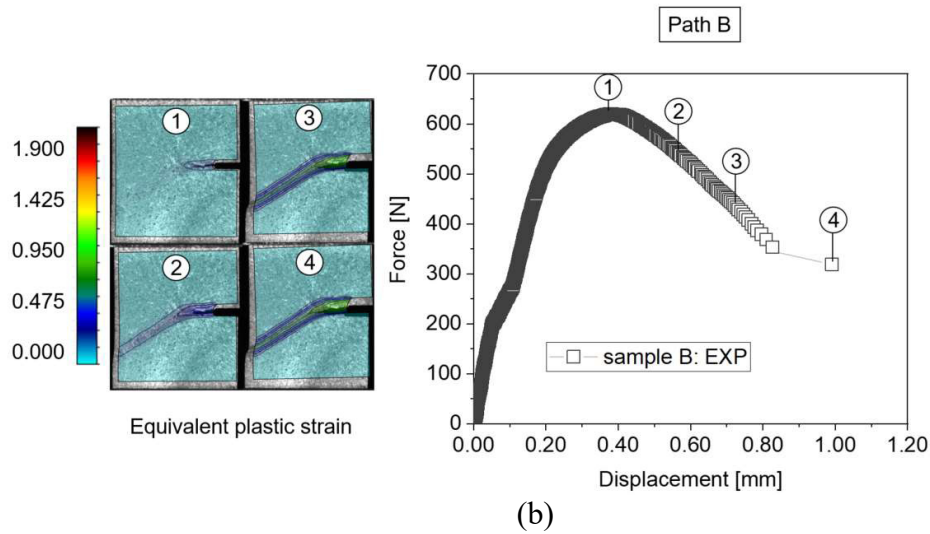


Fig. 4.3. Experimental results for tensile specimens with a side notch and a pre-crack: (a) force-displacement curve and DIC analysis of a specimen exhibiting a failure path of type A and (b) a specimen exhibiting a failure path of type B.

4.3 Computational model

4.3.1 Finite element model of the pre-cracked specimen

Finite element simulations of the experiments shown in Fig. 4.3 are performed using the ANSYS Mechanical simulation software. Full-integration 8-node 3D solid element (SOLID185 element type of the ANSYS element library (ANSYS Documentation)) are used to discretize the specimen, shown in Fig. 4.4. The mesh area represents the non-hatched area shown in Fig. 4.1.

Only one half of the specimen geometry is modelled, exploiting the symmetry of the specimen geometry in the through-the-thickness direction (z -direction, see Fig. 4.4). To represent a pre-crack in the model, the finite elements along the length of the measured pre-crack are detached, i.e. corresponding nodes are separated as shown in Fig. 4.4. Ahead of the pre-crack, all finite elements are fully connected. The mesh of the finite element model is designed such that the elements in the specimen center and around the pre-crack feature the same element size. Thus, the respective region is discretized by a uniform mesh of 0.09 mm element size. Approaching the upper and lower boundaries of the specimen, the element size is slightly coarsened to reduce the number of elements in the model. The same mesh pattern is swept through the specimen thickness. The displacement history measured by DIC is imposed onto the upper and lower specimen boundaries, respectively. In the symmetry plane, a normal displacement of zero (in z -direction) is imposed.

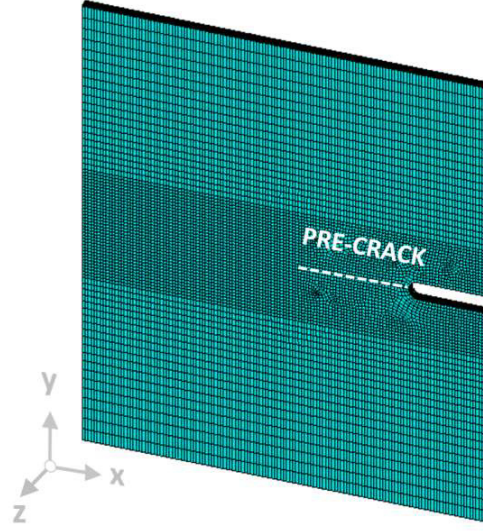


Fig. 4.4. Finite element model of the pre-cracked specimen. The finite elements along the marked (dashed) line are separated in y-direction to model the pre-crack. One half of the model is shown due to the symmetry in z-direction.

4.3.2 Constitutive model

The coupled ductile fracture locus theory as presented in (Baltic et al. 2020a) is employed to model the response of the pre-cracked specimens. This approach of modeling ductile failure links strain softening to damage evolution dependent on the current stress state along the complete strain path. The equivalent stress of the damaged material is defined by the Eq. (4.1):

$$\sigma_{eq} = \left[1 - \int_0^{\varepsilon_f} \frac{d\varepsilon_p}{\varepsilon_f(\eta, \bar{\theta})} \right] [\sigma(\varepsilon_p) + L(\varepsilon_p - e^p)], \quad (4.1)$$

where a fracture locus $\varepsilon_f(\eta, \bar{\theta})$ quantifies the dependency of the fracture strain ε_f on the stress state, i.e. on the evolution of the stress triaxiality η and Lode angle parameter $\bar{\theta}$. The stress triaxiality η is defined as the ratio of the hydrostatic stress σ_m and the equivalent von Mises stress σ_e , i.e.

$$\eta = \frac{\sigma_m}{\sigma_e}. \quad (4.2)$$

For the Lode angle parameter, a definition according to (Bai and Wierzbicki 2008) is adopted who transformed the Lode angle θ (Lode 1926; Zhang et al. 2000, 2000) to the normalized space; this Lode angle parameter $\bar{\theta}$ is defined as

$$1 \leq \bar{\theta} = 1 - \frac{6\theta}{\pi} \leq 1. \quad (4.3)$$

A conventional hardening function $\sigma(\varepsilon_p)$ has been modified in an additive manner by a nonlocal regularization term $L(\varepsilon_p - e^p)$, where ε_p and e^p are equivalent plastic strain and nonlocal plastic strain, respectively. The parameter L determines an adequate amount of regularization such that both force-displacement response and

local strain distribution are well described. A stress-state dependent damaging process rules the predicted crack path insofar as the damage variable,

$$D = \int_0^{\varepsilon_f} \frac{d\varepsilon_p}{\varepsilon_f(\eta, \theta)}, \quad (4.4)$$

is fully coupled to the plastic material flow and element stiffness. Once the accumulated damage in some point of the structure, i.e., in a finite element during the simulation, reaches the critical value $D = 1$, the element is eliminated from the stiffness matrix, while the total finite element analysis continues.

It is emphasized that the nonlocality introduced by variable e^p prevents the strain induced damage D to localise in a region of zero volume, that is, a size of a finite element for a discretized computational model. The e^p represents a weighted average of the equivalent plastic strain ε_p ,

$$e^p(x) = \frac{\int_B \psi(y:x) \varepsilon_p(y) dv}{\int_B \psi(y:x) dv}. \quad (4.5)$$

and the strain in the FE model is convoluted by a Gaussian function of a width given by the variance l^2 ,

$$\psi(y : x) = \frac{1}{(2\pi)^{3/2} l^3} \exp\left(-\frac{|y-x|^2}{2 l^2}\right). \quad (4.6)$$

(Baltic et al. 2020a) determined the parameter l from experiments as equal to the width of the strain localization observed by DIC and therefore referred to it as an *experimentally resolved length scale*. In this way, the implemented regularization of the damage model represents a function of the length scale over which the experimental strains are averaged for determining the fracture strain, crucial for model calibration. In general, to provide an unambiguous fracture strain, the fracture locus must be reported always together with its associated length scale.

In the context of the present study, the length scale l may be viewed as a link between two correlated theories, damage and fracture mechanics, as elucidated in (Mazars and Pijaudier-Cabot 1996). The definition of l as a finite, nonzero quantity ensures that the dissipated energy, necessary to form a crack, does not vanish. Thus, the damage model predicts a non-zero energy dissipated at fracture, as also assumed in fracture mechanics. The value of l and all the other material parameters in the present investigation are adopted from the preceding work (Baltic et al. 2020a) without any change, to verify the generality of the stress state dependent fracture strain concept.

4.4 Numerical results

Although the interpretation of the experiments might suggest that, statistically, the crack path B is more likely to be observed and thus a more conservative solution in terms of the fracture strain to nominally the same problem than the crack path A, we examine and consider the causation by numerical analyses. Potential uncertainties regarding deviations from the nominal geometry have already been considered in the

model because the specimens' geometries were measured and the length of the introduced pre-crack was documented by digital microscopy. Material inhomogeneities are disregarded because all the specimens were extracted from the same material and Scanning Electron Microscopy (SEM) and Energy Dispersive X-ray (EDX) analysis confirmed the uniformity of the material texture. In probing the problem further, the test setup is thus considered as the main suspected determinant for the preferred failure path.

The simulation of the pre-cracked specimen are therefore performed under different boundary conditions to examine the influence of the load alignment and verify if the assumption of the perfect clamping of the specimen is justified. It was suspected that the potential uncertainties of the test setup might determine whether the failure follows one path (A) or another (B). Fig. 4.5 shows numerically predicted failure paths after imposing the displacement history measured by DIC on the specimen boundaries for specimens A and B, exhibiting failure paths A and B, respectively. Note that the lengthier pre-crack ($a_0 = 3.535$ mm) distinguishes the geometry of the specimen A from specimen B ($a_0 = 2.434$ mm). In addition, a simulation of an ideally clamped specimen with a fixed lower boundary is performed. The results shown in Fig. 4.5 suggest that the experimental imperfections impose different loading conditions onto the sample and thus trigger different crack paths. In the numerical experiment conducted on specimen A, the applied boundary conditions from DIC allowed a slight rotation of the specimen. Therefore, the failure propagates horizontally at the beginning and only in the final stages of the experiment, shortly before the collapse, the specimen starts kinking due to shear band formation. Based on this numerical study, it becomes apparent that minor sliding of the sample through the clamping allowed an additional rotational degree of freedom and resulted in failure evolution of a type B.

Comparing the numerical results for the sample B having the DIC-measured displacement history applied on the boundaries, with the results of an ideally clamped sample B having the lower boundary fixed, one can observe that the predicted failure evolution are in accordance with each other (Fig. 4.5). This type of loading imposed causes a clear formation of the strain into a shear band just in front of the introduced pre-crack.

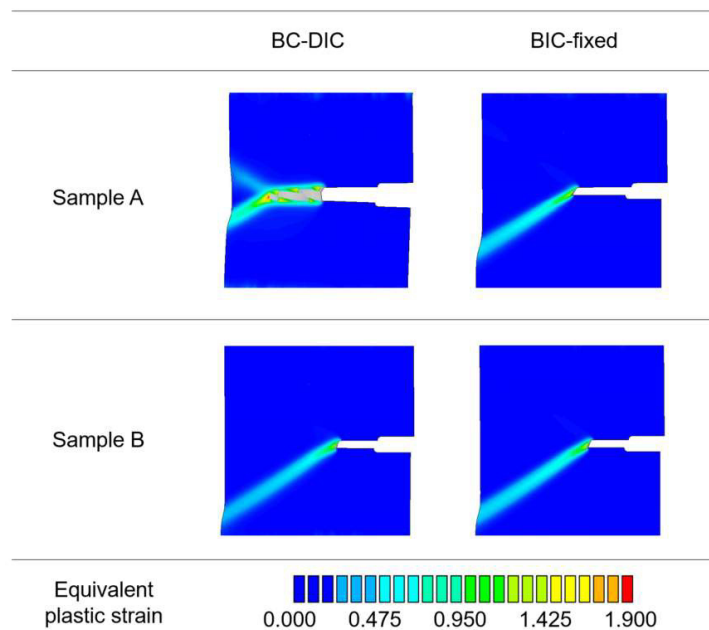
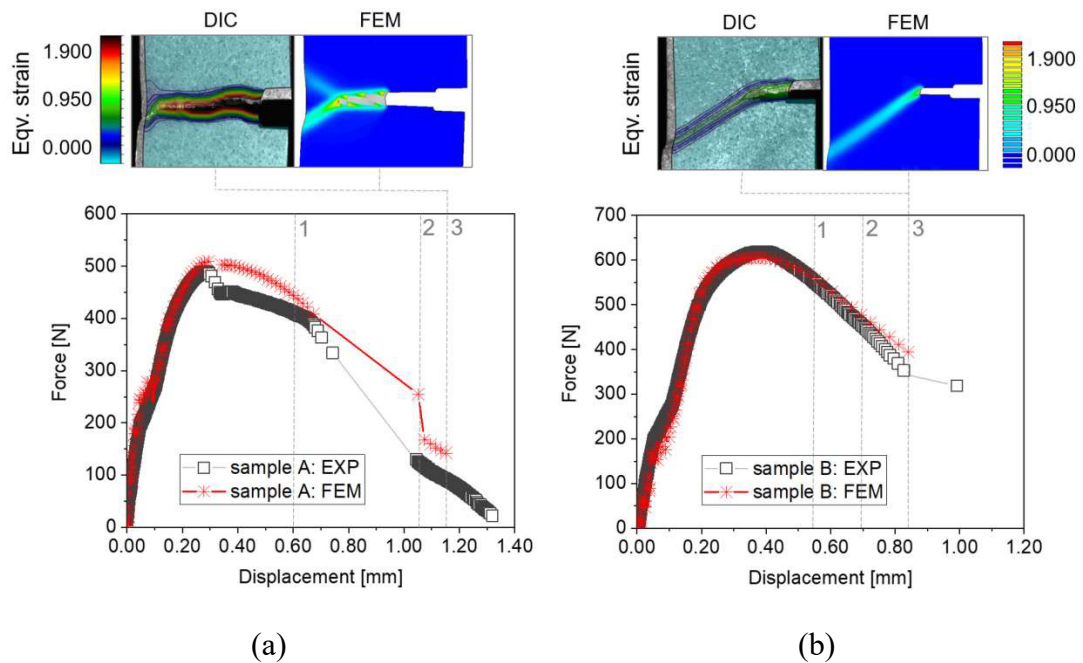


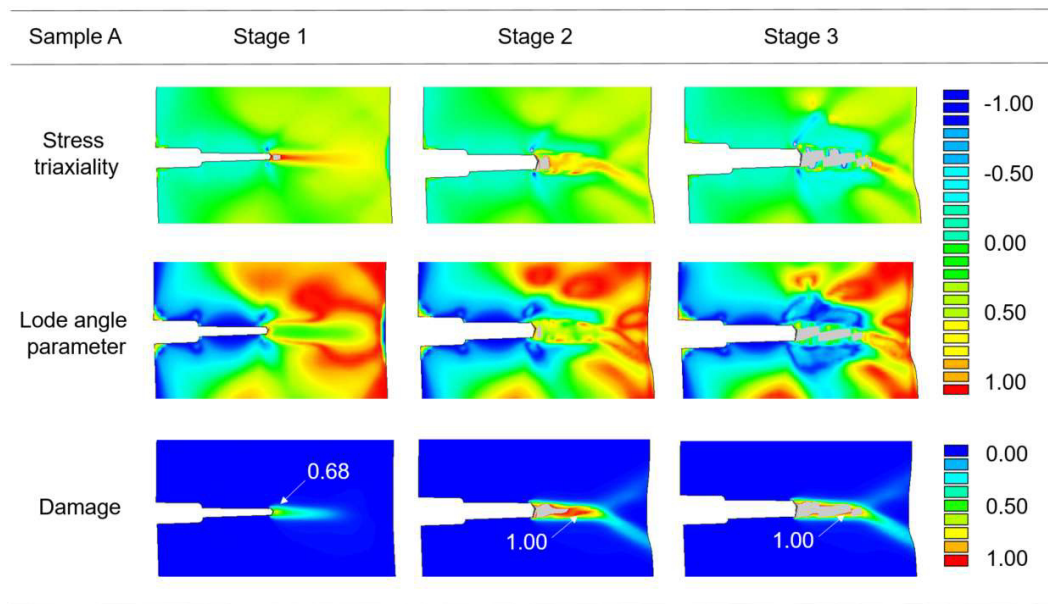
Fig. 4.5. Numerical study of the response of the pre-cracked specimen under different boundary conditions (BC): numerically predicted failure path for applied DIC-measured displacement history (BC-DIC) compared to a model of an ideally clamped specimen with fixed lower specimen boundary (BC-fixed); for samples A and B.

The performed experiments are nevertheless very valuable for the examination of the numerical model's performance because in any case the comparison between the numerical and experimental results allows to assess the model's true predictive capabilities across different failure events. Fig. 4.6 compares calculated force-displacement curves from the finite element simulation with experimentally determined data points. It is highlighted that the data obtained from these experiments are in no way included in the model calibration. The deviation of the calculated force-displacement curve for the sample A is attributed to the adopted material parameters and the length scale l from (Baltic et al. 2020a) without any further adjustments. Note that the overall force at failure is higher for sample B than for sample A, because there is still significant cross-sectional area carrying the applied load, before the sample B fails suddenly without time-resolvable crack propagation. This is because the stored elastic energy is high enough to provoke an unstable crack growth as soon as the crack is initiated. On the contrary, the remaining load carrying area for specimen A is significantly reduced.

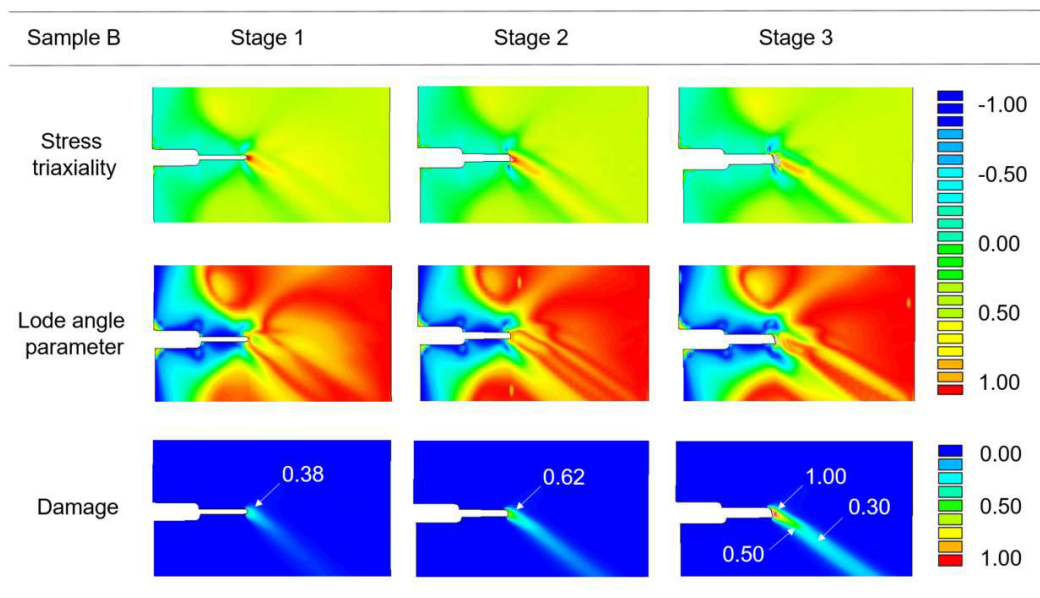
These rather satisfactory numerical predictions are attributed to the material model's main feature, i.e., the stress-state dependent damaging (softening) process that takes into account the history of the stress state variables (stress triaxiality and Lode angle parameter). Consequently, the damaging process controls the failure path in the numerical model. The evolution of the stress state variables (stress triaxiality and Lode angle parameter) upon straining is visualised in Fig. 4.6c and Fig. 4.6d for specimens A and B, respectively, for three stages marked in the force-displacement

curves of Fig. 4.6a and Fig. 4.6b. Stage 3 stands for the instant prior to the specimens' full separation, i.e. final failure. Looking closely at the evolution of these mechanical fields in sample A (Fig. 4.6c), it becomes apparent that a particularly rapid increase of damage D is caused by the high stress triaxiality in front of the pre-crack and a Lode angle parameter close to zero. This combination of the stress state parameters represents the most critical valley of the fracture locus, where the material has the lowest ductility (the shape of the adopted fracture locus can be found in (Baltic et al. 2020a)). On the other hand, the Lode angle parameter in the zone of strain localization of the specimen B (Fig. 4.6d) is close to 1, meaning that it interferes with high stress triaxiality, which nevertheless dominates and determines the failure path. Furthermore, the non-zero damage ($D > 0.3$) in stage 3 along the area of the specimens A and B exhibiting some retained load carrying capacity (Fig. 4.6c and Fig. 4.6d) implies that a material change on the local level is imperative to capture correct mechanical response of the analysed specimens.





(c)



(d)

Fig. 4.6. Comparison of experimentally recorded (EXP) and numerically calculated (FEM) force-displacement curves for (a) sample A and (b) sample B; the insets show the equivalent strains recorded by Digital Image Correlation (DIC) and calculated numerically (FEM). Visualisation of the numerically computed evolution of stress triaxiality, Lode angle parameter and damage in sample A (c) and sample B (d); the plots show the fields in the center plane of the sample.

4.5 Summary and conclusion

The goal of this computational study was to benchmark the predictive capabilities of the coupled fracture locus theory on tensile experiments of pre-cracked specimens. The fundamental generality of the concept relying on the local stress state dependent fracture strain is assessed insofar as the damage model established on uncracked specimens is adopted without any adjustments. The mechanisms of strain localization along with material damage and classical crack propagation have been successfully predicted. Fundamentally different failure processes under marginally different loading conditions have been thus rather well captured for nominally the same problem, which implies that the failure processes can be well described knowing merely the fracture locus of the material together with its associated length scale.

These results suggest that the already established regularized damage model that relies on fracture strain measurements even leads to reasonable failure predictions for a pre-cracked structure, in fact without knowing the experimental outcome before. It is emphasized that the fracture strains must be reported in conjunction with their associated length scale, that is, the length over which the experimental strains are averaged. The present study demonstrates that the so-established damage model yields realistic results even for a classical crack propagation problem.

Acknowledgements

The author gratefully acknowledges the financial support under the scope of the COMET program within the K2 Center “Integrated Computational Material, Process and Product Engineering (IC-MPPE)” (Project No 859480). This program is supported by the Austrian Federal Ministries for Climate Action, Environment, Energy, Mobility, Innovation and Technology (BMK) and for Digital and Economic Affairs (BMDW), represented by the Austrian research funding association (FFG), and the federal states of Styria, Upper Austria and Tyrol. TDK Electronics is thanked for providing the material.

Chapter 5

Machine learning assisted calibration of a ductile fracture locus model¹¹

While several different specimen geometries are typically required to calibrate a ductile fracture locus model, this article presents for the first time a calibration methodology that uses one single specimen geometry. This is accomplished by a computational framework that combines finite element modeling (FEM) and artificial neural network (ANN). The ANN is trained using merely the numerical experiments on a shear tension specimen, where combinations of the model parameters are used to generate the training database. The local displacement fields and global force-displacement histories are extracted throughout the complete numerical experiment and passed to the ANN. Therefore, the influence of the local stress state on the evolution of the local deformation is implicitly taken into account. The trained ANN is verified by evaluating its predictability of material parameters of FE simulations unseen in the training stage. The experimental data obtained from the shear tensile test using Digital Image Correlation is introduced to the trained ANN to identify the parameter set that predicts the real mechanical response of the shear specimen. Three different ANN architectures with distinguished input representations are studied. It turns out that all of them can acceptably describe the experimental behavior of not only the calibration specimen but also the specimens not used for training the model.

¹¹ This chapter has been published in Materials & Design as an open access article (<https://www.sciencedirect.com/science/article/pii/S026412752100157X?via%3Dihub>).

5.1 Introduction

Ductile damage and fracture modeling is essential for a broad spectrum of metal alloys applications, ranging from large lightweight structures over car bodies to tiny electronic components. Although sophisticated stress state dependent damage models have been proposed in the literature, the complexity of the calibration procedure often hinders their application in the aerospace, automotive and electronics communities.

For its simplicity and ease of implementation, uncoupled fracture initiation models are convenient for industrial purposes and widely used in applied mechanics, among others (Bao and Wierzbicki 2004; Dunand and Mohr 2010; Khan and Liu 2012; Roth and Mohr 2016; Lou et al. 2017; Deole et al. 2018; Ha et al. 2018; McDonald et al. 2019; Cheng et al. 2017; Jang et al. 2020). Their heart is a fracture locus that quantifies the dependency of ductile fracture on the stress and strain states (Bao and Wierzbicki 2004). (Baltic et al. 2020a) took a step further and embedded the fracture locus concept into a coupled damage mechanics framework. Either used in uncoupled or coupled mode, ductile fracture models require knowledge of the strain to fracture as a function of the stress state for proportional loading for their straightforward calibration. An ideal case of a constant strain-history path is possible to achieve just in special cases (Roth and Mohr 2016, 2018). As imposing constant proportional loadings up to failure over the complete stress state domain is extremely difficult, if not impossible, determination of the actual fracture locus from experimental measurements becomes questionable.

In addition to the experimental challenges mentioned above, there are uncertainties related to the finite element (FE) simulations which are indispensable for extracting the evolution of mechanical fields in a material point, i.e. the progress of the stress triaxiality and Lode angle parameter upon straining. Each experiment has to be studied by FE analysis to identify the stress and strain fields. (Dunand and Mohr 2010) demonstrated that spatial and time discretization errors might greatly affect the evolution of both equivalent plastic strain and stress triaxiality. Furthermore, the location of the onset of fracture in the computational model is frequently assumed to coincide with the location of the highest equivalent plastic strain. However, because of the stress state effects, the most strained element does not necessarily have to reach the critical damage value first which defines the instant of the onset of fracture in a FE model. Furthermore, the analysis of the mechanical fields discussed beforehand often relies on damage-free plasticity, although there is ample evidence that coupled damage plasticity models provide more realistic results in structural computations.

In this work, a machine learning supported calibration of a ductile fracture locus model is investigated in an attempt to overcome the above challenges in experimental and computational mechanics. Several studies already testify the great potential of artificial neural network (ANN) systems for material parameter identification. For instance, (Abbassi et al. 2013) followed the ANN based identification strategy to calibrate the parameters of the Gurson-Tvergaard-Needleman (GTN) model (Gurson 1977; Tvergaard and Needleman 1984) by using the X and Y displacements of the

specimen's middle point. (Abendroth and Kuna 2003, 2006) employed the load-displacement curve of a small punch test to train the ANN and find the damage and fracture properties modelled by the GTN model as well. (Aguir and Marouani 2010; Marouani and Aguir 2011) used an ANN to find the parameters of the GTN model employed in sheet metal blanking simulations. More recently, (Sun et al. 2020) also used the information from the load-displacement curve for ANN training to determine the damage parameters of the shear modified GTN model (Nahshon and Hutchinson 2008).

We present a computational framework for the determination of material constants by a machine learning method that integrates finite element (FE) simulations with ANN, similar in purpose but significantly different from the previous works in the following aspects:

- training data selection: the data passed from FE to ANN model consists of (i) the images of a complete local displacement field and (ii) the values of global force-displacement curve. Both (i) and (ii) data are extracted throughout the complete numerical experiment;
- material model employed: a machine learning supported calibration of a ductile fracture locus model will be attempted for the first time in the following sections.

The main advantage of the proposed calibration strategy stems particularly from the above specific training data selection. While using only one single calibration specimen, the presented approach allows to make use of all information accessible in the experiment, i.e. the local deformation influenced by the stress state and the damage state. In particular, assisting the calibration of a specific fracture locus model by ANN allows to circumvent extracting and averaging the evolution of stress state variables in a material point from numerical models of various calibration specimens. Therefore, no assumptions regarding the choice of an element for extracting the loading paths need to be adopted any longer.

The framework features (1) training of the ANN merely from numerical experiments, (2) examination of the ANN model's quality by assessing the predictability of material parameters used in FE simulations unseen in the training stage, (3) feeding the experimental data to the trained ANN to find the set of parameters that models the behavior of real experiment and (4) validation on different sample geometries not used for the training.

The goal of the present study is to find a robust set of parameters that accurately models the mechanical behavior and the instant of fracture of the analysed ductile material. We limit our attention to the parameters of the coupled damage model based on the fracture locus introduced in the preceding work (Baltic et al. 2020a). Instead of performing a series of ductile fracture experiments on various sample geometries to characterize the macroscopic mechanical response of the investigated alloy, a single sample geometry is analysed numerically by FE simulations. A shear tension specimen is modelled to study the sensitivity of the numerical response to parameter variations selected by a three level full factorial experimental design. The

data extracted from the FE models that are passed to the ANN will be referred to as a *training database*. The ANNs used here belong to the class of convolutional neural networks (CNN), which are chosen because of their pattern recognition capability. In particular, CNNs are able to exploit translation and scale invariance, making them generally more data efficient for most pattern recognition tasks. The ANN key features include one dimensional (1D) and three dimensional (3D) convolution layers with subsequent max pooling, and, in addition, two regularization approaches applied together to mitigate the overfitting of the parameters to be estimated.

5.2 Constitutive model: governing equations

The coupled ductile fracture locus model employed in the sequel is briefly summarized below to the reader's convenience. Details on the model formulation can be found in (Baltic et al. 2020a). Since the fundamental mechanisms of ductile fracture are rather well understood, cf., e.g., the review articles (Pineau et al. 2016; Benzerga et al. 2016), the constitutive equations are preserved to keep the physical foundation of the model. The function equations are thus predetermined, and the ANN is used for determining the constants of this given function.

5.2.1 Coupled ductile fracture locus model

The unified approach introduced in (Baltic et al. 2020a) comprises the theories for ductile fracture locus (Lou and Huh 2013), damage mechanics (Lemaitre 1985) and regularization (Anand et al. 2012). The model proposes modeling strain softening linked to damage evolution dependent on the current stress state along the strain path. The equivalent stress required for yielding of the damaged material matrix is described by

$$\sigma_{eq} = \left[1 - \int_0^{\varepsilon_f} \frac{d\varepsilon_p}{\varepsilon_f(\eta, \bar{\theta})} \right] [\sigma(\varepsilon_p) + L(\varepsilon_p - e^p)], \quad (5.1)$$

where a three-dimensional fracture locus $\varepsilon_f(\eta, \bar{\theta})$ defines a function that returns the fracture strain ε_f at a general multiaxial stress state given by the stress triaxiality η and the Lode angle parameter $\bar{\theta}$. A linear damage accumulation rule, $\frac{d\varepsilon_p}{\varepsilon_f(\eta, \bar{\theta})}$, where $d\varepsilon_p$ denotes the differential increment of the equivalent plastic strain ε_p , quantifies the local ductile damage D assumed to accumulate at each point in the continuum prior to failure. A softening factor is defined as a linear function of the damage variable, $[1 - \int_0^{\varepsilon_f} dD]$, to capture the stress state effects on the plastic flow, $\sigma(\varepsilon_p)$. An additional regularization term, $L(\varepsilon_p - e^p)$, modifies a conventional hardening function $\sigma(\varepsilon_p)$ in an additive manner. Note that the regularization is applied to the current yield strength and not to the initial undamaged one. The variable e^p represents a weighted average of the equivalent plastic strain ε_p over a specified strain distribution function f that follows a Gaussian distribution. The implemented

regularization distributes the strains of the FE model over a width defined by a length scale parameter l contained in the strain distribution function f . As the influence of the softening and regularization terms interfere, the parameter L should be calibrated to produce an adequate amount of regularization.

The linear damage accumulation rule is a simple form of mapping all possible fracture surfaces obtained from different strain paths onto a single fracture locus given by (Lou and Huh 2013),

$$\varepsilon_f(\bar{\theta}, \eta) = \frac{c_3}{\left(\frac{2}{\sqrt{\bar{\theta}^2 + 3}}\right)^{c_1} \left(\frac{\langle 1 + 3\eta \rangle}{2}\right)^{c_2}} \quad \langle x \rangle = \begin{cases} x & \text{when } x \geq 0 \\ 0 & \text{when } x < 0 \end{cases} \quad (5.2)$$

where the material constants $\{c_1, c_2, c_3\}$ should be determined. c_1 and c_2 model the stress state dependency of the underlying damage process, whereas c_3 represents the magnitude of the fracture locus without influencing its final shape. The fracture strain, ε_f , is herein defined as the maximum local equivalent plastic strain just before structural failure.

5.2.2 Unknowns for the ANN model

The three parameters $\{c_1, c_2, c_3\}$ of the fracture locus defined by (Eq. 5.2) are to be found from a shear tension experiment. As c_1 reflects the influence of the Lode angle parameter, $\bar{\theta}$, whose variation in the shear tension experiment (see subchapter 3.1.) is expected to be minimal, it cannot be determined properly from this experiment. Accordingly, c_1 will be fixed in the following to $c_1 = 2.082$, the value found in (Baltic et al. 2020a). Thereby we restrict ourselves to only two unknowns $\{c_2, c_3\}$. Given that c_2 modulates the dependency of the fracture strain on stress triaxiality, whose effect is predominant, c_2 is subject to ANN identification together with c_3 , which controls the overall magnitude of the fracture strain. The regularization parameter L controlling the effect of added (artificial) hardening is to be identified by ANN as well because it has a strong impact on the strain localization. For the latter purpose, the complete strain distribution is accessible to the ANN in the form of the full surface displacement field evolution that is fed into the model.

Accordingly we proceed with 3 unknown parameters to be identified by ANN, i.e. $\{c_2, c_3, L\}$. The fracture locus and regularization parameters of the material model employed in the sequel are summarized in Table 5.1. The remaining model parameters, i.e. elasticity as well as plasticity parameters defining the hardening function $\sigma(\varepsilon_p)$ (see Eq. 5.1), are taken from (Baltic et al. 2020a).

Table 5.1. Material parameters to be identified by the ANN

Ductile fracture locus parameters	c_1 [-]	c_2 [-]	c_3 [-]
	2.082*	?	?
Regularization parameters	l [mm]	L [MPa]	
	0.195**	?	

* c_1 is fixed and omitted from the ANN; cf. the main text for a detailed discussion.

**The length scale l is determined from experiments as the width of the shear band observed by Digital Image Correlation (Baltic et al. 2020a).

5.3 Computational framework for material parameter identification

5.3.1 Finite element model of the shear tension experiment

The finite element model of the shear specimen comprises one-half of the specimen geometry, as appropriate symmetry conditions in xy -plane are applied (see Fig. 5.1). The model is discretized by 8-node solid elements (ANSYS Element Library SOLID185) with an element length of about 0.043 mm and 7 elements over the thickness. The model's total thickness is 0.28 mm, which equals one half of the thickness of the real specimen machined from sheet material. The displacement history measured experimentally is applied to the upper boundary of the model and the simulations are carried out using the FE code ANSYS Mechanical APDL (ANSYS Documentation). The choice of the parameter sets of the material model employed is further discussed in the following subchapter.

In particular, this specimen was selected among the others (notched tension and dog-bone) because a closer look at the evolution of mechanical fields in the shear specimen reveals that at least one stress state parameter, i.e. the Lode angle, remains constant for the most part of the strain path (Baltic et al. 2020a). The stress triaxiality increases from low (0.00) over moderate (0.25) to high values (0.60); a detailed analysis of the discussed loading path can be found in (Baltic et al. 2020a). Being able to omit the influence of the Lode angle (and skip the determination of c_1), and having a large range of stress triaxiality and total fracture strain values for determining c_2 and c_3 , is expected to facilitate the learning process of the ANN.

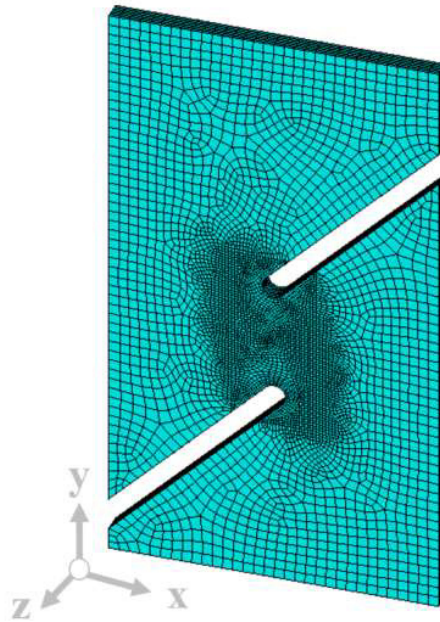


Fig. 5.1. Finite element model of the shear tension specimen

5.3.2 Training database

The sensitivity of the numerical response to material model parameter variations is studied following a three level full factorial experimental design. The relationships between parameters $\{c_2, c_3, L\}$ are explored through finite element analysis of 27 models in total, representing 27 different positions in parameter space, arranged on a rectilinear grid, with 12 middle-edge positions (nodes), 12 corner nodes and 3 centre nodes, as shown schematically in Fig. 5.2. Although there are somewhat more efficient designs like e.g. (Box and Behnken 1960) requiring fewer simulation runs than the full factorial one, the later was selected particularly because it covers just about every possible parameter combination. The ANN model is thereby supplied with high quality data. Yet, a reasonable parameter range has to be chosen to ensure that the actual parameter values for modeling the experimental behavior lie within the limits of the training data. For every parameter, three levels are used, (i) the low value, (ii) the middle value and (iii) the high parameter value (Table 5.2).

The selected range has to ensure that the domain of design space where the actual experiment falls is captured. Here, the choice of the design space was guided by the preceding work (Baltic et al. 2020a). Starting from the values found in the referred work, the design variables are varied systematically and iteratively to obtain the training database well-distributed around the actual experiment, see Fig. 5.3.

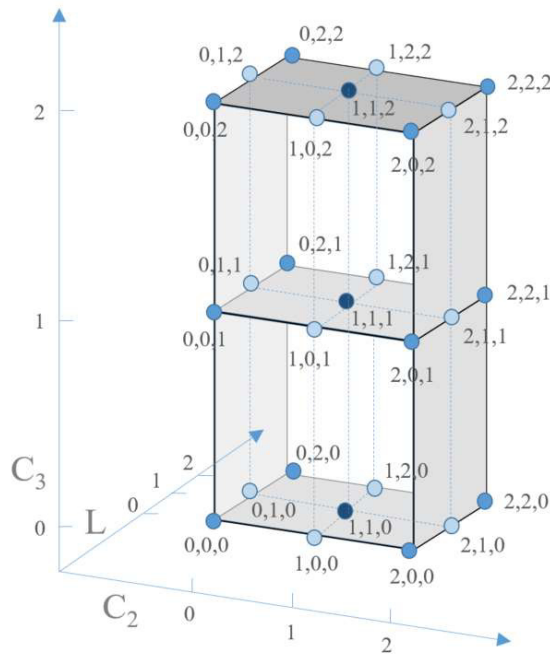


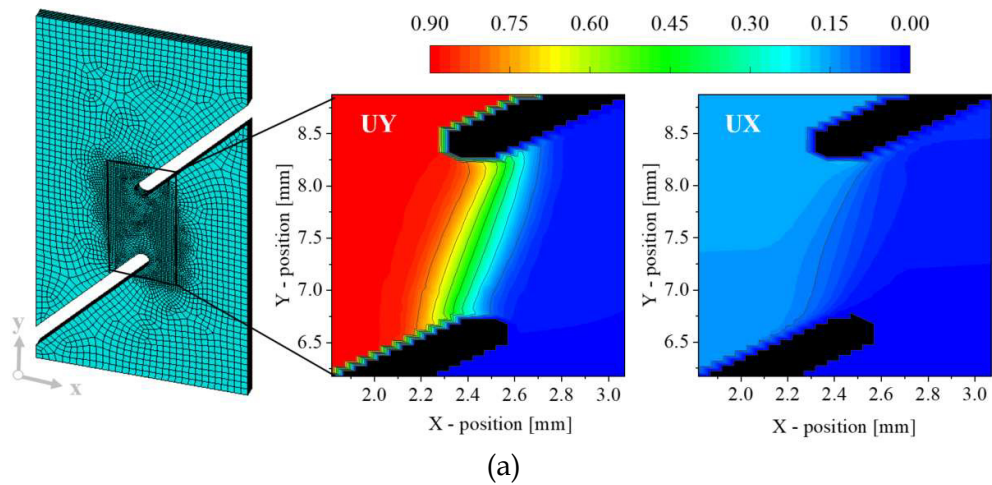
Fig. 5.2. Design of numerical experiments following the three level full factorial: 3-variable system with 3 levels (0 = low value, 1 = middle value, 2 = high value) arranged on the middle edge nodes (○), corner edge nodes (●) and centre nodes (●).

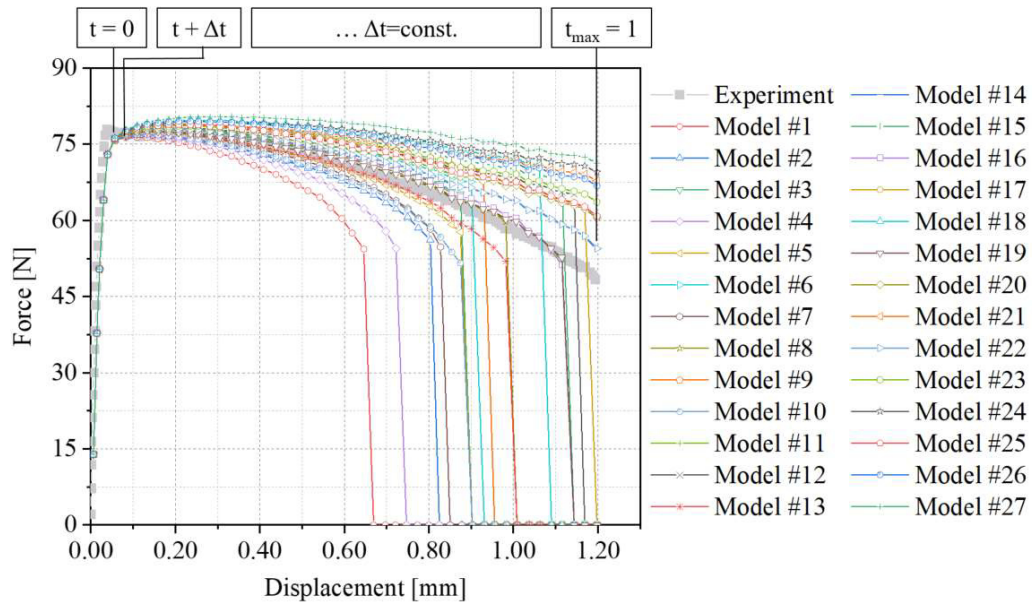
Table 5.2. ANN training database developed following a three level full factorial design

Numerical experiment	Ductile damage model parameters		
	Fracture locus		Regularization
	c_2 [-]	c_3 [-]	L [MPa]
Model #1	0.3	2.2	160.0
Model #2	0.5	2.2	160.0
Model #3	0.8	2.2	160.0
Model #4	0.3	2.2	180.0
Model #5	0.5	2.2	180.0
Model #6	0.8	2.2	180.0
Model #7	0.3	2.2	210.0
Model #8	0.5	2.2	210.0
Model #9	0.8	2.2	210.0
Model #10	0.3	2.5	160.0
Model #11	0.5	2.5	160.0
Model #12	0.8	2.5	160.0
Model #13	0.3	2.5	180.0
Model #14	0.5	2.5	180.0
Model #15	0.8	2.5	180.0
Model #16	0.3	2.5	210.0
Model #17	0.5	2.5	210.0
Model #18	0.8	2.5	210.0
Model #19	0.3	2.8	160.0
Model #20	0.5	2.8	160.0
Model #21	0.8	2.8	160.0
Model #22	0.3	2.8	180.0

Model #23	0.5	2.8	180.0
Model #24	0.8	2.8	180.0
Model #25	0.3	2.8	210.0
Model #26	0.5	2.8	210.0
Model #27	0.8	2.8	210.0

Postprocessing of the finite element simulations allows extracting the numerical results in terms of (a) images of the surface displacement fields in X and Y direction and (b) force values for the applied displacement. The extraction of both local (a) and global (b) data is done throughout the complete numerical experiment in equally spaced time increments, Δt . In this way, the information about the stress state evolution is taken into account. Local displacement field images are extracted from the nodes positioned in the zone of interest where the plastic strain develops, see Fig. 5.3a. Every single force value extracted at a specific time t (Fig. 5.3b) is assigned to the corresponding displacement image (Fig. 5.3a). The database constructed thereby is passed from the FE to the ANN model, whose architecture will be discussed in the next subchapter.





(b)

Fig. 5.3. Passing the training database from FE to ANN throughout the complete numerical experiment: (a) images of the local displacement field in X and Y direction (UX and UY) for every time step t, (b) global force-displacement curve values for every time step t.

The quality of the trained ANN model will be verified using the numerical experiments not contained in the training database, referred to as FE test cases. This verification is performed on FE test cases whose parameters are chosen to lie inside the design space shown in Fig. 5.2. The original design space is divided into 8 cubes as indicated by dashed blue lines in Fig. 2. The first set of parameter combinations is selected such that it covers the middle nodes of each of the 8 cubes (Table 5.3). The second set of parameters is selected following the Latin hypercube sampling, i.e. the points inside each of the 8 cubes are chosen randomly (Table 5.4).

Table 5.3. FE test cases covering the middle points of each of the 8 cubes

Numerical experiment	Ductile damage model parameters		
	Fracture locus		Regularization
	c_2 [-]	c_3 [-]	L [MPa]
FEM test #1	0.40	2.35	170.00
FEM test #2	0.65	2.35	170.00
FEM test #3	0.40	2.35	195.00
FEM test #4	0.65	2.35	195.00
FEM test #5	0.40	2.65	170.00
FEM test #6	0.65	2.65	170.00
FEM test #7	0.40	2.65	195.00
FEM test #8	0.65	2.65	195.00

Table 5.4. FE test cases selected according to the Latin hypercube sampling

Numerical experiment	Ductile damage model parameters		
	Fracture locus		Regularization
	c_2 [-]	c_3 [-]	L [MPa]
FEM test #9	0.32	2.43	161.63
FEM test #10	0.78	2.29	171.10
FEM test #11	0.50	2.48	184.81
FEM test #12	0.70	2.38	197.30
FEM test #13	0.31	2.50	170.33
FEM test #14	0.52	2.62	177.54
FEM test #15	0.43	2.52	200.76
FEM test #16	0.54	2.57	191.62

5.3.3 Artificial Neural Network (ANN) models

5.3.3.1 Model architectures and the building blocks

Three ANN structures are constructed and investigated based on the way the input information is processed to estimate the material parameters, see Fig. 5.4. In the architecture A the local displacement field images are used to estimate the material parameters $\{c_2, c_3\}$ while the parameter $\{L\}$ is estimated by using only the information inherent in the global force-displacement profile. For the architecture B, the opposite of architecture A is imposed, i.e. the parameters $\{c_2, c_3\}$ are learned from the force-displacement profile while $\{L\}$ is estimated from the displacement field images. For the architecture C all information, i.e. the features of the local displacement field images and the global force-displacement curves are used together to estimate the parameters $\{c_2, c_3, L\}$.

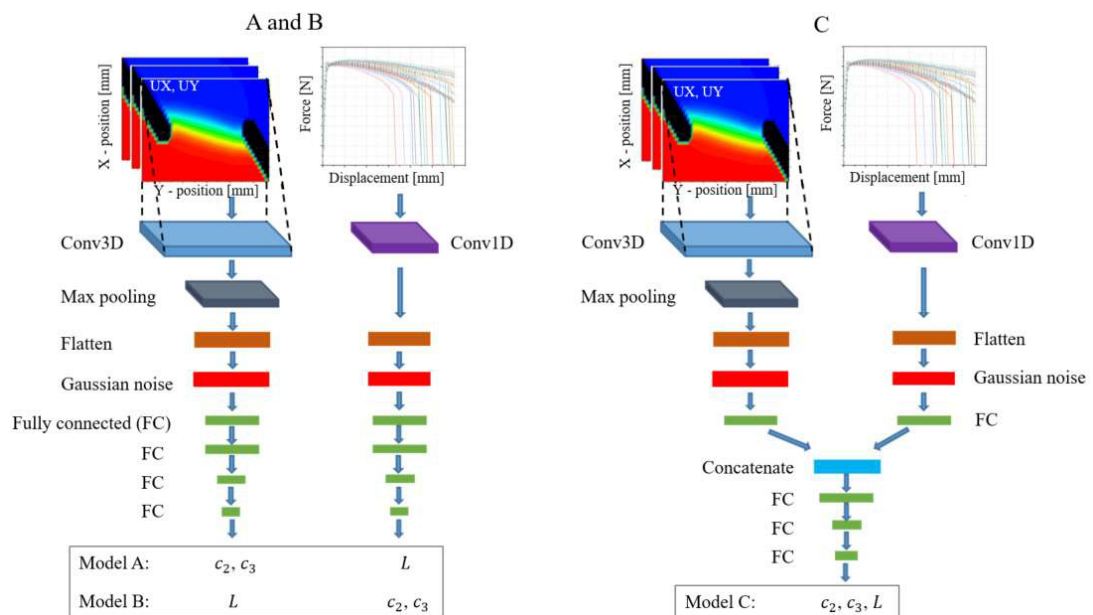


Fig. 5.4. Different ANN architectures studied: models A, B and C.

Since the input data for the ANNs contain images, we employ convolutional neural networks (CNN) because of their performance for translation invariant pattern recognition (in our case, the pattern to be recognized and characterized is the local strain concentration pattern). CNNs are capable of extracting high-level features hidden in the input data through their convolution layers and nonlinear activation functions. The convolutional layers are particularly suitable to exploit translation invariance in the input space. Therefore, all ANN architectures contain a convolution layer as a first layer for processing the input information. Furthermore, three-dimensional (3D) convolution layers are employed because the local displacement field images contain two space dimensions and one time dimension. The 3D convolution layers are capable of extracting features from both the spatial and temporal dimensions, which are necessary for capturing the motion information encoded in multiple adjacent frames (herein, those are data extractions on the force-displacement (FD) curve trajectory). One-dimensional convolutions are also applied on the FD history, which is a sequence of data in time. Similar to 3D convolutions, 1D convolutions are capable of extracting features from sequences of fixed length and mapping their internal features. The building blocks of the model structures shown in Fig. 5.4 are briefly described in the following.

In all models, after a 3D convolution layer a max pooling layer is added, which extracts the points with the largest value in the analysed local domain. Max pooling is a linear operation which reduces the dimension of the features extracted by a 3D convolution and also may prevent overfitting to a certain extent. At the other side, on the FD branch, after a 1D convolution no pooling layer is added because it is not necessary due to the small feature dimension. Afterwards, a flattening layer is applied to convert the feature data of the convolution layers into a single long feature vector. The structure and hierarchy of the selected layers in the CNN network follows a routine practice. For an in-depth discussion of the CNN networks, the reader is referred to (Stewart 2018; Kuo 2016).

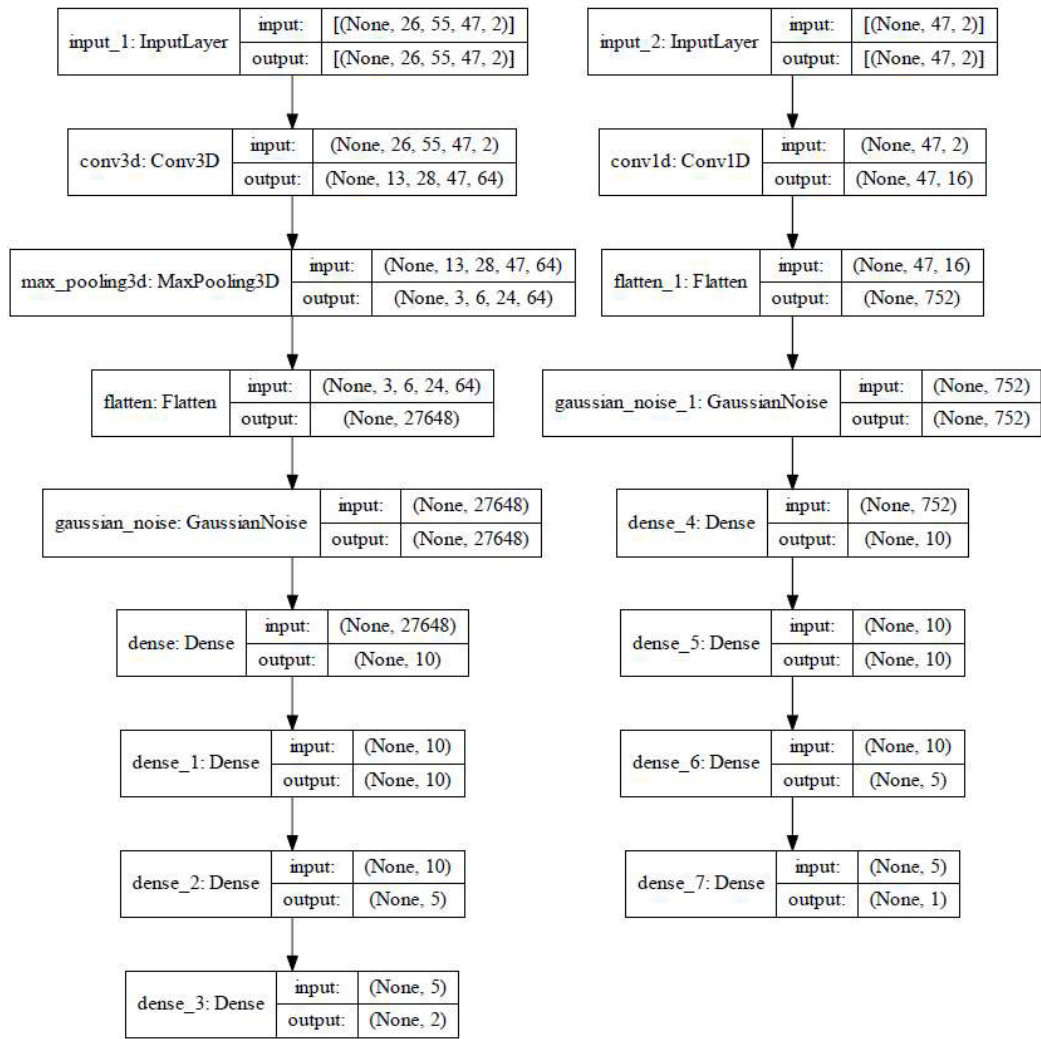
The training data are comprised of 27 FE models, see Table 5.2. Considering the size of the ANN networks, the optimization problem is very much prone to overfitting, which will result in deteriorated validation or test qualities. Therefore, two regularization approaches are considered and applied together to mitigate overfitting. The first one is an additive zero-centered Gaussian noise layer, with standard deviation of 0.05, which is positioned after the convolutional layers and can be regarded as random data augmentation. The effect of the Gaussian noise on the performance of CNNs has not been investigated systematically in the literature. However, it turned out to be very useful in achieving more generalizable trained models thereby even increasing the stability of the training stage. The other regularizer is applied through penalties on all layer kernels during optimization. For the latter, we apply an L2 regularization penalty with a regularization factor of 0.01. The penalty of the L2 regularizer is computed as

$$cost = l2 * \sum w^2 \quad (5.3)$$

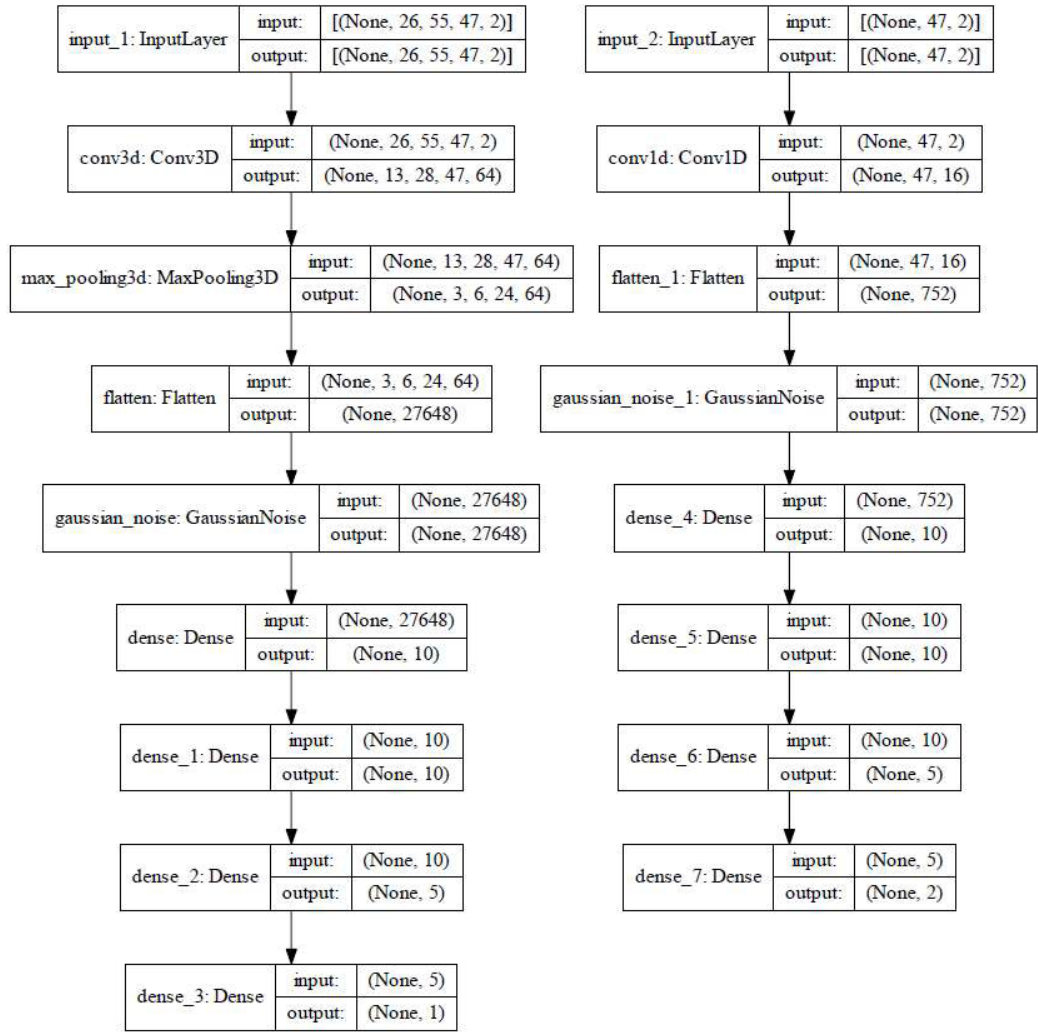
where w is a vector of layer weights and $l2 = 0.01$ is the regularization factor. This penalty prevents the weights of a network to grow very large and therefore helps to minimize overfitting of the training data. After a noise layer, fully connected (FC) layers are inserted in an inverted pyramidal stack (larger layers up and smaller layers at the bottom) to emphasize the importance of the information at higher levels (see Fig. 5.5 for detail information about the layer sizes). Note that in model C a concatenation layer is needed to merge two sources of extracted features to be forwarded to the next FC layers. The max pooling, Gaussian noise, flattening and concatenation layers have no training parameters. Therefore, the model architectures A, B and C are not only similar in structure but also very close in size, i.e. models A and B have 286,816 training parameters while model C has 286,751 (see Fig. 5.5).

In Fig. 5.5 the first dimension (None) corresponds to the batch size, which for the training data is equal to 27 and for verification data is equal to 16. For the 3D and 1D CNN, filter sizes of (3,3,2) and 2 are chosen, respectively. This selection was based on the sparse random exploration of a huge hyperparameter space. The sufficiency of the kernel size 3*3 is proven (see Baltic et al. 2021, Appendix). The spatial kernel size of 3*3 is a frequent choice as it adds more benefits like weight sharing and lowering the computational costs while taking into account information from the neighbouring pixels. The odd size of the filter (in spatial dimensions) is also beneficial because of the symmetry, i.e. all the previous layer pixels are symmetrical around the output pixel. Therefore, distortions typical for even sized kernels are avoided.

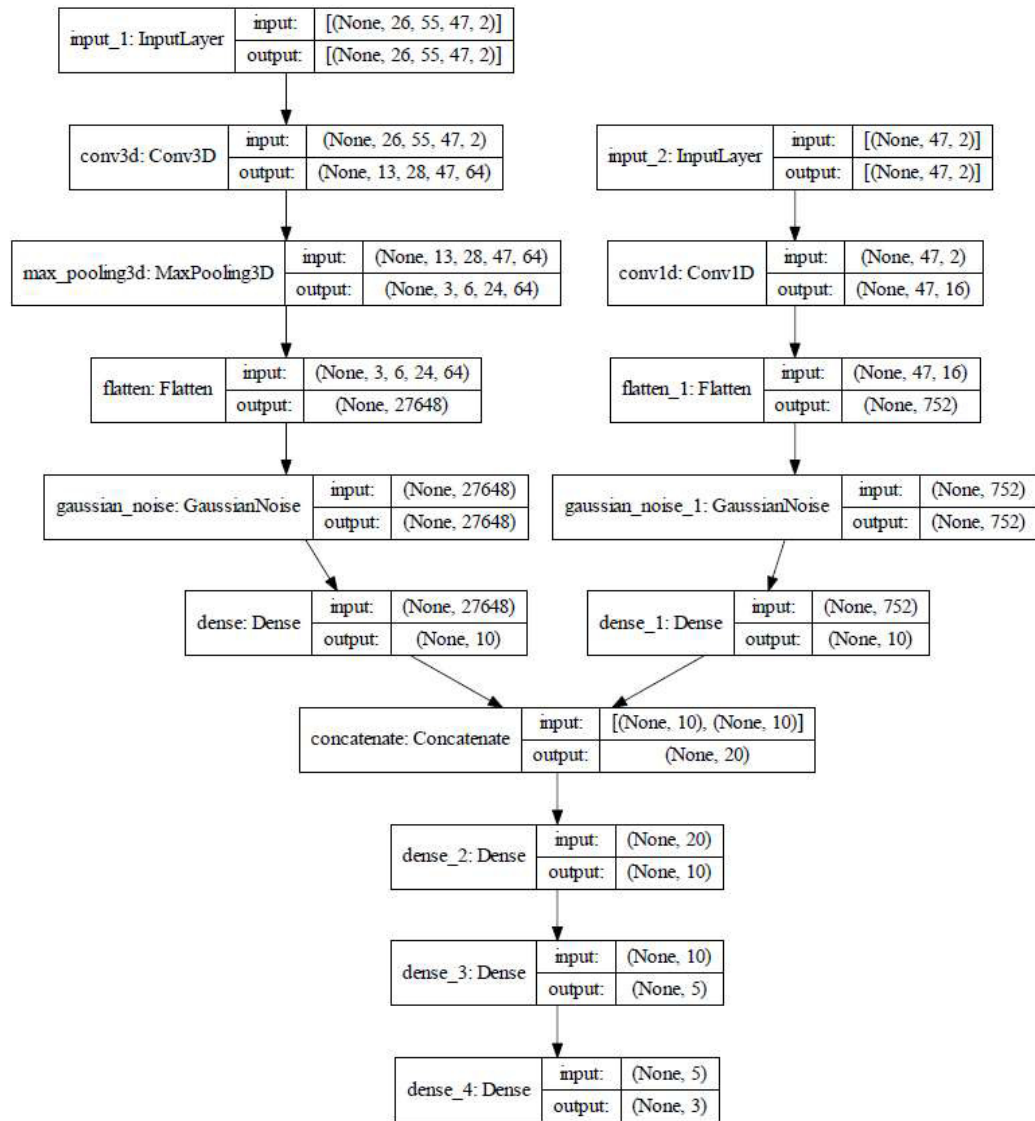
Note that these model structures do not have a large depth and width but still contain the main building blocks necessary for effective extraction of high-dimensional features from a small set of training examples. Usually, more CNN layers can potentially improve the accuracy of the ANN models. However, this depends on the choice of the architecture (deep or shallow) and depth and width of the training data set, as it has been explored in (Basha et al. 2019). According to (Basha et al. 2019), for the training datasets of size 27, a shallow model with more FC layers is the optimal choice for better performance. Indeed, we found that adding more CNN layers does not provide extra benefits while increasing computational costs. Here, the considered one CNN layer serves as a smart feature extractor both in space and time. Finding the optimum model architecture is not trivial. However, in the context of this work, the selected architecture designs perform well enough to demonstrate the applicability of the presented approach.



(a)



(b)



(c)

Fig. 5.5. Model summary of different ANN architectures: (a) model A, (b) model B, (c) model C.

5.3.3.2 Data preparation

Scale and distribution of the input and output data are very important for training the neural networks. Different scales may cause difficulties in training and modeling of the problem. This is because large input values may result in a model with extremely large neuron weights, thereby causing unstable learning and poor performance during generalization. Very large and different scales of output variables also often result in exploding gradients leading to a failing learning process or low model performance. Moreover, scaled training data always reduce the training time and lower the probability to fall into local minima.

In this work, the inputs (displacement field images and global FD curve) and outputs (material parameters) are normalized to the range of [0,1] with the linear transformation

$$X' = \frac{X - X_{min}}{X_{max} - X_{min}}, \quad (5.4)$$

where X and X' are the original and transformed data, respectively, and X_{min} and X_{max} correspond to the minimum and maximum value of X in the training data. The same minimum and maximum is used for normalization of the verification and experimental data.

5.3.3.3 Activation functions

In neural networks the nonlinearity to the output of a neuron is introduced via an activation function. The five most widely used activation functions are Sigmoid, Tanh, ReLU, Softplus and Gaussian. It is not trivial a priori which activation function works best for a given data set and problem. Sigmoid and Tanh are saturated non-linear activation functions and are widely used in traditional ANN models. They are given by Eq. (5.5) and Eq. (5.6), respectively:

$$f(x) = \frac{1}{1 + e^{-x}} \quad (5.5)$$

$$f(x) = \frac{e^x - e^{-x}}{e^x + e^{-x}} \quad (5.6)$$

As it is clear, the outputs of the Sigmoid are in the range (0,1) while the outputs of Tanh are in the range (-1,1). When the training data are scaled, there will be no problems with saturation which happens with large input values. For all layers in ANN structures in Fig. 5.4 Tanh is used except for the output layer, where Sigmoid activation is applied. Application of Sigmoid on the neurons of the last output layers imposes positivity of the material parameters $\{c_2, c_3, L\}$. Furthermore, even though the input data are scaled to (0,1) we find that Tanh is a better choice for the upper layers of the ANNs in Fig. 5.4: since the output of Tanh lies in the range (-1,1), the mean for the hidden layer is 0 or very close to it, which helps making the learning for next layer easier. Moreover, the Tanh activation function has larger derivatives compared to the Sigmoid, thereby making it more relevant for the gradient descent based optimization used in the error back propagation training algorithm. Although ReLU activation functions are nowadays very popular because they overcome vanishing gradients issues, in this work, since the considered ANN models are small, i.e. there are not so many hidden layers, the ReLU functions are not applied on the hidden layers.

5.3.3.4 Network optimization

The optimization of the training parameters of the ANN models is done by minimizing the sum of squared errors (SSE) of the estimated parameters $\{c_2, c_3, L\}$ for all training examples. The SSE is defined as

$$SSE = \sum_{i=1}^{27} (c'_{2i} - c_{2i})^2 + (c'_{3i} - c_{3i})^2 + (L'_{2i} - L_{2i})^2, \quad (5.7)$$

where $\{c'_2, c'_3, L'\}$ are the network output and $\{c_2, c_3, L\}$ are the true target parameters. Once the networks are fed by all training examples, the accumulated error is back-propagated to update the network weights and biases. The TensorFlow® software framework is used to train and optimize the networks (Abadi et al. 2015). With TensorFlow built-in operations back propagation based optimization can be done without the necessity to write complex program code. The Adam optimiser with a learning rate of 0.001 is used (Kingma and Ba 2014).

Every ANN model (A, B and C) is optimized 10 times with random initialization of its network parameters and maximum epoch number of 4000. We found this epoch number to be sufficient for the convergence of the optimization while still preventing the model to overfit the training data due to applied regularization approaches described in section 3.3.1. Then the average of 10 optimized model outputs is taken and considered as the final parameter estimate. With this strategy, we believe the prediction of material parameters is more accurate and robust for a highly nonlinear inverse problem as considered in this work.

5.3.4 Feeding the experimental data to the trained ANN

The results of the tensile test conducted on the shear specimen are provided to the trained ANN in the same format as the training database. Displacement field images in X and Y directions are generated from the DIC-measured displacement history (Fig. 5.6a). The force values measured during tensile testing are extracted over specified time increments Δt (Fig. 5.6b). For every single force value, the corresponding displacement image is provided. The experimental data extracted in this way is fed to the trained ANN model to find the set of parameters $\{c_2, c_3, L\}$ that models best the behavior of a real shear tension specimen.

When postprocessing the experimental data, different data arrangements have been generated in order to investigate potential effects of the ANN predictions. The influence of spatial discretization has been assessed by extracting the displacement images in different resolutions, Δp , defined as a distance between two nodes of the FE mesh for which the data has been provided. Fine and 2x coarser resolution have been considered, $\Delta p=0.0625$ mm and $\Delta p=0.125$ mm, respectively. The impact of the time discretization, i.e. the time step increment Δt , has been examined as well. Finer and coarser time discretizations have been investigated, i.e. $\Delta t=0.02$ and $\Delta t=0.05$.

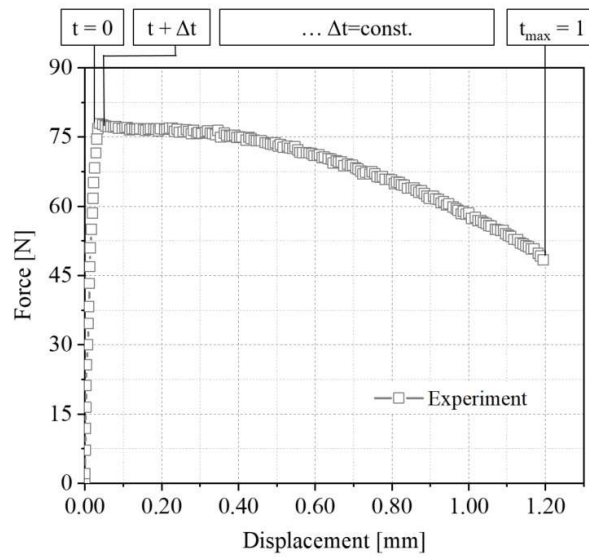
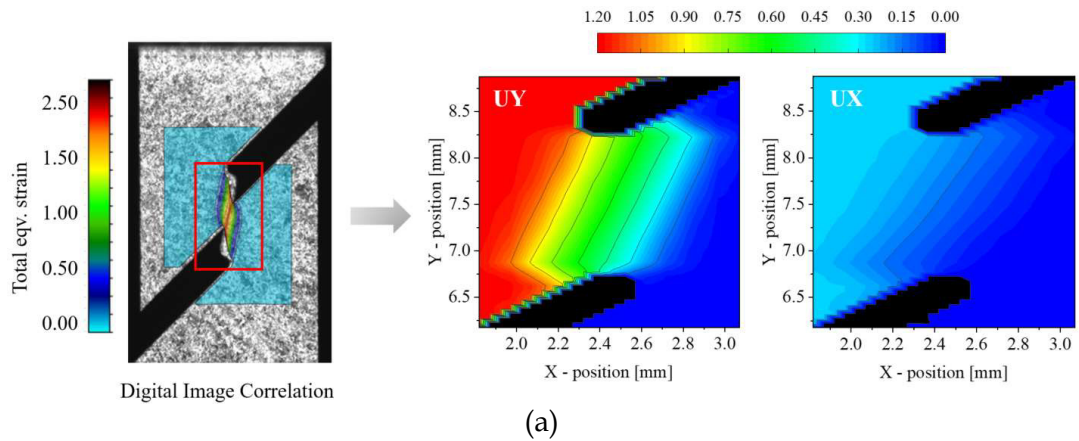
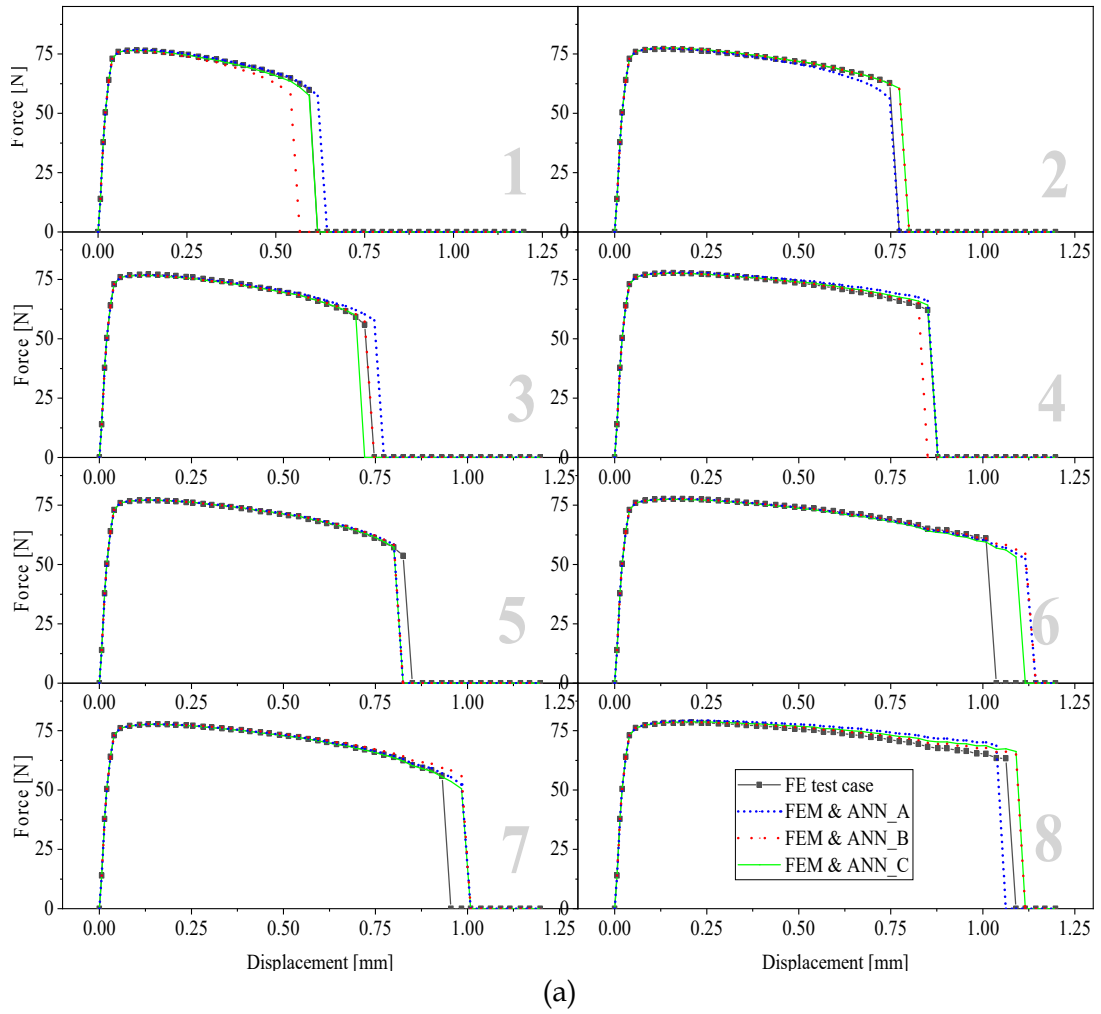


Fig. 5.6. Application of the trained ANN model: feeding the experimental data of the shear tension specimen into the trained ANN. (a) local displacement fields obtained from DIC analysis and (b) global force-displacement curve.

Delivering the displacement images using two different resolutions Δp has not shown any effect on the training quality. Therefore, the coarser resolution has been accepted (0.125 mm) for faster processing. On the other hand, the time discretization, i.e. the number of time steps for which the force displacement curve data is extracted and displacement images are attached, has turned out to have some impact on the training quality. Thus, more time steps, i.e. a smaller time step increment Δt (0.02) has been adopted.

5.4 Results and discussion

Before application on the real shear experiment, the quality of all three ANN architectures has been examined on four generated FE test cases unseen in the training stage. Numerical results (displacement field images and FD profiles) of those FE test cases are fed into the trained ANN models to estimate the material parameters used originally in the simulation (listed in Table 5.3. and Table 5.4.). The predicted parameters delivered by different ANN models are fed back to the FE simulation. The final model verification is based on the correct reproduction of the displacement field and FD history in the simulation with the estimated material parameters rather than merely judging the relative values of the estimated material parameters. This is because, due to the non-uniqueness of this highly nonlinear inverse problem, different parameter combinations may produce the same FD profile. Therefore, the prediction quality of the studied ANN model architectures for the FE test cases is shown in Fig. 5.7 by comparing the resulting FD profiles. Fig. 5.7a shows the predictions of the FE test cases covering the middle nodes of each of the 8 cubes. We observe that all ANN models studied (A, B and C) estimate sets of material parameters that reproduce the behavior of most of the test cases with satisfactory accuracy. Obviously, these three ANN architectures perform very similarly. Model B is slightly off for test case 1 though. For test case 6, all three architectures have similar deviation in displacement to fracture. Fig. 5.7b shows the predictions of the FE test cases designed according to Latin hypercube sampling. The performance of all different ANN architectures studies is similar again for all FE test cases, with the exemption of the FE test case 13 and 14, where the ANN model B results in a somewhat larger deviation compared to ANN architectures A and C. In the light of these results it is difficult to assess the preferred model architecture. Considering the complex material model exhibiting features such as material softening, all three models provide satisfactory results.



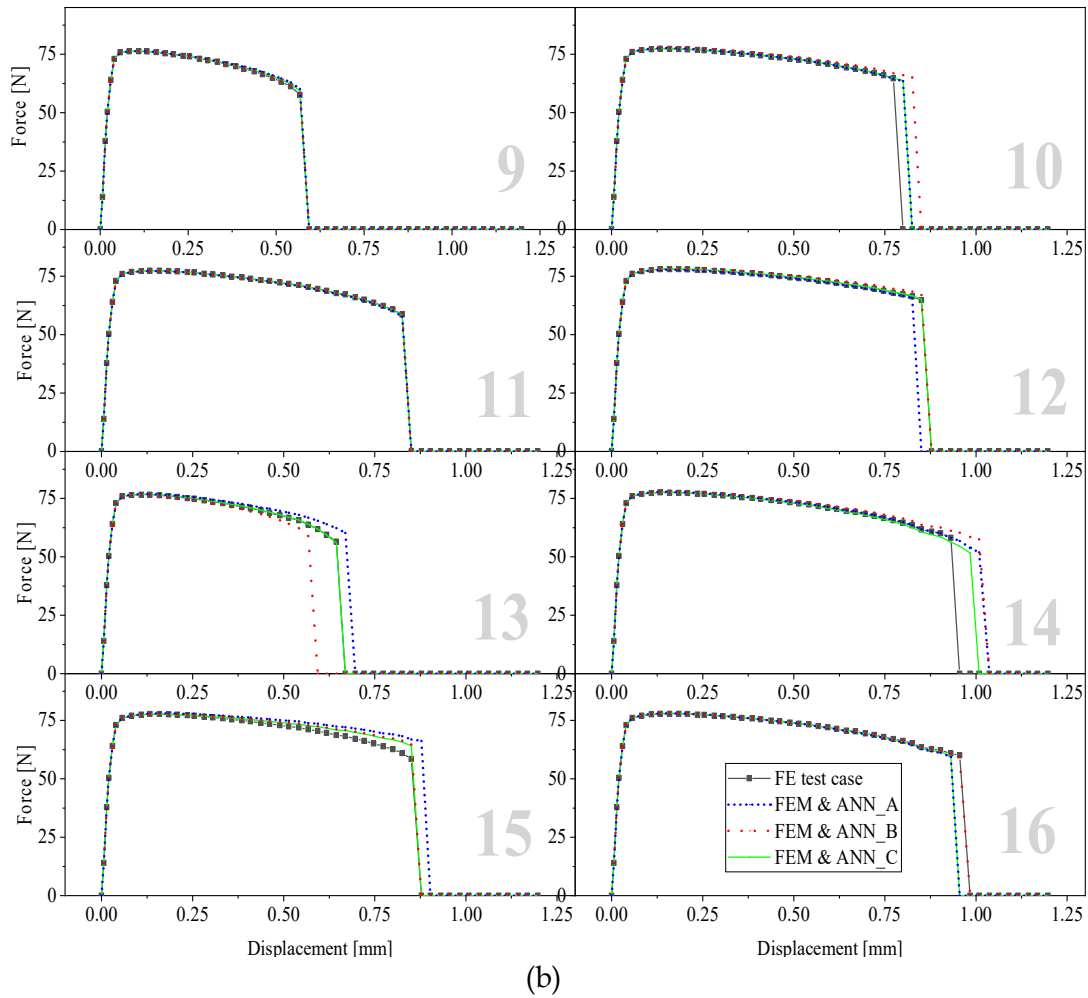
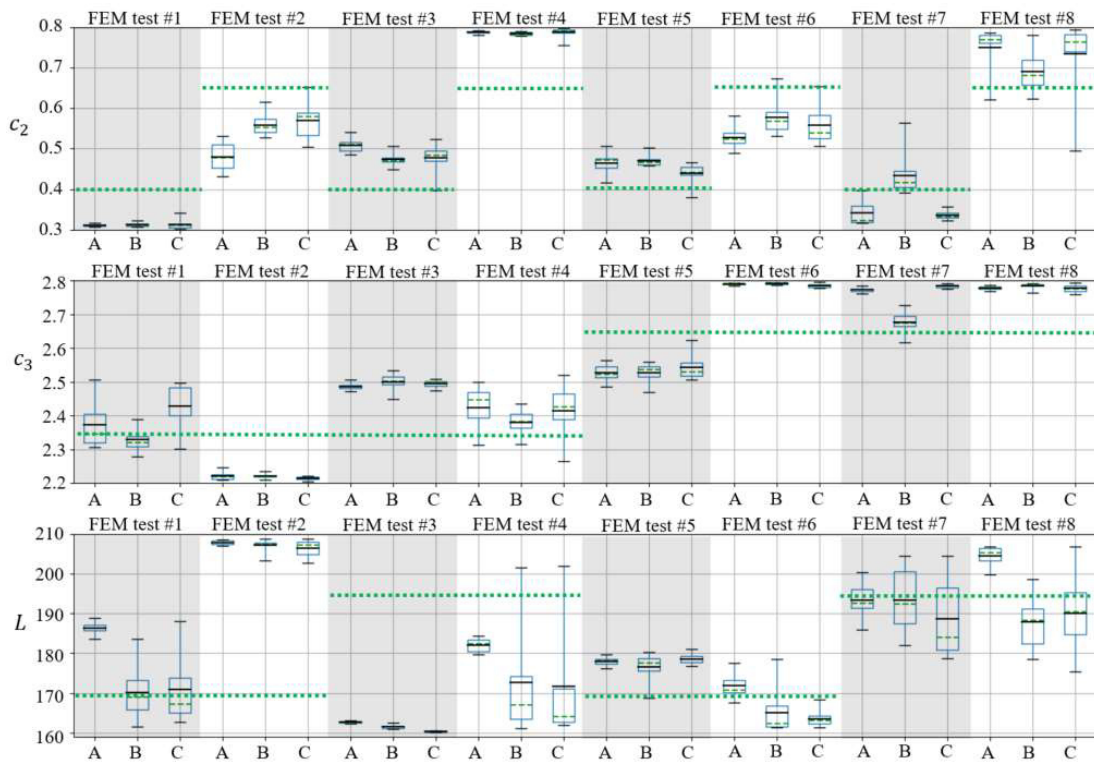


Fig. 5.7. Verification of the ANN models: results of the FE model predictions (FEM) for numerical test cases (FE test case) using parameter sets determined by different ANN architectures (ANN_A, ANN_B, ANN_C); the inserted numbers (1 - 8) on each individual graph represent the number of the FE test case; (a) results for the FE models covering the middle nodes of each of the 8 cubes; (b) results for the FE models designed according to the Latin hypercube sampling.

For better evaluation of the network outputs, Fig. 5.8 shows comparative statistics in box plots for the outcomes of 10 independent optimized ANN models on the verification dataset. Box plots visualize the distribution of numerical data and skewness through displaying the data quartiles, averages, medians and ranges. In Fig. 5.8, the whiskers, i.e. upper and lower vertical lines with the horizontal cap include the total range of the estimates, marking the minimum and maximum of the data. The lower and upper sides of the box correspond to the first and third quartiles, respectively; the dashed line in the box corresponds to the median of the data, whereas the average of the estimates is represented as a solid line. We observe that the overall ranges of the outcomes of all models overlap most of the time. Comparing

the median of each box for a given validation model of three ANN models, all architectures give results very close to each other, which reflects the fact that the models are very similar in terms of prediction quality. From the interquartile range, all models estimate the parameter c_3 in a somewhat more robust way than c_2 . Furthermore, for c_3 the median and average of outcomes coincide or are very close, which reflects the Gaussian distribution of the estimates. The true values, which were input for the FE generated test data are shown as green dotted lines.



(a)

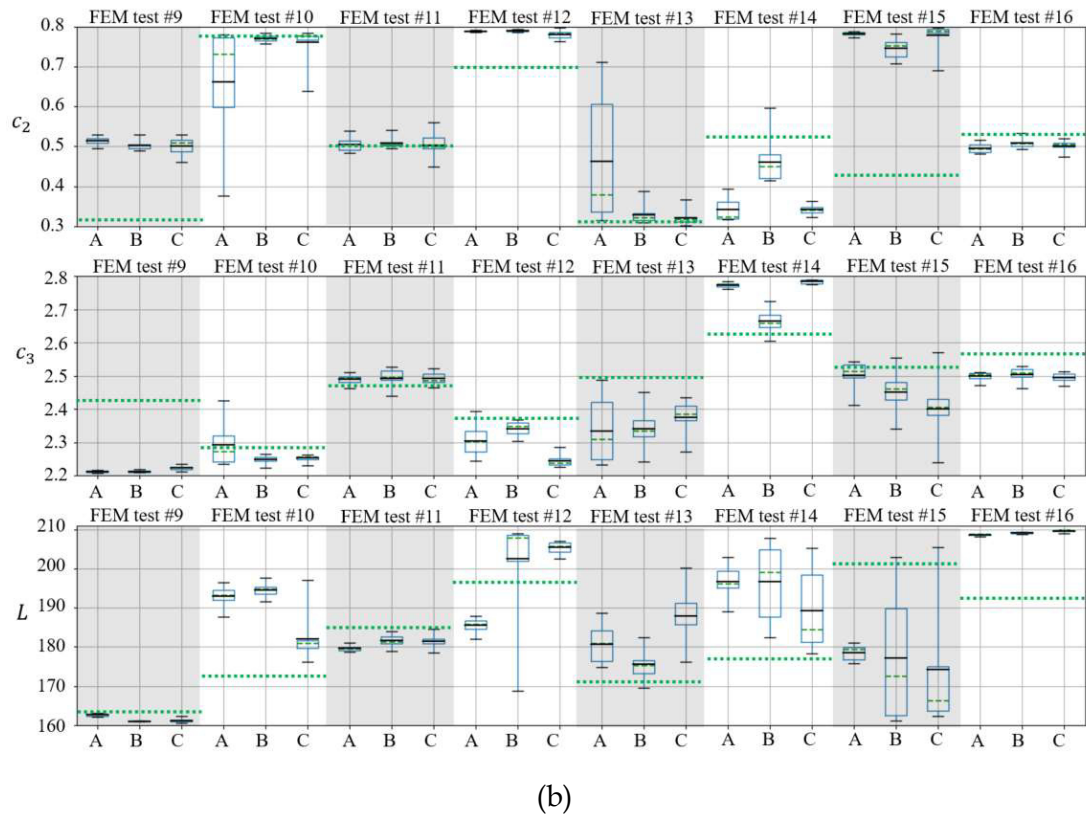


Fig. 5.8. Comparative statistics of different ANN network outputs on verification data. (a) FE models covering the middle nodes of each of the 8 cubes; (b) FE models designed according to the Latin hypercube sampling. The box plots show the statistics obtained by 10 independent optimization outcomes of the ANN and the green dotted lines show the true value, used in the FE model to generate the test data, for comparison.

Finally, comparing the true values of the material parameters of the verification models reported in Table 5.3, we observe that, although the interquartile range of the box plots rarely overlaps with the true values, the predicted parameters still produce the same numerical response (as shown in Fig. 5.7). Judging by the sensitivity analysis, small variations of the model parameters do not substantially change the FD curve and the displacement field. This inverse problem of estimating the material parameters is highly nonlinear, steep and complex, see Eq. (5.2). Therefore, it is possible to obtain different material parameters resulting in a comparable FD history and displacement field. Therefore, it is difficult to select the best model based on these verification models and exploratory data analysis. In fact, the results suggest that all models perform very similarly on the verification models with very small marginal differences.

However, the final validation of the ANN models has to be done on a real-world experiment. To this end, the data extracted from an experimental force-displacement curve and experimental displacement field images are fed into the trained ANN models. The predicted material parameter sets, averaged over the outcome of 10

independent optimized models, are shown in Table 5.5. Interestingly, we observe that models A and B predict the same parameters c_2 and c_3 , unlike the prediction of parameter L which shows a considerable difference. For comparison, Table 5.5 also shows the parameters formerly found by a classical experimental-numerical approach (Baltic et al. 2020a). Considering the complete set of parameters (c_2 , c_3 and L), it becomes apparent that only the ANN model A provides comparable set of parameters. The box plot of the outcomes is shown in 5.9. We observe that model B has a lower scatter in predicting the parameters. Again, it is difficult to select the model which performs best.

Table 5.5. Identified material parameters after feeding the experimental data of the shear tension specimen into ANN

ANN architecture	Ductile damage model parameters		
	Fracture locus		Regularization
	c_2 [-]	c_3 [-]	L [MPa]
ANN_A	0.4967915	2.7909071	164.575690
ANN_B	0.4620881	2.7928969	209.217671
ANN_C	0.3201537	2.6564574	208.712200
Experimental-numerical approach from (Baltic et al. 2020a)	0.5570000	2.4230000	167.125000

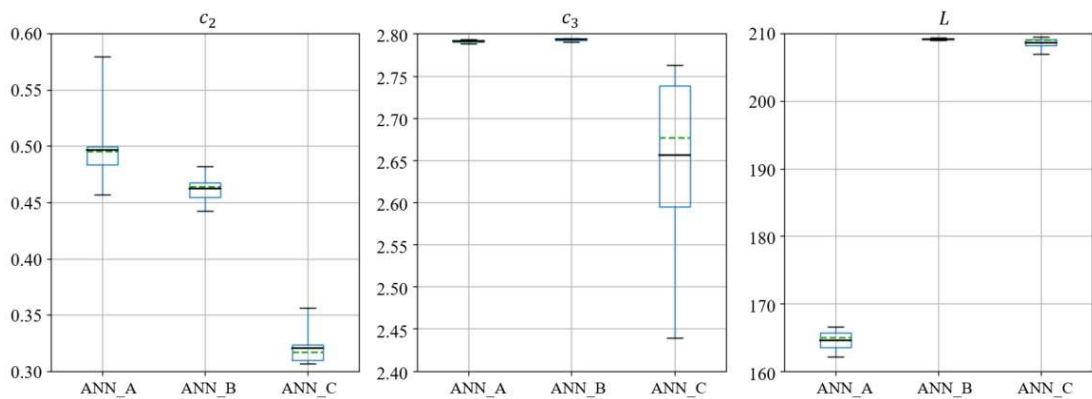


Fig. 5.9. Comparative statistics of different ANN network outputs on the experimental data.

The validation of the model prediction against experimental data is shown in Fig. 5.10. The parameter set provided by the ANN model A successfully predicts the force-displacement response recorded experimentally, yet with the fracture point predicted somewhat earlier than measured. On the other hand, the parameter set of the ANN model B predicts harder response than the experimental one. The last ANN architecture studied, C, leads to the most conservative prediction of fracture. These results reflect the high nonlinearity of the inverse problem and show that a small change in one parameter may result in a significantly different force-displacement response. Comparing the evolution of local mechanical fields in the experiment and

simulation Fig. 5.11, one can conclude that the progress of the strain upon loading is also well captured. This is expected because the information about the complete evolution of the local strain distribution has been accessible to the ANN in the training stage in the form of the full surface displacement field history that is fed into the ANN.

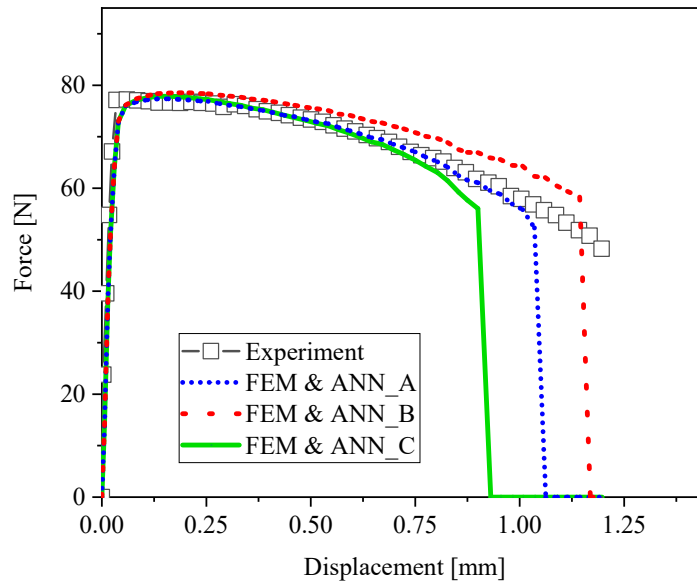


Fig. 5.10. Validation of the ANN model: FE model predictions of the experimental force displacement curves using material parameters determined by different ANN architectures (ANN_A, ANN_B, ANN_C).

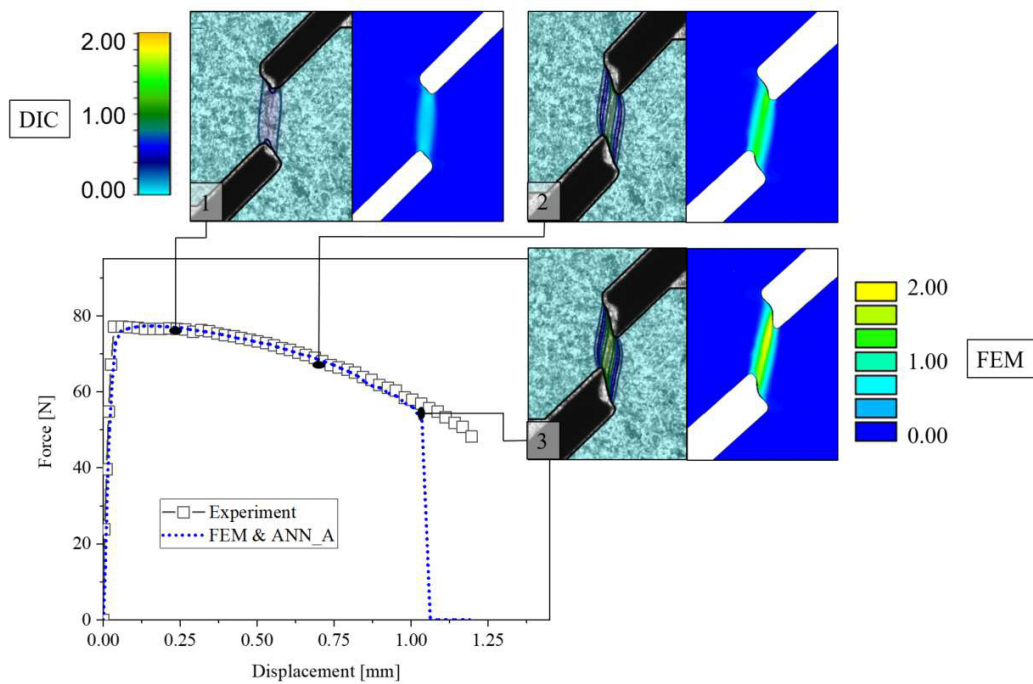


Fig. 5.11. Comparison of local equivalent total strain distributions documented experimentally using Digital Image Correlation (DIC) and calculated numerically (FEM) at three stages (1, 2 and 3). The FE simulation (FEM) shows the results using the set of parameters predicted by ANN model architecture A.

For a more general assessment of the parameter sets predicted by the ANN architectures studied, the parameters are validated for various samples not used in the training stage. The specimens specifically designed to cover various stress states in (Baltic et al. 2020a) are used for validation. Specimen geometries include notched samples ($R=1.00$ mm, $R=0.25$ mm), dogbone specimen (gauge width \times length = 2.00×5.00 mm) and shear specimen ($\alpha = 45^\circ$) (shear specimen with $\alpha = 0^\circ$ was used to generate the training database). Fig. 5.12 shows the force-displacement histories calculated for these specimens by the set of material parameters obtained from ANN architectures A, B and C. In Fig. 5.12, the specimens are referred to according to the list of abbreviations given in Table 5.6. While the numerical results are mainly following the experimental data, a somewhat larger deviation for one particular geometry (shear45) is attributed to excessive stress triaxiality influence stemming from overestimated c_2 value. Nevertheless, considering that this prediction quality is achieved using only one single specimen for the complete calibration process, the overall agreement for all specimens is satisfactory.

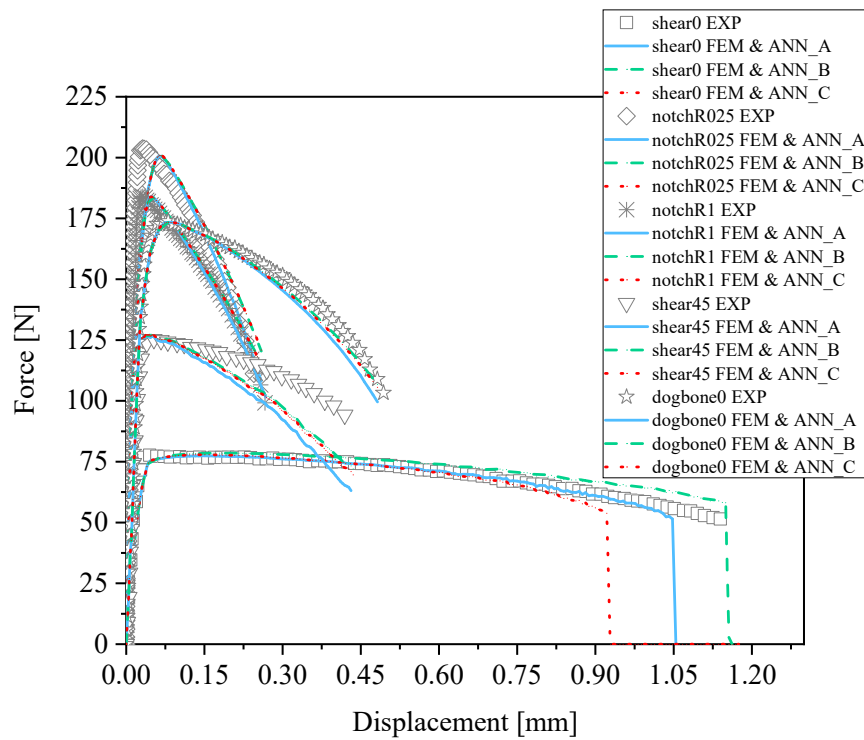


Fig. 5.12. Comparison of numerically predicted force-displacement curves using the set of parameters given by ANN model A for multiple geometries covering various stress states. The experimental data is taken from (Baltic et al. 2020a).

Table 5.6. List of abbreviations

Abbreviation	Explanation
notchR025	Notched tension specimen with radius of the notch R=0.25 mm
notchR1	Notched tension specimen with radius of the notch R=1.00 mm
shear0	Shear tension specimen with angle $\alpha=0^\circ$ (see (Baltic et al. 2020a))
shear45	Shear tension specimen with angle $\alpha=45^\circ$ (see (Baltic et al. 2020a))
dogbone	Conventional dogbone tension specimen
EXP	Experimental result
SIM	Simulation result

5.5 Summary and conclusion

ANN assisted fracture locus calibration has been studied in this work for the first time as a promising alternative to the experimental-numerical calibration strategy followed in e.g. (Baltic et al. 2020a). The article demonstrates the procedure of including the evolution of both local and global features, i.e. displacement images and force-displacement curve of the material observed in the experiment, into the training of the neural network. Application of artificial intelligence using a so-trained neural network provides accurate predictions of ductile fracture on the local and global levels, as the reported results suggest. The new methodology allows extracting the model parameters from a single sample geometry as opposed to the many sample geometries typically required to establish a ductile fracture locus. The original contributions of the presented work are twofold, stemming from the ductile fracture modeling and machine learning aspects:

- The computational framework developed supports the determination of the ductile fracture locus in such a way that the knowledge of a relevant loading path in the course of deformation is no longer mandatory for model calibration, i.e. the calibration does not rely on the strategy of averaging the stress state variables along the loading path any longer. Since it was found that the fracture locus for proportional loadings differs substantially from the one for nonproportional ones (Benzerga et al. 2012; Basu and Benzerga 2015), bypassing the averaging of the fracture paths appears as a great improvement, particularly in view of the application to prestrained materials prone to strain localization, where proportional loadings are impossible to achieve in the experiment. Furthermore, the ambiguity of the choice of a critical element to be selected in the numerical model for the extraction of the respective loading path is thereby also circumvented.
- The verification results of differently structured artificial neural networks suggest that, no matter which of these three ANN structures is chosen, it is possible to estimate realistic material parameters. Nevertheless, the preference is given to the physics informed partitioning of the ANN architecture over brute force application of ANNs. It is suggested to include prior physical

knowledge regarding the material model concerned, particularly when large training data sets are not available and experimental data is limited, as it is usually the case in material modeling. This work has shown that despite limited data and thus small size of the ANN, it is possible to calibrate the material parameters and achieve realistic results in structural computations.

Our observations suggest that a single sample geometry is sufficient to extract the constants determining the material's hardening or rather softening law. It is essential that the sample experiences a variety of different stress states in different positions upon plastic deformation. Key to success is found to be in making use of this valuable information in the model calibration. Further research should provide a more general proof involving different sample geometries and different materials. This work is a first step towards a fully automatic material parameter determination from simple tensile tests, using the evolution of local and global features as an input.

Acknowledgements

The author gratefully acknowledges the financial support under the scope of the COMET program within the K2 Center "Integrated Computational Material, Process and Product Engineering (IC-MPPE)" (Project No 859480). This program is supported by the Austrian Federal Ministries for Climate Action, Environment, Energy, Mobility, Innovation and Technology (BMK) and for Digital and Economic Affairs (BMDW), represented by the Austrian research funding association (FFG), and the federal states of Styria, Upper Austria and Tyrol. TDK Electronics is thanked for providing the material.

Chapter 6

Summary

A modeling strategy to describe the damage and fracture of a thin-walled structure made of a ductile material was developed in this thesis. Various fracture mechanisms were well explained by a unique damage plasticity model. Key to success in modeling different material responses under different regimes was found to be the local fracture strain theory i.e. a three-dimensional fracture locus with its associated length scale, coupled to metal plasticity. Following the physical aspects of a ductile fracture process, the model featuring a stress state dependent damaging process was proposed, resulting in a true stress-strain response dependent on the history of the stress state variables. A new definition of a length scale with a clear physical meaning was introduced and considered in the numerical model, ensuring thus the fracture predictions to be independent of the scale of the experimentally determined fracture strain.

The modeling approach was first validated on uncracked structures where the aim was to predict the onset of fracture. Different plastic responses of tension samples experiencing a wide range of stress states were captured by modeling the softening process dependent on the loading path to fracture. Furthermore, a numerical analysis of the failure scenario in a real world structure was performed whose instant of failure was successfully predicted by the material model calibrated independently of the loading conditions occurring in the component.

The concept was further examined on pre-cracked structures aiming to predict the experimentally observed crack propagation. As this could also be accomplished without any adjustments of the model calibrated for uncracked specimens, there is some fundamental generality of the concept relying on the local stress state dependent fracture strain. This is, however, valid only if the fracture strains are considered together with their associated length scale, i.e. the length over which the experimental strains are averaged.

Furthermore, a step forward in determining the model parameters was taken by taking advantage of a machine learning algorithm as a promising alternative to classical inverse methods. This facilitates the practical usage of the model and

broadens the range of applications. Generally, the work paves the way for modeling demanding strain-hardened materials and sheet-metal structures exposed to complex loading histories.

Bibliography

- Abadi, M.; Agarwal, A.; Barham, P.; Brevdo, E.; Chen, Z.; Citro, C. et al. (2015): TensorFlow : Large-Scale Machine Learning on Heterogeneous Distributed Systems.
- Abbassi, F.; Belhadj, T.; Mistou, S.; Zghal, A. (2013): Parameter identification of a mechanical ductile damage using Artificial Neural Networks in sheet metal forming. In: *Materials & Design* 45, S. 605–615. DOI: 10.1016/j.matdes.2012.09.032.
- Abendroth, M.; Kuna, M. (2003): Determination of deformation and failure properties of ductile materials by means of the small punch test and neural networks. In: *Computational Materials Science* 28, S. 633–644. DOI: 10.1016/j.commatsci.2003.08.031.
- Abendroth, M.; Kuna, M. (2006): Identification of ductile damage and fracture parameters from the small punch test using neural networks. In: *Engineering Fracture Mechanics* 73 (6), S. 710–725. DOI: 10.1016/j.engfracmech.2005.10.007.
- Aguir, H.; Marouani, H. (2010): Gurson-Tvergaard-Needleman parameters identification using artificial neural networks in sheet metal blanking. In: *Int J Mater Form* 3, S. 113–116. DOI: 10.1007/s12289-010-0720-5.
- Anand, L.; Aslan, O.; Chester, S. A. (2012): A large-deformation gradient theory for elastic–plastic materials. Strain softening and regularization of shear bands. In: *International Journal of Plasticity* 30–31, S. 116–143. DOI: 10.1016/j.ijplas.2011.10.002.
- ANSYS Documentation (Hg.): <https://ansyshelp.ansys.com/>.
- Aslan, O.; Cordero, N. M.; Gaubert, A.; Forest, S. (2011): Micromorphic approach to single crystal plasticity and damage. In: *International Journal of Engineering Science* 49 (12), S. 1311–1325. DOI: 10.1016/j.ijengsci.2011.03.008.
- Bai, Y. (2008): Effect of Loading History on Necking and Fracture. Massachusetts Institute of Technology.
- Bai, Y.; Wierzbicki, T. (2008): A new model of metal plasticity and fracture with pressure and Lode dependence. In: *International Journal of Plasticity* 24 (6), S. 1071–1096. DOI: 10.1016/j.ijplas.2007.09.004.
- Bai, Y.; Wierzbicki, T. (2015): A comparative study of three groups of ductile fracture loci in the 3D space. In: *Engineering Fracture Mechanics* 135, S. 147–167. DOI: 10.1016/j.engfracmech.2014.12.023.

- Baltic, S.; Asadzadeh, M. Z.; Hammer, P.; Magnien, J.; Gänser, H.-P.; Antretter, T.; Hammer, R. (2021): Machine learning assisted calibration of a ductile fracture locus model. In: *Materials & Design* 203, S. 109604. DOI: 10.1016/j.matdes.2021.109604.
- Baltic, S.; Magnien, J.; Gänser, H.-P.; Antretter, T.; Hammer, R. (2020a): Coupled damage variable based on fracture locus: Modelling and calibration. In: *International Journal of Plasticity* 126, S. 102623. DOI: 10.1016/j.ijplas.2019.11.002.
- Baltic, S.; Magnien, J.; Gänser, H.-P.; Antretter, T.; Hammer, R. (2020b): Coupled damage variable based on fracture locus: Prediction of ductile failure in a complex structure. In: *International Journal of Solids and Structures* 207, S. 132–144. DOI: 10.1016/j.ijsolstr.2020.10.018.
- Bao, Y.; Wierzbicki, T. (2004): On fracture locus in the equivalent strain and stress triaxiality space. In: *International Journal of Mechanical Sciences* 46 (1), S. 81–98. DOI: 10.1016/j.ijmecsci.2004.02.006.
- Bao, Yingbin; Wierzbicki, Tomasz (2005): On the cut-off value of negative triaxiality for fracture. In: *Engineering Fracture Mechanics* 72 (7), S. 1049–1069. DOI: 10.1016/j.engfracmech.2004.07.011.
- Barlat, F.; Aretz, H.; Yoon, J. W.; Karabin, M. E.; Brem, J. C.; Dick, R. E. (2005): Linear transformation-based anisotropic yield functions. In: *International Journal of Plasticity* 21 (5), S. 1009–1039. DOI: 10.1016/j.ijplas.2004.06.004.
- Barsoum, Imad; Faleskog, Jonas (2011): Micromechanical analysis on the influence of the Lode parameter on void growth and coalescence. In: *International Journal of Solids and Structures* 48 (6), S. 925–938. DOI: 10.1016/j.ijsolstr.2010.11.028.
- Basaran, M.; Wölkerling, S. D.; Feucht, M.; Neukamm, F.; Weichert, D. (Hg.) (2010): An Extension of the GISSMO Damage Model based on Lode Angle Dependence. Bamberg. 9th LS-DYNA anwenderforum.
- Basha, S. S.; Dubey, S. R.; Pulabaigari, V.; Mukherjee, S. (2019): Impact of Fully Connected Layers on Performance of Convolutional Neural Networks for Image Classification. In: *Neurocomputing* 378. DOI: 10.1016/j.neucom.2019.10.008.
- Basu, S.; Benzerga, A. A. (2015): On the path-dependence of the fracture locus in ductile materials. Experiments. In: *International Journal of Solids and Structures* 71, S. 79–90. DOI: 10.1016/j.ijsolstr.2015.06.003.
- Bathe, K. J. (1996): *Finite Element Procedures*: Prentice-Hall.
- Beese, A. M.; Luo, M.; Li, Y.; Bai, Y.; Wierzbicki, T. (2010): Partially coupled anisotropic fracture model for aluminum sheets. In: *Engineering Fracture Mechanics* 77 (7), S. 1128–1152. DOI: 10.1016/j.engfracmech.2010.02.024.
- Belytschko, T.; Bazant, Z. P.; Yul-Woong, H.; Ta-Peng, C. (1986): Strain-softening materials and finite-element solutions. In: *Computers and Structures* Vol. 23, No. 2., 163–180.

Benzerga, A.; Leblond, J.-B.; Needleman, A.; Tvergaard, V. (2016): Ductile failure modeling. In: *Int J Fract* 201. DOI: 10.1007/s10704-016-0142-6.

Benzerga, A.; Surovik, D.; Keralavarma, S. (2012): On the path-dependence of the fracture locus in ductile materials – Analysis. In: *International Journal of Plasticity* 37, S. 157–170. DOI: 10.1016/j.ijplas.2012.05.003.

Besson, J. (2009): Continuum Models of Ductile Fracture: A Review. In: *International Journal of Damage Mechanics* 19 (1), S. 3–52. DOI: 10.1177/1056789509103482.

Bonet, J.; Wood, R. D. (1997): Nonlinear continuum mechanics for finite element analysis: Cambridge University Press.

Bouchard, Pierre-Olivier; Gachet, Jean-Marie; Roux, Emile (2011): Ductile damage parameters identification for cold metal forming applications 1353, S. 47–52. DOI: 10.1063/1.3589490.

Box, G. E. P.; Behnken, D. W. (1960): Some New Three Level Designs for the Study of Quantitative Variables. In: *Technometrics* 2 (4), S. 455–475. DOI: 10.1080/00401706.1960.10489912.

Boyce, B. L.; Kramer, S. L. B.; Bosiljevac, T. R.; Corona, E.; Moore, J. A.; Elkhodary, K. et al. (2016): The second Sandia Fracture Challenge: predictions of ductile failure under quasi-static and moderate-rate dynamic loading. In: *Int J Fract* 198 (1), S. 5–100. DOI: 10.1007/s10704-016-0089-7.

Boyce, B. L.; Kramer, S. L. B.; Fang, H. E.; Cordova, T. E.; Neilsen, M. K.; Dion, K. et al. (2014): The Sandia Fracture Challenge: blind round robin predictions of ductile tearing. In: *Int J Fract* 186 (1), S. 5–68. DOI: 10.1007/s10704-013-9904-6.

Bridgman, P. W. (1952): Studies in Large Plastic Flow and Fracture. 115 Bände.

Brüinig, Michael; Chyra, Oliver; Albrecht, Daniel; Driemeier, Larissa; Alves, Marcílio (2008): A ductile damage criterion at various stress triaxialities. In: *International Journal of Plasticity* 24 (10), S. 1731–1755. DOI: 10.1016/j.ijplas.2007.12.001.

Brüinig, Michael; Gerke, Steffen; Schmidt, Marco (2017): Damage and failure at negative stress triaxialities: Experiments, modeling and numerical simulations. In: *International Journal of Plasticity* 102. DOI: 10.1016/j.ijplas.2017.12.003.

Cao, T.-S.; Bobadilla, C.; Montmitonnet, P.; Bouchard, P.-O. (2015): A comparative study of three ductile damage approaches for fracture prediction in cold forming processes. In: *Journal of Materials Processing Technology* 216, S. 385–404. DOI: 10.1016/j.jmatprotec.2014.10.009.

Cao, T.-S.; Gachet, J.-M.; Montmitonnet, P.; Bouchard, P.-O. (2014): A Lode-dependent enhanced Lemaitre model for ductile fracture prediction at low stress triaxiality. In: *Engineering Fracture Mechanics* 124-125, S. 80–96. DOI: 10.1016/j.engfracmech.2014.03.021.

Chen, Dongdong; Sun, Guangyong; Meng, Maozhou; Li, Guangyao; Li, Qing (2018a): Residual crashworthiness of CFRP structures with pre-impact damage – An

experimental and numerical study. In: *International Journal of Mechanical Sciences* 149, S. 122–135. DOI: 10.1016/j.ijmecsci.2018.08.030.

Chen, Kelin; Scales, Martin; Kyriakides, Stelios (2018b): Material hardening of a high ductility aluminum alloy from a bulge test. In: *International Journal of Mechanical Sciences* 138-139, S. 476–488. DOI: 10.1016/j.ijmecsci.2018.02.002.

Cheng, C.; Meng, B.; Han, J. Q.; Wan, M.; Wu, X. D.; Zhao, R. (2017): A modified Lou-Huh model for characterization of ductile fracture of DP590 sheet. In: *Materials & Design* 118, S. 89–98. DOI: 10.1016/j.matdes.2017.01.030.

Cockcroft, M. G.; Latham, D. J. (1968): Ductility and the Workability of Metals. In: *Journal Institute of Metals* Vol. 96, pp. 33-39.

Coppieters, S.; Cooreman, S.; Sol, H.; van Houtte, P.; Debruyne, D. (2011): Identification of the post-necking hardening behaviour of sheet metal by comparison of the internal and external work in the necking zone. In: *Journal of Materials Processing Technology* 211 (3), S. 545–552. DOI: 10.1016/j.jmatprotec.2010.11.015.

Datsko, J. (1966): *Material Properties and Manufacturing Processes*. New York: John Wiley & Sons Inc.

Deole, A. D.; Barnett, M. R.; Weiss, M. (2018): The numerical prediction of ductile fracture of martensitic steel in roll forming. In: *International Journal of Solids and Structures* 144-145, S. 20–31. DOI: 10.1016/j.ijsolstr.2018.04.011.

Driemeier, L.; Moura, R. T.; Machado, I. F.; Alves, M. (2015): A bifailure specimen for accessing failure criteria performance. In: *International Journal of Plasticity* 71, S. 62–86. DOI: 10.1016/j.ijplas.2015.02.013.

Driemeier, Larissa; Brünig, Michael; Micheli, Giancarlo; Alves, Marcílio (2010): Experiments on stress-triaxiality dependence of material behavior of aluminum alloys. In: *Mechanics of Materials* 42 (2), S. 207–217. DOI: 10.1016/j.mechmat.2009.11.012.

Dunand, M.; Mohr, D. (2010): Hybrid experimental–numerical analysis of basic ductile fracture experiments for sheet metals. In: *International Journal of Solids and Structures* 47 (9), S. 1130–1143. DOI: 10.1016/j.ijsolstr.2009.12.011.

Dunand, Matthieu; Mohr, Dirk (2011): Optimized butterfly specimen for the fracture testing of sheet materials under combined normal and shear loading. In: *Engineering Fracture Mechanics* 78 (17), S. 2919–2934. DOI: 10.1016/j.engfracmech.2011.08.008.

Engelen, R.; Geers, M.; Baaijens, F. (2003): Nonlocal implicit gradient-enhanced elasto-plasticity for the modelling of softening behavior. In: *International Journal of Plasticity* 19, S. 403–433. DOI: 10.1016/S0749-6419(01)00042-0.

Fischer, F. D.; Kolednik, O.; Shan, G. X.; Rammerstorfer, F. G. (1995): A note on calibration of ductile failure damage indicators. In: *Int J Fract* 73 (4), S. 345–357. DOI: 10.1007/BF00027274.

- Forest, S. (2009): Micromorphic Approach for Gradient Elasticity, Viscoplasticity, and Damage. In: *Journal of Engineering Mechanics* 135 (3), S. 117–131. DOI: 10.1061/(ASCE)0733-9399(2009)135:3(117).
- Freudenthal, A. M. (1950): The inelastic behaviour of engineering materials and structures. New York: John Wiley & Sons Inc.
- Gänsler, H.-P.; Atkins, A. G.; Kolednik, O.; Fischer, F. D.; Richard, O. (2000): Upsetting of Cylinders: A Comparison of Two Different Damage Indicators. In: *materialstechnology* 123 (1), S. 94–99. DOI: 10.1115/1.1286186.
- Gänsler H.P.; Atkins A.G.; Kolednik O.; Fischer, F. D.; Richard O. (2001): Upsetting of Cylinders: A Comparison of Two Different Damage Indicators. In: *Journal of Engineering Materials and Technology*, zuletzt geprüft am 30.10.2018.
- Gao, X.; Zhang, T.; Zhou, J.; Graham, S. M.; Hayden, M.; Roe, C. (2011): On stress-state dependent plasticity modeling. Significance of the hydrostatic stress, the third invariant of stress deviator and the non-associated flow rule. In: *International Journal of Plasticity* 27 (2), S. 217–231. DOI: 10.1016/j.ijplas.2010.05.004.
- Gao, Xiaosheng; Zhang, Guihua; Roe, Charles (2010): A Study on the Effect of the Stress State on Ductile Fracture. In: *International Journal of Damage Mechanics* 19, S. 75–94. DOI: 10.1177/1056789509101917.
- Giagmouris, T.; Kyriakides, S.; Korkolis, Y. P.; Lee, L.-H. (2010): On the localization and failure in aluminum shells due to crushing induced bending and tension. In: *International Journal of Solids and Structures* 47 (20), S. 2680–2692. DOI: 10.1016/j.ijsolstr.2010.05.023.
- Gurson, A. L. (1977): Continuum Theory of Ductile Rupture by Void Nucleation and Growth: Part I – Yield Criteria and Flow Rules for Porous Ductile Media. In: *materialstechnology* 99 (1), S. 2–15. DOI: 10.1115/1.3443401.
- H. W. Swift (1952): Plastic Instability under Plane Stress. In: *Journal of the Mechanics and Physics of Solids* 1, S. 1–18.
- Ha, J.; Baral, M.; Korkolis, Y. (2018): Plastic anisotropy and ductile fracture of bake-hardened AA6013 aluminum sheet. In: *International Journal of Solids and Structures*. DOI: 10.1016/j.ijsolstr.2018.07.015.
- Hancock, J. W.; Mackenzie, A. C. (1976): On the mechanisms of ductile failure in high-strength steels subjected to multi-axial stress-states. In: *Journal of the Mechanics and Physics of Solids* 24 (2-3), S. 147–160. DOI: 10.1016/0022-5096(76)90024-7.
- Haufe, A.; Neukamm, F.; Feucht, M.; DuBois, P.; Borvall, T. (Hg.) (2010): A Comparison of recent Damage and Failure Models for Steel Materials in Crashworthiness Application in LS-DYNA. 11th International LS-DYNA Users Conference. Dearborn, MI, USA, June 6-8.
- Hershey, A. V. (1954): The plasticity of an isotropic aggregate of anisotropic face centred cubic crystals. In: *Journal of Applied Mechanics* (21), S. 241–249.

- Hill, R. (1948): A theory of the yielding and plastic flow of anisotropic metals. In: *Proceedings of the Royal Society of London* (193:281–297).
- Hill, R. (1952): On discontinuous plastic states, with special reference to localized necking in thin sheets. In: *Journal of the Mechanics and Physics of Solids* 1 (1), S. 19–30. DOI: 10.1016/0022-5096(52)90003-3.
- Hosford, W. F. (1972): A generalized isotropic yield criterion. In: *Journal of Applied Mechanics* (39), S. 607–609.
- Hutchinson, J. W.; Tvergaard, V. (1981): Shear band formation in plane strain. In: *International Journal of Solids and Structures* 17 (5), S. 451–470. DOI: 10.1016/0020-7683(81)90053-6.
- Jang, I.; Bae, G.; Song, J.; Kim, H.; Park, N. (2020): Fracture envelopes on the 3D-DIC and hybrid inverse methods considering loading history. In: *Materials & Design* 194, S. 108934. DOI: 10.1016/j.matdes.2020.108934.
- Johnson, Gordon R.; Cook, William H. (1985): Fracture characteristics of three metals subjected to various strains, strain rates, temperatures and pressures. In: *Engineering Fracture Mechanics* 21 (1), S. 31–48. DOI: 10.1016/0013-7944(85)90052-9.
- Kajberg, J.; Lindkvist, G. (2004): Characterisation of materials subjected to large strains by inverse modelling based on in-plane displacement fields. In: *International Journal of Solids and Structures* 41 (13), S. 3439–3459. DOI: 10.1016/j.ijsolstr.2004.02.021.
- Khan, A. S.; Liu, H. (2012): A new approach for ductile fracture prediction on Al 2024-T351 alloy. In: *International Journal of Plasticity* 35, S. 1–12. DOI: 10.1016/j.ijplas.2012.01.003.
- Kim, J.; Gao, X.; Srivatsan, T. S. (2004): Modeling of void growth in ductile solids. Effects of stress triaxiality and initial porosity. In: *Engineering Fracture Mechanics* 71 (3), S. 379–400. DOI: 10.1016/S0013-7944(03)00114-0.
- Kim, J.-H.; Serpantié, A.; Barlat, Frederic; Pierron, Fabrice; Lee, Myoung-Gyu (2013): Characterization of the post-necking strain hardening behavior using the virtual fields method. In: *International Journal of Solids and Structures* 50, S. 3829–3842. DOI: 10.1016/j.ijsolstr.2013.07.018.
- Kingma, D.; Ba, J. (2014): Adam: A Method for Stochastic Optimization. In: *International Conference on Learning Representations*.
- Knysh, P.; Korkolis, Y. (2017): Identification of the post-necking hardening response of rate- and temperature-dependent metals. In: *International Journal of Solids and Structures* 115-116, S. 149–160. DOI: 10.1016/j.ijsolstr.2017.03.012.
- Korkolis, Y.; Kyriakides, S. (2008a): Inflation and burst of aluminum tubes. Part II: An advanced yield function including deformation-induced anisotropy. In: *International Journal of Plasticity - INT J PLASTICITY* 24, S. 1625–1637. DOI: 10.1016/j.ijplas.2008.02.011.

- Korkolis, Y.; Kyriakides, S. (2008b): Inflation and burst of anisotropic aluminum tubes for hydroforming applications. In: *International Journal of Plasticity - INT J PLASTICITY* 24, S. 509–543. DOI: 10.1016/j.ijplas.2007.07.010.
- Korkolis, Y.; Kyriakides, S. (2009): Path-dependent failure of inflated aluminum tubes. In: *International Journal of Plasticity - INT J PLASTICITY* 25, S. 2059–2080. DOI: 10.1016/j.ijplas.2008.12.016.
- Korkolis, Y.; Kyriakides, S. (2011a): Hydroforming of anisotropic aluminum tubes: Part I experiments. In: *International Journal of Mechanical Sciences - INT J MECH SCI* 53, S. 75–82. DOI: 10.1016/j.ijmecsci.2010.11.003.
- Korkolis, Y.; Kyriakides, S. (2011b): Hydroforming of anisotropic aluminum tubes: Part II analysis. In: *International Journal of Mechanical Sciences - INT J MECH SCI* 53, S. 83–90. DOI: 10.1016/j.ijmecsci.2010.11.004.
- Krajcinovic, D.; Lemaitre, J. (1987): *Continuum Damage Mechanics. Theory and applications*: Springer-Verlag Wien.
- Kramer, S. L. B.; Jones, A.; Mostafa, A.; Ravaji, Babak; Tancogne-Dejean, Thomas; Roth, Christian C. et al. (2019): The third Sandia fracture challenge: predictions of ductile fracture in additively manufactured metal. In: *Int J Fract* 218 (1), S. 5–61. DOI: 10.1007/s10704-019-00361-1.
- Kuo, C.-C. Jay (2016): Understanding convolutional neural networks with a mathematical model. In: *Journal of Visual Communication and Image Representation* 41, S. 406–413. DOI: 10.1016/j.jvcir.2016.11.003.
- Kuwabara, T.; Yoshida, K.; Narihara, K.; Takahashi, S. (2005): Anisotropic plastic deformation of extruded aluminum alloy tube under axial forces and internal pressure. In: *International Journal of Plasticity* 21 (1), S. 101–117. DOI: 10.1016/j.ijplas.2004.04.006.
- Lemaitre, J. (1985): A Continous Damage Mechanics Model for Ductile Fracture, zuletzt geprüft am 01.02.2019.
- Lemaitre, J. (1986): Local approach of fracture. In: *Engineering Fracture Mechanics* 25 (5), S. 523–537. DOI: 10.1016/0013-7944(86)90021-4.
- Lemaitre, J. (1996): *A Course on Damage Mechanics*: Springer-Verlag Berlin Heidelberg.
- Lemaitre, J.; Chaboche, J.-L. (1990): *Mechanics of Solid Materials*.
- Lemaitre, J.; Desmorat, R. (2005): *Engineering Damage Mechanics. Ductile, Creep, Fatigue and Brittle Failures*: Springer-Verlag Berlin Heidelberg.
- Li, F.; Du X. (2010): Mesh-dependence of Material with Softening Behavior. In: *Chinese Journal of Aeronautics* 23 (1), S. 46–53. DOI: 10.1016/S1000-9361(09)60186-2.

- Li, H.; Fu, M. W.; Lu, J.; Yang, H. (2011): Ductile fracture. Experiments and computations. In: *International Journal of Plasticity* 27 (2), S. 147–180. DOI: 10.1016/j.ijplas.2010.04.001.
- Li, Y.; Wierzbicki, T. (2010): Prediction of plane strain fracture of AHSS sheets with post-initiation softening. In: *International Journal of Solids and Structures* (47), S. 2316–2327.
- Ling, C.; Forest, S.; Besson, J.; Tanguy, B.; Latourte, F. (2018): A reduced micromorphic single crystal plasticity model at finite deformations. Application to strain localization and void growth in ductile metals. In: *International Journal of Solids and Structures* 134, S. 43–69. DOI: 10.1016/j.ijsolstr.2017.10.013.
- Lode, W. (1926): Versuche über den Einfluß der mittleren Hauptspannung auf das Fließen der Metalle Eisen, Kupfer und Nickel. In: *Zeitschrift für Physik* 36 (11), S. 913–939. DOI: 10.1007/BF01400222.
- Lou, Y.; Chen, L.; Clausmeyer, T.; Tekkaya, A. E.; Yoon, J. W. (2017): Modeling of ductile fracture from shear to balanced biaxial tension for sheet metals. In: *International Journal of Solids and Structures* 112, S. 169–184. DOI: 10.1016/j.ijsolstr.2016.11.034.
- Lou, Y.; Huh, H. (2013): Extension of a shear-controlled ductile fracture model considering the stress triaxiality and the Lode parameter. In: *International Journal of Solids and Structures* 50 (2), S. 447–455. DOI: 10.1016/j.ijsolstr.2012.10.007.
- Lou, Y.; Yoon, J. W.; Huh, H. (2014): Modeling of shear ductile fracture considering a changeable cut-off value for stress triaxiality. In: *International Journal of Plasticity* 54, S. 56–80. DOI: 10.1016/j.ijplas.2013.08.006.
- Lou, Yanshan; Huh, Hoon; Lim, Sungjun; Pack, Keunhwan (2012): New ductile fracture criterion for prediction of fracture forming limit diagrams of sheet metals. In: *International Journal of Solids and Structures* 49, S. 3605–3615. DOI: 10.1016/j.ijsolstr.2012.02.016.
- Malcher, L.; Andrade Pires, F. M.; César de Sá, J.M.A. (2012): An assessment of isotropic constitutive models for ductile fracture under high and low stress triaxiality. In: *International Journal of Plasticity* 30-31, S. 81–115. DOI: 10.1016/j.ijplas.2011.10.005.
- Malvern, L. E. (1969): *Introduction to the Mechanics of a Continuous Medium*: Prentice-Hall.
- Marouani, H.; Aguir, H. (2011): Identification of material parameters of the Gurson–Tvergaard–Needleman damage law by combined experimental, numerical sheet metal blanking techniques and artificial neural networks approach. In: *Int J Mater Form* 5. DOI: 10.1007/s12289-011-1035-x.
- Mase, G. T.; Smelser, R. E.; Mase, G. E. (2010): *Continuum mechanics for engineers*: CRC Press Taylor & Francis Group.

- Mazars, J.; Pijaudier-Cabot, G. (1996): From damage to fracture mechanics and conversely: A combined approach. In: *International Journal of Solids and Structures* 33 (20), S. 3327–3342. DOI: 10.1016/0020-7683(96)00015-7.
- McClintock, F. A. (1968a): A Criterion for Ductile Fracture by the Growth of Holes. In: *Journal of Applied Mechanics*.
- McClintock, F. A. (1968b): A Criterion for Ductile Fracture by the Growth of Holes. In: *appliedmechanics* 35 (2), S. 363–371. DOI: 10.1115/1.3601204.
- McDonald, B.; Bornstein, H.; Ameri, A.; Daliri, A.; Orifici, A. C. (2019): Plasticity and ductile fracture behaviour of four armour steels. In: *International Journal of Solids and Structures* 176-177, S. 135–149. DOI: 10.1016/j.ijsolstr.2019.05.013.
- Mirone, G.; Corallo, D. (2010): A local viewpoint for evaluating the influence of stress triaxiality and Lode angle on ductile failure and hardening. In: *International Journal of Plasticity* 26 (3), S. 348–371. DOI: 10.1016/j.ijplas.2009.07.006.
- Mohr, D.; Treitler, R. (2008): Onset of fracture in high pressure die casting aluminum alloys. In: *Engineering Fracture Mechanics* 75 (1), S. 97–116. DOI: 10.1016/j.engfracmech.2007.01.029.
- Nahshon, K.; Hutchinson, J. W. (2008): Modification of the Gurson Model for shear failure. In: *European Journal of Mechanics - A/Solids* 27 (1), S. 1–17. DOI: 10.1016/j.euromechsol.2007.08.002.
- Needleman, A. (1988): Material rate dependence and mesh sensitivity in localization problems. In: *Computer Methods in Applied Mechanics and Engineering* 67 (1), S. 69–85. DOI: 10.1016/0045-7825(88)90069-2.
- Neukamm, Frieder; Feucht, Markus; Haufe, André (Hg.) (2009): Considering damage history in crashworthiness simulations. 7th European LS-DYNA Conference. Salzburg, Austria, May 14-15.
- Öchsner, A. (2016): *Continuum Damage and Fracture Mechanics*: Springer Science+Business Media Singapore.
- Pack, K.; Mohr, D. (2017): Combined necking & fracture model to predict ductile failure with shell finite elements. In: *Engineering Fracture Mechanics* 182, S. 32–51. DOI: 10.1016/j.engfracmech.2017.06.025.
- Pack, K.; Tancogne-Dejean, T.; Gorji, Maysam B.; Mohr, D. (2018): Hosford-Coulomb ductile failure model for shell elements: Experimental identification and validation for DP980 steel and aluminum 6016-T4. In: *International Journal of Solids and Structures* 151, S. 214–232. DOI: 10.1016/j.ijsolstr.2018.08.006.
- Paredes, M.; Wierzbicki, T.; Zelenak, P. (2016): Prediction of crack initiation and propagation in X70 pipeline steels. In: *Engineering Fracture Mechanics* 168, S. 92–111. DOI: 10.1016/j.engfracmech.2016.10.006.
- Pineau, A.; Benzerga, A.; Pardoën, T. (2016): Failure of Metals I – Brittle and Ductile Fracture. In: *Acta Materialia* 107, S. 424–483. DOI: 10.1016/j.actamat.2015.12.034.

- Qian, L.-Y.; Fang, G.; Zeng, P.; Wang, Q. (2015): Experimental and numerical investigations into the ductile fracture during the forming of flat-rolled 5083-O aluminum alloy sheet. In: *Journal of Materials Processing Technology* 220, S. 264–275. DOI: 10.1016/j.jmatprotec.2015.01.031.
- Reddi, D.; Areej, V. K.; Keralavarma, S. M. (2019): Ductile failure simulations using a multi-surface coupled damage-plasticity model. In: *International Journal of Plasticity*. DOI: 10.1016/j.ijplas.2019.02.007.
- Rice, J. R.; Tracey, D. M. (1969): On the ductile enlargement of voids in triaxial stress fields*. In: *Journal of the Mechanics and Physics of Solids* 17 (3), S. 201–217. DOI: 10.1016/0022-5096(69)90033-7.
- Rice, James R. (1976): The localisation of plastic deformation. In: *Theoretical and Applied Mechanics* 1, zuletzt geprüft am 13.05.2018.
- Riks, E. (1979): An incremental approach to the solution of snapping and buckling problems. In: *International Journal of Solids and Structures* 15 (7), S. 529–551. DOI: 10.1016/0020-7683(79)90081-7.
- Roth, C. C.; Mohr, D. (2016): Ductile fracture experiments with locally proportional loading histories. In: *International Journal of Plasticity* 79, S. 328–354. DOI: 10.1016/j.ijplas.2015.08.004.
- Roth, C. C.; Mohr, D. (2018): Determining the strain to fracture for simple shear for a wide range of sheet metals. In: *International Journal of Mechanical Sciences* 149, S. 224–240. DOI: 10.1016/j.ijmecsci.2018.10.007.
- Roth, C. C.; Morgeneyer, T. F.; Cheng, Y.; Helfen, L.; Mohr, D. (2018): Ductile damage mechanism under shear-dominated loading: In-situ tomography experiments on dual phase steel and localization analysis. In: *International Journal of Plasticity*, S. 162–192.
- Roux, Emile; Bouchard, Pierre-Olivier (2010): Ductile Damage Material Parameter Identification. Numerical Investigation. In: Paper 135–ISBN 978.
- Rudnicki, J. W.; Rice, J. R. (1975): Conditions for the localization of deformation in pressure-sensitive dilatant materials. In: *Journal of the Mechanics and Physics of Solids* 23 (6), S. 371–394. DOI: 10.1016/0022-5096(75)90001-0.
- Scales, M.; Chen, K.; Kyriakides, S. (2019): Material Response, Localization, and Failure of an Aluminum Alloy Under Combined Shear and Tension. Part I Experiments. In: *International Journal of Plasticity*. DOI: 10.1016/j.ijplas.2019.04.004.
- Scales, M.; Tardif, N.; Kyriakides, S. (2016): Ductile failure of aluminum alloy tubes under combined torsion and tension. In: *International Journal of Solids and Structures* 97-98, S. 116–128. DOI: 10.1016/j.ijsolstr.2016.07.038.
- Soare, Stefan C. (2016): On the overall yielding of an isotropic porous material with a matrix obeying a non-quadratic criterion. In: *International Journal of Engineering Science* 104, S. 5–19. DOI: 10.1016/j.ijengsci.2016.04.005.

- Springmann, M.; Kuna, M. (2005): Identification of material parameters of the Gurson–Tvergaard–Needleman model by combined experimental and numerical techniques. In: *Computational Materials Science* 32 (3), S. 544–552. DOI: 10.1016/j.commatsci.2004.09.010.
- St. Pietruszczak; Mróz, Z. (1981): Finite element analysis of deformation of strain-softening materials. In: *International Journal for Numerical Methods in Engineering* 17 (3), S. 327–334. DOI: 10.1002/nme.1620170303.
- Stewart, M. (2018): Simple Introduction to Convolutional Neural Networks. In: *Towards Data Science*. Online article. <https://towardsdatascience.com/simple-introduction-to-convolutional-neural-networks-cdf8d3077bac>, 01.02.2021.
- Sun, Q.; Lu, Y.; Chen, J. (2020): Identification of material parameters of a shear modified GTN damage model by small punch test. In: *Int J Fract* 222 (1), S. 25–35. DOI: 10.1007/s10704-020-00428-4.
- Tardif, N.; Kyriakides, S. (2012): Determination of anisotropy and material hardening for aluminum sheet metal. In: *International Journal of Solids and Structures* 49 (25), S. 3496–3506. DOI: 10.1016/j.ijsolstr.2012.01.011.
- Teng, X.; Mae, H.; Bai, Y.; Wierzbicki, T. (2008): Statistical analysis of ductile fracture properties of an aluminum casting. In: *Engineering Fracture Mechanics* 75 (15), S. 4610–4625. DOI: 10.1016/j.engfracmech.2008.04.016.
- Teng, X.; Wierzbicki, T. (2006): Evaluation of six fracture models in high velocity perforation. In: *Engineering Fracture Mechanics* 73 (12), S. 1653–1678. DOI: 10.1016/j.engfracmech.2006.01.009.
- Thomas, N.; Basu, S.; Benzerga, A. A. (2016): On fracture loci of ductile materials under non-proportional loading. In: *International Journal of Mechanical Sciences* 117, S. 135–151. DOI: 10.1016/j.ijmecsci.2016.08.007.
- Torki, M. E. (2019): A unified criterion for void growth and coalescence under combined tension and shear. In: *International Journal of Plasticity*. DOI: 10.1016/j.ijplas.2019.02.002.
- Tutyshkin, N.; Müller, W. H.; Wille, R.; Zapara, M. (2014): Strain-induced damage of metals under large plastic deformation. Theoretical framework and experiments. In: *International Journal of Plasticity* 59, S. 133–151. DOI: 10.1016/j.ijplas.2014.03.011.
- Tvergaard, V. (2009): Behaviour of voids in a shear field. In: *Int J Fract* 158, S. 41–49. DOI: 10.1007/s10704-009-9364-1.
- Tvergaard, V. (2012): Effect of stress-state and spacing on voids in a shear-field. In: *International Journal of Solids and Structures* 49 (22), S. 3047–3054. DOI: 10.1016/j.ijsolstr.2012.06.008.
- Tvergaard, V.; Needleman, A. (1984): Analysis of the cup-cone fracture in a round tensile bar. In: *Acta Metallurgica* 32 (1), S. 157–169. DOI: 10.1016/0001-6160(84)90213-X.

Tvergaard, V.; Needleman, A.; Lo K, K. (1981): Flow localization in the plane strain tensile test. In: *Journal of the Mechanics and Physics of Solids* 29 (2), S. 115–142. DOI: 10.1016/0022-5096(81)90019-3.

Wang, P.; Qu, S. (2018): Analysis of ductile fracture by extended unified strength theory. In: *International Journal of Plasticity* 104, S. 196–213. DOI: 10.1016/j.ijplas.2018.02.011.

Wriggers, P. (2008): *Nonlinear Finite Element Methods*: Springer-Verlag Berlin Heidelberg.

Xue, L. (2006): Damage accumulation and fracture initiation in uncracked ductile solids subject to triaxial loading. In: *International Journal of Solids and Structures* 44 (16), S. 5163–5181. DOI: 10.1016/j.ijsolstr.2006.12.026.

Xue, L. (2008): Constitutive modeling of void shearing effect in ductile fracture of porous materials. In: *Engineering Fracture Mechanics* 75 (11), S. 3343–3366. DOI: 10.1016/j.engfracmech.2007.07.022.

Xue, L.; Wierzbicki, T. (2007): Ductile fracture initiation and propagation modeling using damage plasticity theory. In: *Engineering Fracture Mechanics* 75 (11), S. 3276–3293. DOI: 10.1016/j.engfracmech.2007.08.012.

Zhang, K. S.; Bai, J. B.; Francois, D. (2000): Numerical analysis of the influence of the Lode parameter on void growth. In: *International Journal of Solids and Structures*.

Zribi, T.; Khalfallah, A.; Belhadjsalah, H. (2013): Experimental characterization and inverse constitutive parameters identification of tubular materials for tube hydroforming process. In: *Materials and Design* 49. DOI: 10.1016/j.matdes.2013.02.077.

Appendices

APPENDIX A

Implementation of nonlocal regularization according to (Anand et al. 2012) in ANSYS Mechanical APDL

```
/com, define first the length scale leng in (mm)
leng=0.195      !mm
PI=3.141592654
esel,all
*get,nelems,elem,,count

!loop elems
*del,loop_elems
*dim,loop_elems,array,nelems

csys,0
wpcsys,,0
cmsel,s,middle_elems
*vget,loop_elems(1),elem,1,esel,1

csys,0
esel,all
*del,x_list
*del,y_list
*del,z_list
*dim,x_list,array,nelems
*dim,y_list,array,nelems
*dim,z_list,array,nelems

*vget,x_list(1),elem,1,cent,x
*vget,y_list(1),elem,1,cent,y
*vget,z_list(1),elem,1,cent,z
```

```

*del,el_volumes
*dim,el_volumes,array,nelems
esel,all
*do,nelem,1,nelems
    *get,elem_volu,elem,nelem,volu
    el_volumes(nelem)=elem_volu
*enddo

esel,all
etable,plstrain,eppl,eqv
*del,pl_strains
*dim,pl_strains,array,nelems
*vget,pl_strains,elem,1,etab,plstrain

con1=-1/(2*leng**2)
con2=1/((2*PI)**(3/2)*leng**3)
*del,cons1
*del,cons2
*dim,cons1,array,nelems
*dim,cons2,array,nelems
*do,i,1,nelems
    cons1(i)=con1
    cons2(i)=con2
*enddo

*del,ep_elem
*dim,ep_elem,array,nelems

*do,nelem,1,nelems

check_elem=loop_elems(nelem)

*if,check_elem,eq,1,then

*del,vecX0
*dim,vecX0,array,nelems
*del,vecY0
*dim,vecY0,array,nelems
*del,vecZ0
*dim,vecZ0,array,nelems

*vfill,vecX0(1),ramp,x_list(nelem,1),0
*vfill,vecY0(1),ramp,y_list(nelem,1),0
*vfill,vecZ0(1),ramp,z_list(nelem,1),0

!loop over locations in array parameter

```

```

*voper,diffX,vecX0(1),sub,x_list(1)
*voper,diffY,vecY0(1),sub,y_list(1)
*voper,diffZ,vecZ0(1),sub,z_list(1)
*voper,vec_sqX,diffX,mult,diffX
*voper,vec_sqY,diffY,mult,diffY
*voper,vec_sqZ,diffZ,mult,diffZ

*voper,lab1,vec_sqX,add,vec_sqY
*voper,lab2,lab1,add,vec_sqZ
*voper,lab3,lab2,mult,cons1
*vfun,lab4,exp,lab3
*voper,npsi,cons2,mult,lab4

*voper,npsi_epsPL,npsi,mult,pl_strains
*voper,psi,npsi,mult,el_volumes

*voper,psi_epsPL,npsi_epsPL,mult,el_volumes
*vscfun,sum1,sum,psi_epsPL
*vscfun,sum2,sum,psi

ep_el=sum1/sum2
ep_elem(nelem)=ep_el

*endif

*enddo

ep_scale=1
esel,all
etable,ep,eppl,eqv
*vput,ep_elem(1),elem,1,etab,ep
*if,ep_scale,ne,1,then
    sadd,dep,plstrain,ep,,-1*ep_scale
*endif

```

APPENDIX B

Implementation of stress triaxiality, Lode angle parameter and ductile fracture locus model according to (Lou and Huh 2013) in ANSYS Mechanical APDL

```

/com, define model constants c1, c2, c3
c1=2.081504124
c2=0.55650812
c3=2.423085375

esel,all
*get,num_e,elem,0,count

PI=3.141592654
etable,sigma1,s,1
etable,sigma2,s,2
etable,sigma3,s,3

sadd,lab1,sigma1,sigma2
sadd,lab2,lab1,sigma3
smult,meanstress,lab2,,1/3

etable,hydro,nl,hpres           !store hydrostatic stress
etable,seqv,s,eqv              !store equivalent stress
sexp,inv_seqv,seqv,, -1
smult,TRIAX1,hydro,inv_seqv

sadd,dev1,sigma1,hydro,1,-1     !principal deviatoric stress
sadd,dev2,sigma2,hydro,1,-1
sadd,dev3,sigma3,hydro,1,-1
sexp,d_dev1,dev1,,2
sexp,d_dev2,dev2,,2
sexp,d_dev3,dev3,,2
sadd,sum1,d_dev1,d_dev2
sadd,sum2,sum1,d_dev3
sadd,J2,sum2,,1/2              !second deviatoric invariant

smult,lab1,J2,,3
*del,fun_1
*dim,fun_1,array,num_e
*vget,fun_1(1),elem,1,etab,lab1 !store data to array
*del,fun_2
*dim,fun_2,array,num_e
*vfun,fun_2(1),sqrt,fun_1(1)   !perform a function on a single
array parameter

```

```

etable,vonmises,s,1
*vput,fun_2(1),elem,1,etab,vonmises

sexp,inv_mises,vonmises,, -1           !store the inverse of SEQV
smult,TRIAX,meanstress,inv_mises      !multiply the hydrostatic
stress by the inverse of SEQV

smult,J3_step1,dev1,dev2
smult,J3,J3_step1,dev3                 !third deviatoric invariant

!formula with von mises
sexp,inv_seqv_3,seqv,, -3
smult,final,J3,inv_seqv_3,27/2,1
!formula with J2 for checking
!sexp,invJ2_3/2,J2,, -3/2
!smult,final,J3,invJ2_3/2,3*(SQRT(3))/2,1

*del,fun_1
*dim,fun_1,array,num_e
*vget,fun_1(1),elem,1,etab,final      !store data to array
*del,fun_2
*dim,fun_2,array,num_e
*vfun,fun_2(1),asin,fun_1(1)          !perform a function on a
single array parameter
etable,fun_asin,s,1
*vput,fun_2(1),elem,1,etab,fun_asin   !save back to etable
sadd,lode_rad,fun_asin,, -1/3
sadd,lode_deg,lode_rad,, 180/PI
sadd,reference,lode_rad,,,,PI/6       !shifting the reference for
normalized Lode angle in shear=0
sadd,NORMLODE,reference,, -6/PI,, 1

sexp,lab1,NORMLODE,, 2
sadd,lab2,lab1,,,, 3
*del,fun_3
*dim,fun_3,array,num_e
*vget,fun_3(1),elem,1,etab,lab2
*del,fun_4
*dim,fun_4,array,num_e
*vfun,fun_4(1),sqrt,fun_3(1)
etable,lab3,s,1
*vput,fun_4(1),elem,1,etab,lab3
sexp,lab4,lab3,, -1
smult,lab5,lab4,, 2
sexp,lab6,lab5,, c1

```

```
sadd,lab7,TRIAx,,3,,1
!cut of x value
*del,etriax1
*dim,etriax1,array,num_e
*vget,etriax1(1),elem,1,etab,lab7
*del,etriax
*dim,etriax,array,num_e
*do,numele,1,num_e
    current_triax=etriax1(numele)
    *if,current_triax,ge,0,then
        new_triax=current_triax
    *else
        new_triax=0
    *endif
    etriax(numele)=new_triax
*enddo

etable,lab77,s,1
*vput,etriax(1),elem,1,etab,lab77

smult,lab8,lab77,,1/2
sexp,lab9,lab8,,c2

smult,lab10,lab6,lab9
sexp,lab11,lab10,, -1
smult,fracture_strain,lab11,,c3
```

APPENDIX C

Solution algorithm in ANSYS Mechanical APDL for coupled elasto-plastic analysis with calculation of strain-based damage variable

```

/solu
antype,static
nlgeom,on                               !include large-deflection effects
outres,all,all
nsubst,1,1000,1
neqit,1000
lnsrch,on
ncnv,2
!terminate the analysis, but not the program execution, if the
solution fails to converge

total_time=1
time_inc=total_time/num_steps

flagstrain=0
flagkill=0
flagendstep=0

esel,all
*get,nelems,elem,,count
*del,tot_D
*dim,tot_D,array,nelems
*del,tot_eps
*dim,tot_eps,array,nelems

*get,twall_before_solve,active,0,time,wall

*do,step_no,1,num_steps
    csys,15      !local CS system fits to the CS of DIC

    time,step_no*time_inc
    current_time=step_no/num_steps

    !apply real DIC displacement to top nodes
    cmsel,s,top_nodes
    current_node=0
    *do,i,1,n_top_nodes
        current_node=ndnext(current_node)
        current_locX=nx(current_node)
        Xdispl_DIC%i%=(top_nodes_X(current_locX,current_time))
    
```



```

Ydispl_DIC%i%=- (top_nodes_Y(current_locX,current_time))
d,current_node,ux,Xdispl_DIC%i%
d,current_node,uy,Ydispl_DIC%i%
*enddo
!apply real DIC displacement to down nodes
cmsel,s,down_nodes
current_node=0
*do,i,1,n_down_nodes
current_node=ndnext(current_node)
current_locX=nx(current_node)
Xdispl_DIC%i%=(bottom_nodes_X(current_locX,current_time))
Ydispl_DIC%i%=- (bottom_nodes_Y(current_locX,current_time))
d,current_node,ux,Xdispl_DIC%i%
d,current_node,uy,Ydispl_DIC%i%
*enddo

allsel
solve
finish

*get,convergence_ind,active,0,solu,cnvg
*if,convergence_ind,eq,0,then
    *get,n_lstep,active,0,solu,ncmls
    end_step=n_lstep
*endif
*if,convergence_ind,eq,0,exit

/post1
set,step_no
esel,all
etable,plstrain,nl,epeq          !eqv.pl strain

esel,s,etab,plstrain,,0
esel,inve
cm,selems,elem
*get,num_selems,elem,0,count

*del,selems
*dim,selems,array,nelems

cmsel,s,selems
*vget,selems(1),elem,1,esel,1

*del,epeq_strain
*dim,epeq_strain,array,nelems

```

```

*vmask,selems(1)
*vget,epeq_strain(1),elem,1,etab,plstrain
*vscfun,maxstrain,max,epeq_strain(1)

!store the load step when yield condition is fullfilled
*if,maxstrain,gt,0,and,flagstrain,eq,0,then
    *get,pl_step,active,0,set,lstp
    flagstrain=1
*endif

*if,flagstrain,eq,1,then
esel,all

!increment of the equivalent strain
*if,step_no,eq,pl_step,then
etable,dE,nl,epeq
*else      !step_no > pl_step
set,step_no-1
etable,pl_prev,nl,epeq
sadd,dE,plstrain,pl_prev,1,-1
*endif

set,step_no
*del,dE
*dim,dE,array,nelems
*vget,dE(1),elem,1,etab,dE

!compute the fracture_strain for current stress state
/input,LOUmodel,inp
sexp,inv_fstrain,fracture_strain,, -1
*del,fracture_strain
*dim,fracture_strain,array,nelems
*vget,fracture_strain(1),elem,1,etab,fracture_strain

smult,dD,dE,inv_fstrain
*del,dD
*dim,dD,array,nelems
*vget,dD(1),elem,1,etab,dD
!damage for current step, always overwritten

*voper,tot_D(1),tot_D(1),add,dD(1)
etable,tot_D,s,1
*vput,tot_D(1),elem,1,etab,tot_D
*vscfun,maxD,max,tot_D(1)

!save the number of final step when D=1 is reached

```

```

*if,maxD,ge,1,and,flagendstep,eq,0,then
    *get,end_step,active,0,set,lstp
    flagendstep=1
*endif

*if,maxD,ge,1,exit
!exits the current do loop if condition is fullfilled

esel,all
!checking the strains
*voper,tot_eps(1),tot_eps(1),add,dE(1)
etable,tot_eps,s,1
*vput,tot_eps(1),elem,1,etab,tot_eps

*del,current_EPS
*dim,current_EPS,array,nelems

*vget,current_EPS(1),elem,1,etab,tot_eps
*vscfun,maxEPS,max,current_EPS(1)
*vscfun,maxEPSelem,lmax,current_EPS(1)

!select the elemens with damage increment > 0
esel,s,etab,dD,,0
esel,inve
cm,delems,elem
*get,num_delems,elem,0,count

*del,delems
*dim,delems,array,nelems
cmsel,s,delems
*vget,delems(1),elem,1,esel,1

*del,current_D
*dim,current_D,array,nelems

*vmask,delems(1)
*vget,current_D(1),elem,1,etab,tot_D
*vscfun,maxD,max,current_D(1)
*vscfun,maxDelem,lmax,current_D(1)

esel,s,etab,tot_D,1
*get,num_kill_elems,elem,0,count
*if,num_kill_elems,gt,0,then
cm,elems-to-kill,elem
*endif

```

```

!load step when first elems are killed
*if,num_kill_elems,gt,0,and,flagkill,eq,0,then
    *get,kill_step,active,0,set,lstp
    flagkill=1
*endif

allsel
cmwrite,elemcomps,txt

esel,all

!undamaged material response according to Voce hardening
esel,all
etable,plstrain,nl,epeq
smult,lab1,plstrain,,-b0
*del,fun1
*dim,fun1,array,nelems
*vget,fun1(1),elem,1,etab,lab1
*del,fun2
*dim,fun2,array,nelems
*vfun,fun2(1),exp,fun1(1)
etable,lab2,s,1
*vput,fun2(1),elem,1,etab,lab2
sadd,lab3,lab2,,-1,,1
*if,R0,eq,0,then
sadd,voce,lab3,,Rinf,,sig0
*else
sadd,voce,plstrain,lab3,R0,Rinf,sig0
*endif

/input,anand_regularization,inp

*del,current_voce
*dim,current_voce,array,nelems
*vmask,delems(1)
*vget,current_voce(1),elem,1,etab,voce

*del,current_dep
*dim,current_dep,array,nelems
*vmask,delems(1)
*vget,current_dep(1),elem,1,etab,dep

parsav,all
finish

/solu

```

```

antype,,rest
parres,new
/input,elemcomps,txt

*if,num_delems,gt,0,then

cmsel,s,delems
current_elem=0
*do,ii,1,num_delems

    current_elem=elnext(current_elem)

    Dfun=1-current_D(current_elem)
    sigma_voce=current_voce(current_elem)
    eps_ep=current_dep(current_elem)

    newyield=max(Dfun*(sigma_voce+L_parm*eps_ep),0.1*sig0)
    newmodulus=max(Dfun*young_modulus,0.1*young_modulus)

    mp,ex,%ii%+10,newmodulus
    mp,nuxy,%ii%+10,nu
    tb,biso,%ii%+10
    tbdata,1,newyield,0
    mpchg,%ii%+10,current_elem

*enddo
*endif

*if,num_kill_elems,gt,0,then
    cmsel,s,elems-to-kill,elem
    cm,killed_elems%step_no%,elem
    cmwrite,killed_elems%step_no%,txt
    ekill,all
*endif

*else
/solu
antype,,rest
*endif
*enddo

*get,twall_after_solve,active,0,time,wall

solution_time=twall_after_solve-twall_before_solve

```